

EUV-induced Plasma, Electrostatics and Particle Contamination Control

Citation for published version (APA):

van de Kerkhof, M. A. (2021). *EUV-induced Plasma, Electrostatics and Particle Contamination Control*. [Phd Thesis 1 (Research TU/e / Graduation TU/e), Applied Physics and Science Education]. Technische Universiteit Eindhoven.

Document status and date:

Published: 31/08/2021

Document Version:

Publisher's PDF, also known as Version of Record (includes final page, issue and volume numbers)

Please check the document version of this publication:

- A submitted manuscript is the version of the article upon submission and before peer-review. There can be important differences between the submitted version and the official published version of record. People interested in the research are advised to contact the author for the final version of the publication, or visit the DOI to the publisher's website.
- The final author version and the galley proof are versions of the publication after peer review.
- The final published version features the final layout of the paper including the volume, issue and page numbers.

[Link to publication](#)

General rights

Copyright and moral rights for the publications made accessible in the public portal are retained by the authors and/or other copyright owners and it is a condition of accessing publications that users recognise and abide by the legal requirements associated with these rights.

- Users may download and print one copy of any publication from the public portal for the purpose of private study or research.
- You may not further distribute the material or use it for any profit-making activity or commercial gain
- You may freely distribute the URL identifying the publication in the public portal.

If the publication is distributed under the terms of Article 25fa of the Dutch Copyright Act, indicated by the "Taverne" license above, please follow below link for the End User Agreement:

www.tue.nl/taverne

Take down policy

If you believe that this document breaches copyright please contact us at:

openaccess@tue.nl

providing details and we will investigate your claim.

EUV-induced Plasma, Electrostatics and Particle Contamination Control

PROEFSCHRIFT

ter verkrijging van de graad van doctor aan de Technische Universiteit
Eindhoven, op gezag van de rector magnificus, prof.dr.ir. F.P.T. Baaijens,
voor een commissie aangewezen door het College voor Promoties in het
openbaar te verdedigen op dinsdag 31 augustus 2021 om 16.00 uur

door

Marcus Adrianus van de Kerkhof

geboren te Helmond

Dit proefschrift is goedgekeurd door de promotoren en de samenstelling van de promotiecommissie is als volgt:

Voorzitter: prof.dr.ir. H.J.M. Swagten

Eerste promotor: prof.dr. V.Y. Banine

Tweede promotor: prof.dr.ir. G.M.W. Kroesen

Leden: Prof.dr.ir. J.P.H. Benschop (Universiteit Twente)

Prof.dr. F. Bijkerk (Universiteit Twente)

Prof.dr.ir. O.J. Luiten

Abel Bliss Professor of Engineering David N. Ruzic
(University of Illinois)

Dr.ir. J. Beckers

植樹的最佳時間是二十年前。第二個最好的時間是現在

(The best time to plant a tree was twenty years ago; the second best time is now)

Summary

Extreme UV (EUV) lithography has recently been introduced for high-volume manufacturing of semiconductor devices. Inside the EUV scanner, an EUV-induced plasma is formed in the hydrogen background gas. This weakly ionized plasma is instrumental in maintaining high system transmission by preventing carbon contamination and oxidation of the EUV mirrors. Potential side effects however are etching of the surrounding construction materials, particle release, and risk of charging of floating surfaces and discharges. This thesis will describe relevant aspects of the EUV generation and spectral composition, and the resulting impact on wafer imaging and on the EUV-induced plasma.

The EUV scanner is sensitive to two types of contamination: chemical contamination and particle contamination. Both contamination types will influence the imaging quality of the scanner, and both will be significantly influenced by the EUV-induced plasma. This thesis will focus primarily on the particle contamination aspect, while also some molecular aspects will be briefly discussed.

In terms of particle contamination control, the effect of plasma on release and transport of particles is known from observations from astrophysics and space missions, linking phenomena such as lunar glow and dust accumulation on spacecraft to charging effects on particles by electrons, ions and/or energetic photons in space. We have translated these studies to the EUV-induced scanner plasma, and found that the critical factor determining release is the presence of fast (photo)electrons. Also, the adhesion force between particle and surface may be reduced by plasma etching of surface or particle, or by removal of bonding adsorbates or water. We will describe how the understanding of these two mechanisms can be translated in rules-of-thumb for selecting materials and surface finishing.

Once released from the surface, the force balance will be dominated by neutral drag from crossflow and the Coulomb force from plasma. We will describe how the Coulomb

force develops and how the combination of these forces can be tailored to keep particles away from critical surfaces.

Besides release and transport, the EUV-induced plasma can also result in significant charging of floating surfaces, most notably the reticle. This will lead to electrostatic attraction of particles, and potentially even lead to discharges as the reticle is unloaded. We will describe charging and discharging in more detail, using 3D-PIC model and measurements. We will also present a solution, including scanner validation.

In terms of plasma-materials interaction, the ion energies are crucial. The existing descriptions of single-pulse and more or less open EUV-induced plasma's were extended with a treatment of confinement and multiple pulses. It was found that confinement, with plasma-facing walls at a distance of order of the mean free path length of the energetic photoelectrons, requires explicit inclusion of secondary electron emission from the walls, which may be induced by photoelectric effect or by secondary electron emission by the energetic photoelectrons. For a pulsed plasma with a period shorter than the decay time of the plasma, the plasma will consist of a quasi-steady-state cold background plasma, and periodic transient peaks in ion energy and ion flux. A bi-Maxwellian treatment was introduced to describe this analytically. In terms of modeling, this means no assumptions can be made on the electron distribution functions, and a (Monte-Carlo) Particle-in-Cell (PIC) model is needed. We have presented an extension of the PIC model approach to complex 3D geometries and to multiple pulses, by using a Hybrid PIC-diffusion approach.

The resulting ion energies were found to be 2 eV, with a energy distribution tail of up to roughly 10 eV. This is significantly lower than found in single-pulse EUV-induced plasmas. These energies are well below the sputtering threshold for mirrors and construction materials. This holds both for close confinement around the beam as well as for close proximity to EUV-mirrors or the reticle. Materials with a high secondary electron emission may be beneficiary in this respect, but care should be taken that all materials must be robust against hydrogen radicals and ion-enhanced chemical reactions with hydrogen. The UV afterglow of EUV generation might last longer than

the EUV pulse itself, and might thereby frustrate sheath formation for some tenths of a microsecond; this also will result in reduced peak ion energies as the energetic electrons will cool down fast in the meantime.

Still, even for low ion energies, the hydrogen ions and radicals may affect many common construction materials and coatings in several ways, such as roughening, blistering and chemical reactions. This may have consequences for both particle contamination control as well as for molecular contamination control. The thermodynamics of hydrogen radicals and ions is unfavorable for almost all materials, so whether an interaction becomes problematic relies on the details of the reaction kinetics.

The plasma may affect particle adhesion by etching and roughening either the particle or the substrate, by chemical reaction, or by removing possible covalent bonds between particle and surface. Carbon and carbonaceous layers, such as e.g. greasy or oily residues, were found to be etched away by the hydrogen plasma, which will lead to release over time of hydrocarbons and of particles from poorly cleaned materials. Also, other materials that tend to react with hydrogen or form volatile hydrides were found to be liable to generate particles.

Looking towards the future, the EUV power will continue to rise to enable throughput improvements in the scanner. The ion flux will scale linearly with increasing EUV pulse energy, while the ion energy is independent of this, as all electron populations scale equally with power.

Samenvatting

Extreme UV (EUV) lithography is in de afgelopen jaren geïntroduceerd voor volume-fabricage van halfgeleider-chips. Binnenin de EUV-scanner wordt een plasma gevormd door de EUV-straling in het waterstof achtergrondgas. Dit plasma is van groot belang voor het behouden van een hoge transmissie door koolstofverontreiniging en oxidatie van de EUV-spiegels te voorkomen. Mogelijke bijwerkingen zijn echter etsen van de omringende bouwmaterialen, deeltjes, en risico op het opladen van elektrisch zwevende oppervlakken en ontladingen.

Dit proefschrift beschrijft relevante aspecten van de EUV-straling, en de daaruit voortvloeiende impact op de wafer en op het door EUV opgewekte plasma.

De EUV-scanner is gevoelig voor twee soorten verontreiniging: chemische verontreiniging en deeltjesverontreiniging. Beide soorten verontreiniging zullen de afbeeldingskwaliteit van de scanner beïnvloeden en beide zullen worden beïnvloed door het door EUV opgewekte plasma. Dit proefschrift zal zich voornamelijk richten op deeltjesverontreiniging, terwijl ook enkele aspecten van moleculaire verontreiniging kort zullen worden besproken.

Wat betreft deeltjesverontreiniging is het effect van plasma op het vrijkomen en transport van deeltjes bekend uit de astrofysica en ruimtemissies, waarbij verschijnselen zoals 'lunar glow' en stofaccumulatie op ruimtevaartuigen gekoppeld worden aan oplading van deeltjes door elektronen, ionen en/of energetische fotonen in de ruimte. We hebben deze studies vertaald naar het door EUV opgewekte scannerplasma en bevestigd dat de kritische factor die de afgifte bepaalt de aanwezigheid van energetische (foto)elektronen is.

Ook kan de hechtingskracht tussen het deeltje en het oppervlak worden verminderd door plasma-etsen van oppervlak of deeltje, of door het versneld verdampen van geadsorbeerd water. Het begrip van deze twee mechanismen kan worden vertaald in vuistregels voor het selecteren van materialen en oppervlakteaafwerkingen.

Enmaal los van het oppervlak, wordt de krachtenbalans op het deeltje gedomineerd door de gasstroming en de coulomb-kracht vanuit het plasma. Deze thesis beschrijft hoe de coulomb-kracht zich ontwikkelt en hoe de combinatie van krachten kan worden geoptimaliseerd om deeltjes weg te houden van kritische oppervlakken.

Naast afgifte en transport kan het EUV-plasma ook resulteren in oplading van elektrisch zwevende oppervlakken, met name het masker (of reticle). Dit zal leiden tot elektrostatische aantrekking van deeltjes, en mogelijk zelfs tot ontladingen. Het laden en ontladen zal in detail worden beschreven, aan de hand van een 3D-PIC-model en metingen. Er zullen ook oplossingen worden gepresenteerd, inclusief validatie in scanner.

Voor de interactie tussen plasma en materialen is de energie van de ionen cruciaal. In dit proefschrift worden de bestaande beschrijvingen van EUV-plasma's op basis van geïsoleerde pulsen en/of in min of meer open geometrieën uitgebreid met een behandeling van meerdere pulsen en van begrenzing van het plasma. Begrenzing van het plasma, met wanden op een afstand in de orde van grootte van de gemiddelde vrije weglengte van de energetische foto-elektronen, betekent dat secundaire elektronenemissie van de wanden expliciet moet worden meegenomen in het model. Voor een periodiek plasma met een periode tussen de pulsen die korter is dan de vervaltijd van het plasma, zal het plasma bestaan uit een quasi-stationair koud achtergrondplasma en periodieke pieken in ionenenergie en ionenflux. In dat geval moet een bi-Maxwelliaanse behandeling worden gebruikt voor een analytische beschrijving. Qua modellering betekent dit dat er geen aannames gedaan kunnen worden over de elektronenverdelingsfuncties en dat er een (Monte-Carlo) Particle-in-Cell (PIC) model nodig is. We presenteren hier een uitbreiding van het PIC-concept naar complexe 3D-geometrieën en naar meerdere pulsen. Dit wordt mogelijk gemaakt door gebruik te maken van een hybride PIC-diffusie-model.

De resulterende energie van de ionen is gemeten op 2 eV, met een staart in de energiedistributie tot ongeveer 10 eV. Dit is significant lager dan de energie die eerder gemeten is in EUV-plasma op basis van geïsoleerde pulsen. Deze energie ligt ruim onder de sputterdrempel voor spiegels en constructiematerialen. Dit geldt zowel voor plasma

met nauwe begrenzing rond de EUV-bundel als voor plasma nabij de EUV-spiegels of het masker. Constructiematerialen met een hoge secundaire elektronenemissie zouden bij voorkeur gebruikt moeten worden, maar te allen tijde moet geborgd worden dat alle materialen robuust zijn tegen waterstofradicalen en tegen waterstof-ionen. De UV-afterglow van het primaire EUV-plasma kan langer duren dan de EUV-puls zelf, en zou daardoor de vorming van de positieve plasma-potentiaal (die verantwoordelijk is voor de versnelling van de ionen naar de wand) kunnen vertragen met enkele tienden van een microseconde; deze vertraging kan resulteren in lagere piek-energie van de ionen aangezien het plasma in de tussentijd snel zal afkoelen.

Toch kunnen de waterstofionen en radicalen, zelfs bij lage energie, veel constructiematerialen en coatings op verschillende manieren aantasten, zoals opruwen, blaarvorming en chemische reacties. Dit kan gevolgen hebben voor zowel de beheersing van deeltjesverontreiniging als voor de beheersing van moleculaire verontreiniging. De thermodynamica van waterstofradicalen en ionen is ongunstig voor bijna alle materialen, dus of een interactie problematisch wordt, hangt vooral af van de details van de reactiekinetiek.

Het plasma kan de hechting van deeltjes aan oppervlakken verlagen door bijvoorbeeld het deeltje of het substraat te etsen en op te ruwen, door een chemische reactie of door mogelijke covalente bindingen tussen het deeltje en het oppervlak te verwijderen. Koolstof en koolstofhoudende lagen, zoals b.v. vette of olieachtige resten kunnen geëet worden door het waterstofplasma, wat na verloop van tijd zal leiden tot het vrijkomen van koolwaterstoffen en deeltjes vanaf slecht gereinigde materialen. Ook bleken materialen die de neiging hebben om met waterstof te reageren of vluchtige hydriden te vormen deeltjes te kunnen genereren.

Kijkend naar de toekomst, is de verwachting dat het EUV-vermogen zal blijven toenemen om de productiviteit van de scanner te blijven verbeteren. De ionenflux zal lineair schalen met het toenemende EUV-vermogen, terwijl de energie van de ionen gelijk zal blijven.

List of important symbols and abbreviations

EUV	Extreme ultraviolet (as used here: 13.5 nm)
VUV	Vacuum ultraviolet (10-120 nm wavelength)
UV	Ultraviolet (120-400 nm wavelengths)
e	Elementary charge ($1.60 \cdot 10^{-19}$ C)
eV	$1.60 \cdot 10^{-19}$ J
λ	Wavelength
P_{EUV}	EUV power
$h\nu$	Photon energy (EUV: 92 eV)
$\varphi_{h\nu}$	EUV photon flux
m	Mass (of particle)
g	Standard gravity
d_p (r_p)	Particle diameter (radius)
PRP	Parts per reticle pass (measure for particle contamination)
RME	Reticle Mini Environment
q (q_p)	Charge (of particle)
E	Electrical field
F_{el}	Coulomb force (electric force)
F_{vdw}	Van der Waals force
A_H	Hamaker constant
F_{rel}	Release force
m_e	Electron mass ($9.11 \cdot 10^{-31}$ kg)
m_i	Ion mass (for H_3^+ : $5.02 \cdot 10^{-27}$ kg)
T_e	Electron temperature
n_e	Electron density
T_i	Ion temperature
ϵ_0	Permittivity of free space ($8.85 \cdot 10^{-12}$ F/m)
n_i	Ion density
φ_i	Ion flux

λ_D	Debye length
ω_{pe}	Plasma electron frequency
L_s	Sheath width
v_B	Bohm velocity
ϕ_p	Plasma-wall potential difference
U_{ion}	Ion energy
RFEA	Retarding Field Energy Analyzer
EQP	Electrostatic Quadrupole Plasma analyzer
PIC	Particle in Cell
σ_{hv}	Cross section for photo-ionization
n_{H_2}	Hydrogen gas density
p	Pressure
λ_e	Mean free path of electron
v_e	Velocity of electron
σ_{en}	Electron-neutral (inelastic) collision cross section
f_{en}	Electron-neutral collision frequency
Λ_w	Typical length of the plasma confinement geometry
SEY	Secondary electron yield
D_a	Ambipolar diffusion constant
τ_a	Ambipolar diffusion time constant
ESVM	Electrostatic voltage measurements
γ_E	Energy transfer efficiency
U_b	Binding energy
U_{thr}	Sputtering threshold energy (Yamamura definition)
$Y(H)$	Hydrogen radical etch yield
$Y(H_n^+ H)$	Chemical sputtering yield (of ions)
φ_r	Hydrogen radical flux
ε	Ion energy

Contents

Summary	4
Samenvatting	7
List of symbols and abbreviations	10
1. Introduction: EUV lithography and particle contamination control	14
1.1 EUV lithography	15
1.2 EUV scanner outline	18
1.3 EUV scanner environment	20
1.4 Contamination and particles	21
1.5 Plasma aspect	23
1.6 Pellicle	25
1.7 Adhesion and release	26
1.8 Transport	29
1.9 Layout of this thesis	31
1.10 References	32
2. EUV generation and spectrum	34
2.1 Introduction	34
2.2 LPP EUV generation	36
2.3 LPP VUV and UV emission	38
2.4 VUV and UV spectrometry	39
2.5 UV at wafer level and imaging impact	42
2.6 UV afterglow and impact on plasma	45
2.7 Conclusion	46
2.8 References	46
3. EUV-induced plasma and scanner environment	48
3.1 Introduction	48
3.2 EUV beam	50
3.3 EUV-induced plasma	51
3.3.1 Plasma basics and equations	52
3.3.2 Plasma diagnostics	56
3.3.3 Plasma modeling: hybrid PIC	57
3.3.4 Plasma generation	61
3.3.5 Photoelectric effect	65
3.3.6 Wall losses, electron exchange and electron cooling	67
3.3.7 Diffusion, flux and energy	70
3.3.8 Volume recombination	74
3.3.9 Pulsed mode operation	76
3.3.10 Radicals	80
3.3.11 Gas flow	82
3.3.12 Gas purity	82
3.4 Reticle mini-environment	83

3.5	Off-line emulation of scanner plasma	86
3.6	Conclusion	88
3.7	References	90
4.	Plasma-assisted discharges and charging	95
4.1	Introduction	95
4.2	Plasma and electronics: plasma assisted discharges	97
4.3	Reticle charging and discharges	107
4.4	Particle transport and reticle protection	117
4.5	Conclusion	122
4.6	References	122
5.	Charging of particles on surfaces and particle release	125
5.1	Introduction	126
5.2	EUV generation and EUV-induced plasma	126
5.3	Particle charging and release by plasma	127
5.4	Conclusion	134
5.5	References	134
6.	Plasma-material interaction and particle release	136
6.1	Introduction	136
6.2	EUV generation and EUV-induced plasma	137
6.3	Plasma-material interaction and effect on particle adhesion	140
6.3.1	Surface erosion and sputtering	140
6.3.2	Chemical sputtering	142
6.3.3	Miscellaneous hydrogen-metal interactions	143
6.3.4	Hydrogen-carbon interactions	146
6.4	Conclusion	154
6.5	References	155
7.	Conclusions and outlook	160
7.1	Learnings and recommendations	161
7.2	Summary and outlook	167
	Acknowledgements	168
	Related publications	169
	Curriculum vitae	171

1

Introduction: EUV lithography and particle contamination control

This chapter is based on following publications:

- *M. van de Kerkhof, J. Benschop, V. Banine, "Lithography for now and the future", Solid-State Electronics, 155 (2019)*
- *M. van de Kerkhof, T. van Empel, M. Lercel, C. Smeets, F. van de Wetering, A. Nikipelov, A. Yakunin, V. Banine, "Advanced particle contamination control in EUV scanners", Proc. Of SPIE Vol. 10957 (2019)*

1.1. EUV lithography

We live in an era of information technology, which can be said to have truly started with the invention of the transistor by Bardeen, Brattain and Shockley in 1947, and the subsequent invention of the integrated circuit by Kilby in 1958. Information technology has been growing exponentially since. This growth has been fueled by exponential improvements in computation, storage and communication, which in turn are fueled by five innovation engines: 2D geometric scaling, device scaling, 3D layout scaling, circuit integration scaling, solution architecture scaling.

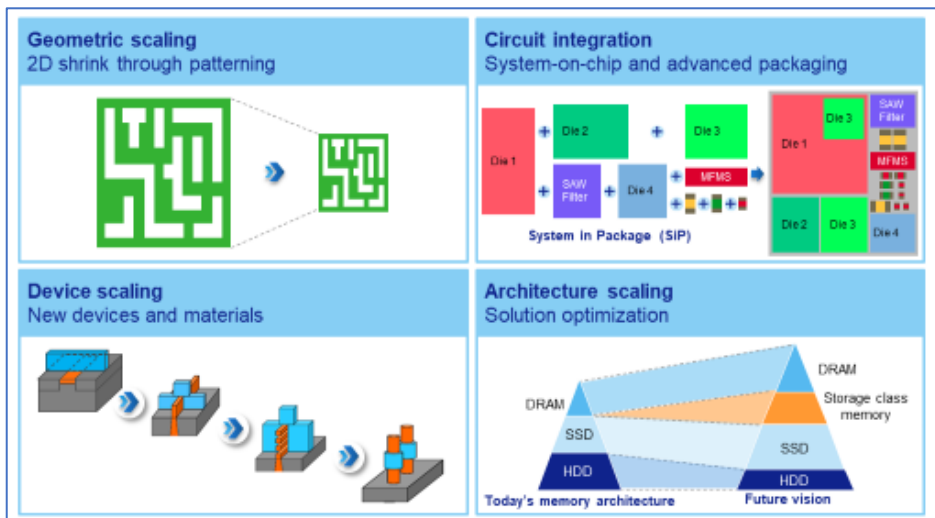


Figure 1: Different drivers for Moore's law; based on input from IMEC and chip manufacturers.

This exponential growth has popularly become known as Moore's law, after Intel co-founder Gordon Moore; in his seminal 1965 publication¹, Moore stated that "the complexity of the minimum component cost has increased roughly a factor of two per year" and he predicted this trend would continue for another decade. This is commonly referred to as "Moore's Law". Later, in his 1975 IEEE article², Gordon Moore updated his prediction into that the components per chip would double every two years rather than every year, as observed from 1959 until 1975. Though it is not a physical law, and

at best can be called an economic law or a conjecture based on a couple of points over a period of a few years, the prediction of Moore has become the guiding principal for the semiconductor industry for the last 50 years. In a later investigation, Kurzweil confirmed and extended Moore's exponential trend retrospectively back to 1900, as shown in Figure 2.

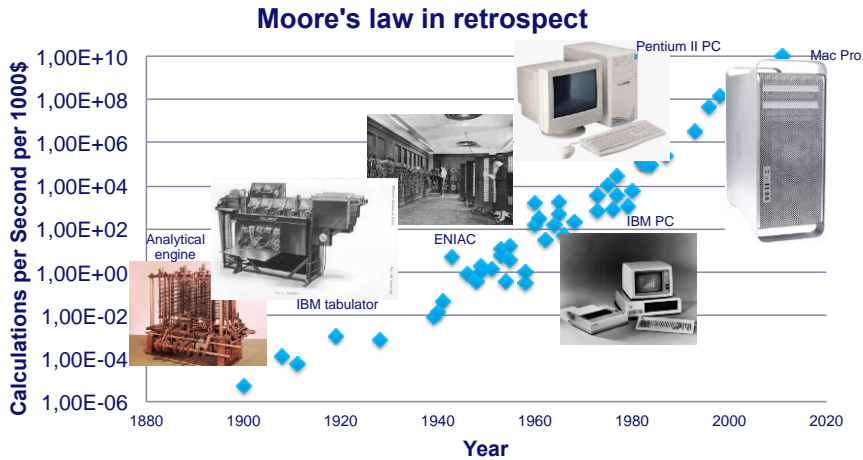


Figure 2: Moore's law in historical perspective³.

Optical lithography has been central to the continuing scaling of integrated chip production, known as Moore's law. Essentially, this has been achieved by reducing the resolution limit, as described in the Abbe resolution criterion:

$$CD = k_1 \cdot \frac{\lambda}{NA} \quad (1.1)$$

With CD the half-pitch of the structure to be printed, λ the wavelength, NA the Numerical Aperture ($NA = n \cdot \sin(\alpha)$, with α the opening angle and n the refractive index of the medium), and k_1 the interference contrast factor⁴.

Evolutionary changes to lithographic tools over the years have seen step-by-step reductions of the wavelength and increases of the NA. Also, the contrast factor k_1 has been reduced by continuous improvements in aberrations and focus/dose control;

lowering k_1 -factors down to 0.4 has also been enabled by 'tricks' like off-axis illumination, polarization and phase-shifting masks. Furthermore, immersion lithography employs water as an imaging medium (with $n=1.4$) to increase the NA to 1.35.

However, in the past decade these evolutionary improvements have run out of steam for the most advanced devices, as these have been stretched by advanced multiple exposures and frequency-doubling schemes. Although enabling Moore's law, these tricks come at the expense of costly additional masks and dwindling process margins.

A revolutionary change in lithography is the recent introduction of Extreme Ultraviolet lithography (EUVL), with a wavelength of 13.5 nm and operating in near-vacuum, to give a resolution limit in the order of 10 nm. For this, the complete lithographic exposure system had to be re-thought, starting from a plasma-based EUV-source to a new type of reflective optics and to moving and clamping parts in the near-vacuum environment.

Even if this technology is complex in itself (as witnessed by the long gap between the first proposals in 1985 by Bell Labs⁵ and the first large-scale-production scanner shipment in 2017), EUV lithography is now fast gaining acceptance as the more cost-effective solution, as compared to aggressive multi-patterning immersion lithography. Also, the superior resolution of EUV results in significantly increased design flexibility, shorter time to yield and superior electrical circuit properties⁶.

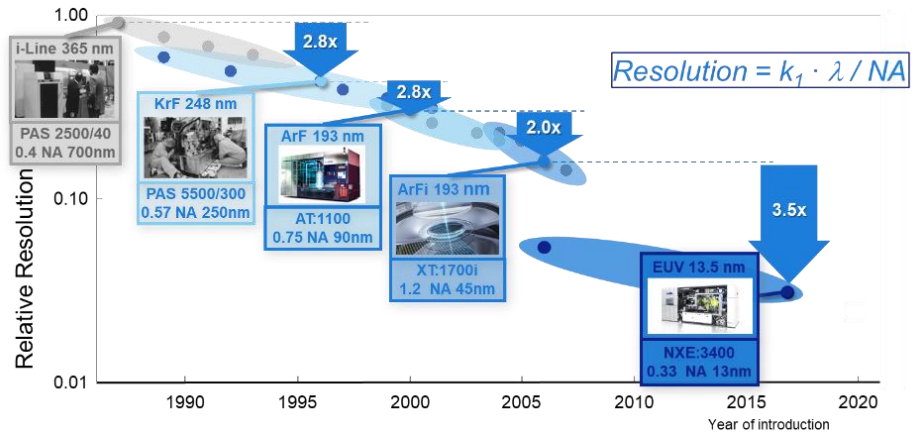


Figure 3: evolutionary improvements in DUV scanners at ASML in past 35 years and the revolutionary jump to EUV.

With the introduction in 2017 of the NXE:3400, with numerical aperture NA=0.33, EUV lithography entered large-scale production⁷. Offering source power of 250 W, and a corresponding throughput of 125 wph (wafers per hour), as well as progressive improvements in overlay, defectivity and availability, this tool has been inserted for production by leading-edge chip manufacturers worldwide, with more than 100 systems installed by 2020. The successor system with higher NA=0.55 is currently in development for even higher resolutions.

1.2. EUV scanner outline

A scanner, or step-and-scan system, is the lithographic tool that lies at the heart of IC manufacturing. In a nutshell it images an object pattern present on a mask, or reticle, onto a photosensitive layer on a wafer. The resulting pattern in the photosensitive layer on the wafer is then developed and the wafer is processed further to create the electrical properties and interconnections that constitute an integrated circuit, layer by layer. Clearly, imaging and focus control are of paramount importance at resolutions approaching 10 nm. In addition, these layers need to be positioned with nm-accuracy with respect to each other, resulting in extremely tight requirements on pattern placement.

In current scanners, the typical magnification factor is $\frac{1}{4}$; in other words, the object pattern on the mask is 4x larger than the pattern as imaged on the wafer. The typical field size is $26 \times 33 \text{ mm}^2$ (at wafer level; so $104 \times 132 \text{ mm}^2$ at mask level). The pattern on the mask is scanned by a slit exposure (to relax the otherwise prohibitive large-field requirements in the projection optics), and this repeated a number of times to fully fill the wafer (which is typically 300mm in diameter), by stepping the wafer to a new position after each scan. Hence the name step-and-scan system.

A full 300 mm wafer can contain ~ 100 full-field chips, such as used for laptop or server CPU and GPU chips, or ~ 1000 small-field chips (which can be fitted 9 or 12 times onto a single reticle to be exposed simultaneously), such as used for mobile applications and memory chips.



Figure 4: Outline of EUV Lithography Scanner. Source: ASML.

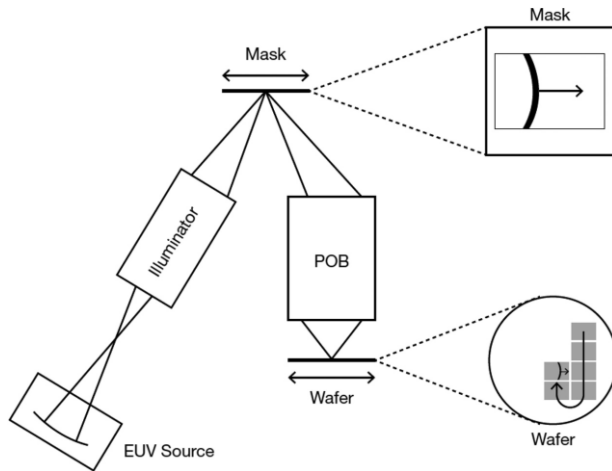


Figure 5: Basic working principle of step-and-scan; the object on a mask (or reticle) is scanned and imaged onto a portion of a wafer, after which the wafer steps to a new position and the process is repeated (source: ASML).

1.3. EUV scanner environment

The EUV wavelength of 13.5 nm is equivalent to a high photon energy of 92 eV. These photons are ionizing for all elements and have a short mean free path in any gas, so the whole system has to be operated at near-vacuum. However, a truly deep-vacuum system turned out to be infeasible as the delicate mirror optics cannot be properly baked out, which resulted in some residual water and hydrocarbons which in turn quickly reduced the reflectivity of the mirrors to unacceptable levels⁸. Therefore, a continuous flow of low pressure hydrogen (H_2) is employed throughout the scanner to continuously remove adsorbed contaminants and prevent oxidation. The small EUV transmission penalty of using low-pressure hydrogen is considered acceptable (absorption coefficient of H_2 is 0.0016 /Pa.m; 5 Pa of H_2 and a total optical path length of ~5 m will result in ~4% transmission loss).

The EUV photons will ionize a fraction of the H_2 gas to create a plasma. The resulting reductive hydrogen plasma will extend several cm's beyond the confines of the EUV beam, while also diffracted and scattered EUV can contribute to the extent of plasma

volume. This needs to be considered carefully in designing the scanner system and materials not just in the beam itself, but also around the beam.

1.4. Contamination and particles

There are two basic types of contamination that may affect scanner operation: chemical contamination and particle contamination, also called defectivity since these result in imaging defects. Examples of chemical contamination are hydrocarbons, outgassing solvents or volatile metal-hydrides, which can lead to film deposits on the mirrors and on the mask (haze formation) and consequent reduction in reflectivity and increased straylight. Examples of particle contamination are submicron metal particles, suspended dust, skin flakes or microfibers. Both will be severely influenced by the presence of the EUV-induced low-pressure hydrogen plasma. This thesis will focus primarily on the particle contamination aspect, while molecular aspects will be briefly addressed in section 6.

Even with perfect imaging and overlay control, device yield can be seriously affected by particles. The optical mirror design is such that no mirror surface is in actual focus, so particles on the mirror surfaces will not image sharply onto the wafer. In theory, they may have minor impact on straylight and overall optical system transmission, but in practice their total surface coverage will be $\ll 1\%$ and this can be ignored.

However, particles that are on either the wafer or the mask will have a direct effect on imaging, by locally absorbing light, which will result in a local dose error. This may result in e.g. unopened contacts or bridging lines and loss of the chip. Assuming a killer defect to be defined by an imaging impact of 10%, the critical particle size at reticle level is found to be ~ 35 nm for the ultimate resolution limit of 13 nm dense lines, and ~ 40 nm for the realistic pitch of 16 nm.

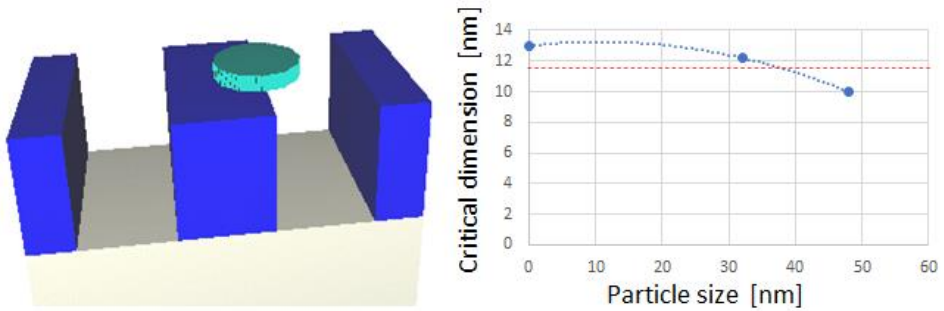


Figure 6: Example of an imaging simulation of a defect for 13 nm dense lines, using dipole illumination and baseline NXE:3400 resist model. Control limit (red) is 10% error in critical dimension.

Mask defectivity is considered to have the biggest impact, since the repeating aspect of mask defectivity can result in potentially zero yield over the full wafer and even for all subsequent wafers, as illustrated in Figure 7. This thesis will focus on advanced particle contamination control for the reticle, but the same physical principles will apply to wafer defectivity.

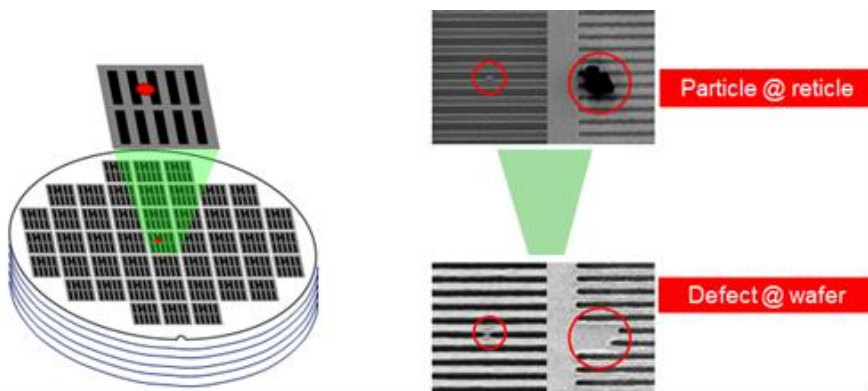


Figure 7: A particle on reticle front side is repeated for each die on wafer (100% yield loss for full field dies)

Particle contamination control aims to break the so-called “chain of defectivity”, whereby particles can release and be transported to the reticle. Generally speaking, particle contamination can be optimized by minimizing the number of particles present (no etching/creation over time), preventing release (no charging, no electric fields), and preventing transport to the reticle (no attractive electric fields).

In principle, it would appear to be sufficient to break the defectivity chain at one point, e.g. by cleaning or by suitable protective flow. However, in view of the extreme defectivity requirements for the scanner and the variety in particle types and sources, in practice all links in the chain must be recognized and addressed: one must use ultraclean parts, defectivity-aware build and service procedures and still one must ensure the scanner is robust against the unavoidable remaining particles⁹. Also, measurability of sub-micron particles on component surfaces is an issue that must be recognized in setting appropriate cleanliness specs.

1.5. *Plasma aspect*

The important contribution of EUV-induced plasma became immediately apparent when the high-power EUV Source could be first used for testing in 2016; until then defectivity testing and optimization was predominantly done without EUV being fired, so resulting defectivity improvements did not typically address these aspects. When defectivity testing was switched to include EUV, a performance deterioration of ~100x was observed, as shown in Figure 8.

Regarding reporting metrics, defectivity is typically measured as added Particles-per-Reticle-Pass (PRP), using a mask inspection tool; and is reported for a standardized particle size, in wafers exposed:

$$PRP = \text{added particles on reticle (of } > 40\text{nm) per } 10000 \text{ wafers } [\#/10k]$$

Every added particle is a serious event in production, resulting in one or more wafer batches having to be reworked and the reticle to be cleaned. And if undetected, a reticle defect can lead to the complete rejection of one or more batches. In view of this impact, the target for the scanner has been set to $PRP < 1/10k$. This is an extremely aggressive target, corresponding to roughly <1 particle of $>40\text{nm}$ per week (assuming ~1500 wafers per day). While a $PRP \approx 1/10k$ is deemed sufficient to enable HVM, full-scale efforts continue to further reduce the number of added particles.

In order to understand and optimize scanner PRP, it makes sense to split this up into a reticle overhead term $PRP_{overhead}$, meaning storage, inspections and clamping withing the scanner, and a wafer exposure term PRP_{EUV} . PRP_{EUV} will scale with number of EUV pulses fired and with time on stage, while $PRP_{overhead}$ will depend on lot size and number of reticle handlings.

$$PRP = \alpha \cdot PRP_{overhead} + \beta \cdot PRP_{EUV} \quad (1.2)$$

Though other contributions might be present, both terms will be strongly influenced by EUV-induced plasma, as will be detailed out in this thesis. For the overhead terms, the main concern is the combination of plasma with clamping electrostatics and resulting risk of discharges and of electrostatic particle attraction¹⁰. For the exposure term, the main concerns are reduction of adhesion and electrostatic release by plasma or EUV. Such plasma effects on release, transport and sticking is consistent with observations from astrophysics and space missions, which have linked phenomena such as lunar glow¹¹, comet tails¹² and dust accumulation on spacecraft¹³ to charging effects on particles by ions, electrons and/or energetic photons in space.

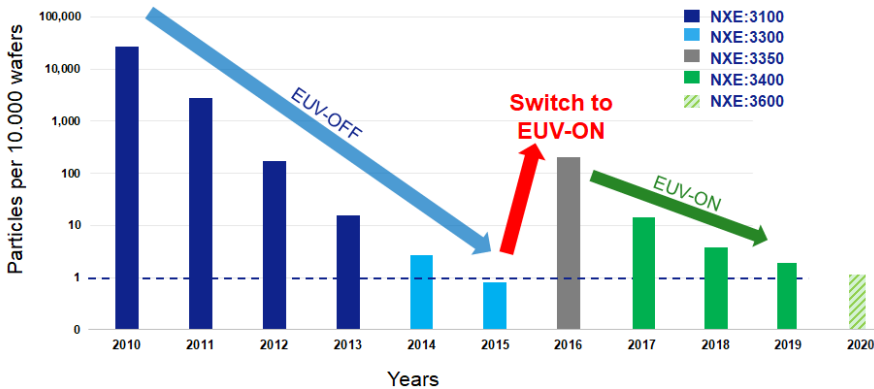


Figure 8: Downward trend in EUV defectivity performance, showing disruption in 2016 by the integration of the high-powered LPP source.

This observed deterioration triggered a targeted effort to improve plasma understanding in terms of particles and to introduce solutions based on that. The

resulting improved plasma understanding has reduced mask particle contamination levels to currently outperform DUV immersion alternatives¹⁴, removing the last major bottleneck from EUV acceptance. Still, there is clear customer value in further improvements and this will undoubtedly remain an area of active investigation for the coming years.

1.6. Pellicle

Besides controlling particle contamination down to effectively zero, as outlined above, another solution for particle contamination of the mask is to apply a so-called pellicle to the mask; this keeps the particles effectively out-of-focus so they do not image sharply anymore¹⁵. However, while this is a tried and proven solution in DUV scanners, in EUV a pellicle comes at a penalty in EUV transmission since EUV is absorbed significantly, even in a pellicle film of <50 nm. Thus, the productivity of the scanner goes down, which translates into a noticeable cost-of-ownership penalty.

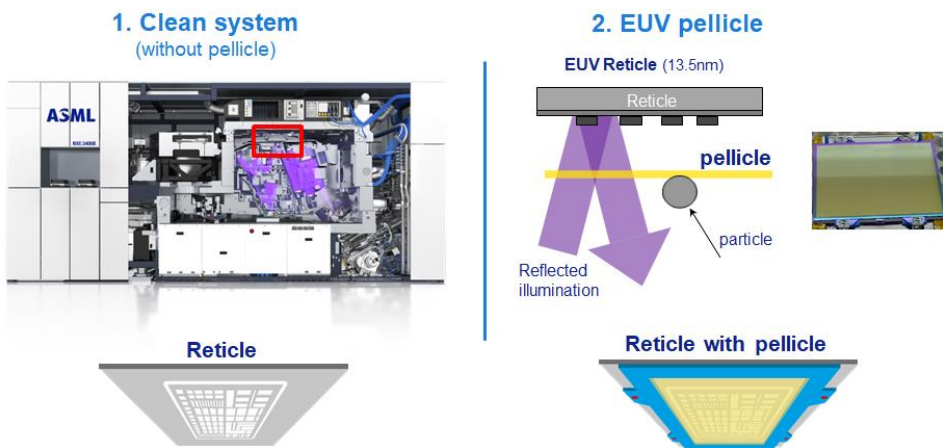


Figure 9: Dual path approach for particle contamination control: left, clean scanner (without pellicle); right, pellicle (relaxing clean scanner requirements)

The optimum of choosing to use a pellicle or not depends on the details of the product, inspection capabilities and defectivity level, and ability to clean particles from mask;

this choice can vary per customer and per product, and even per layer, as discussed by Lercel¹⁶.

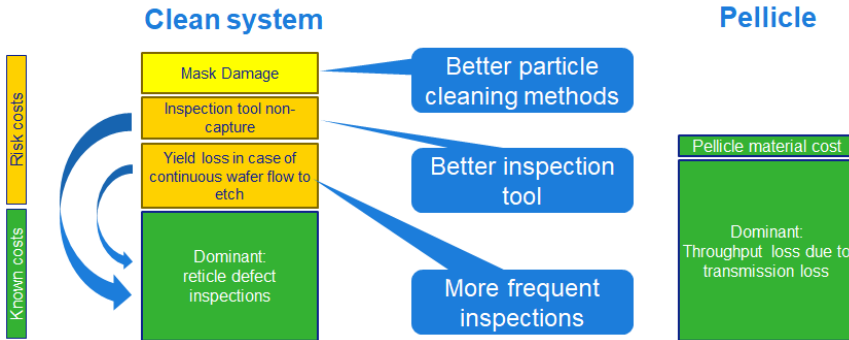


Figure 10: Dynamic cost trade-off between pellicle and clean-system strategy; for the non-pellicle case, known costs and risk costs can be exchanged by optimizing inspection interval and inspection tools.

This thesis will focus on the non-pellicle case, but specific pellicle aspects will be addressed where applicable.

1.7. Adhesion and release

For submicron particles, gravity is essentially negligible because of the exceedingly small mass; similarly, mass-dependent forces like vibrations will be very small. Flow-induced forces may also be ignored in view of the low momentum of the hydrogen molecules, low pressure and the wall effect reducing effective flow speeds. The main adhesive forces in near-vacuum are the Van der Waals force, and chemical bonds via adsorbed hydrocarbons and possibly hydrogen bridges via water, even if capillary forces are not present at these low pressures¹⁷. Contact charging¹⁸ may be ignored, since charge will bleed away to the surface even from poorly conductive particles after several hours, and effectively instantaneously when the conductive EUV-plasma is switched on¹⁹. It should be noted however that capillary forces as well as contact charging and resulting mirror charge attraction²⁰ can be a complicating factor in cleaning parts before closing and pumping down the scanner vessel. Particle materials,

geometries and surface states are intrinsically uncontrolled, which implies that ab initio calculations of adhesion forces cannot be done and that adhesion can vary by orders of magnitude²¹. The main adhesion forces are listed in Table 1, showing that in the near-vacuum state nanoparticles tend to be bound to the surfaces either by Van der Waals forces or covalent bonds (in case of chemisorption).

Table 1: Main adhesion forces for a particle bound to a surface (with r particle radius, γ the surface tension, θ the contact angle, q the charge, D and a distances to the surface, U_0 the bond energy, m particle mass, and g the standard gravity).

Force	Scaling/formula	Order of magnitude for particle $d=100$ nm
Van der Waals (incl. roughness correction C_r)	$C_r \cdot \frac{A_H}{6 \cdot z_0^2} \cdot r$	$\sim e-11 - e-9$ N
Capillary	$4\pi\gamma r \cos \theta$	Negligible at 1-10 Pa
Contact charge and mirror charge	$\frac{qq'}{16\pi\epsilon_0(r+D)^2}$	Negligible in conductive plasma medium
Chemisorption	$\sim U_0/a$	$\sim e-11 - e-9$ N ²²
Gravity	$m \cdot g$	$\sim e-17$ N

Zooming in on the Van der Waals force, this may be written as:

$$F_{vdw} = C_r \cdot \frac{A_H}{6 \cdot z_0^2} \cdot r_p \quad (1.3)$$

With r_p the particle radius, A_H the Hamaker constant, z_0 the minimum separation between surface and particle ($z_0 \cong 0.4$ nm)²³, and C_r an empirical correction factor for a real particle. The Hamaker constant is roughly $A_H \approx 10^{-19}$ J for most practical materials²⁴, resulting in a maximum Van der Waals force of $F_{vdw} \approx 5 \cdot 10^{-9}$ N for a 100 nm particle. However, this maximum Van der Waals force in practice may be significantly lower which is described by the correction term C_r , describing the force reduction by

surface roughness, particle asperities and irregular particle shape; this correction may be in a wide range between $C_r \approx 0.001 - 1^{25}$. The force may be further reduced by adsorbates, although this should be a minor correction at 5 Pa^{26} , but should not be ignored completely as the sensitive scanner cannot be baked out at high temperature so there might still be adsorbates after pump-down. Furthermore, reticles and wafers (fresh from ambient conditions) are continuously cycled through the scanner. The typical Van der Waals force for a 100 nm particle will thus be in a range of 10^{-12} - 10^{-9} N , as illustrated in Figure 11; this range will shift linearly with particle size. This implies that the population of particles cannot be described by single adhesion number, but must always be treated as a range of adhesion forces.

Despite this range the adhesion forces will be large relative to typical release forces for submicron particles. This implies that nanoparticles are very hard to remove or clean.

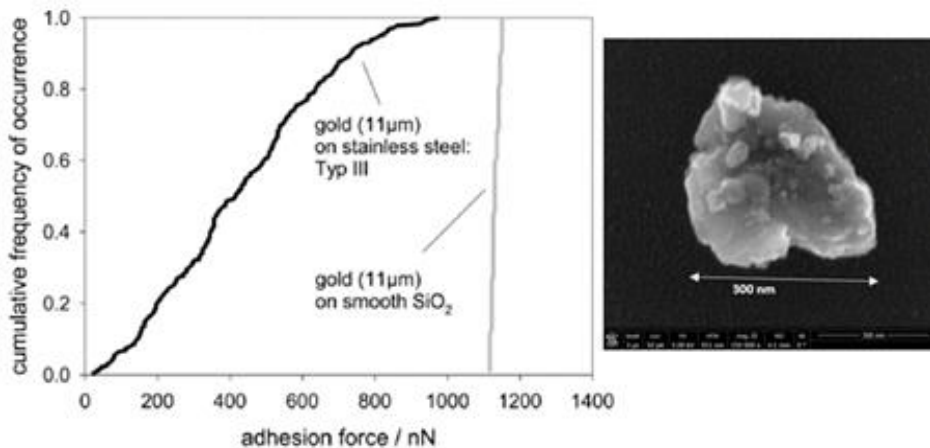


Figure 11: Left, reduced Van der Waals force by surface roughness (from Goetzinger²⁷); right, SEM image of example of actual reticle frontside particle, showing significant roughness and deviations from spherical shape²⁸.

In near-vacuum, besides Van der Waals forces, adsorbed monolayers of water can still be significant, even under near-vacuum conditions²⁹. Plus, at nanoparticle scale, cementation and chemical bonds can be a significant adhesion force¹⁷. Thus, in a vacuum system, most particles will be bound securely to the surfaces and will not release by low-pressure flow or vibrations.

However, the reactive plasma environment can shift the force balance towards release of particles by several mechanisms³⁰: by decomposing bonding adsorbates, by etching away or roughening the surface layers of either particle or substrate, or by charging the particle. Furthermore, the hydrogen plasma may react with some materials which may result in ejection of particles via fragmentation or blistering.

Once released into the plasma bulk (or for free-floating particles) the short-range surface forces of Table 1 become negligible, and the force balance will be dominated by neutral and ion drag forces and electrostatic attraction (Coulomb force). Ion drag and Coulomb forces are determined by the plasma and grounding/biasing details, while the neutral drag force can be independently set by local gas flows. These forces can have different orientations, so care should be taken in the force balance: besides amplitudes also the vector nature of the forces must be considered.

1.8. Transport

The force balance on a free particle is dominated by neutral drag force, ion drag force and coulomb force. Gravity may again be ignored for submicron particles.

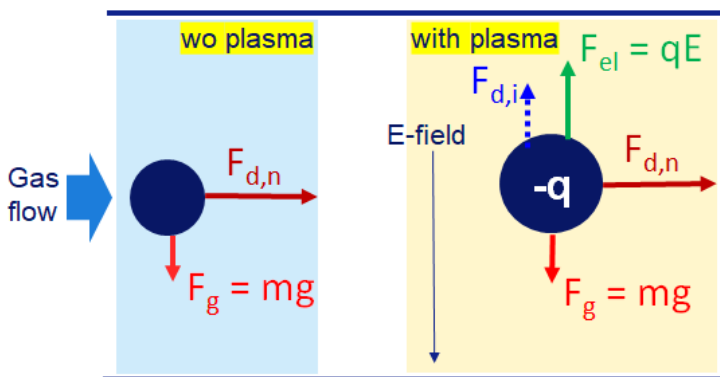


Figure 12: Force balance on free particle; without and with scanner.

Neutral drag force is determined by the gas pressure and the gas velocity. The scanner crossflow is designed to flow parallel to the reticle surface with zero force component

towards the reticle, and a force component away from the reticle above the unavoidable open gap of the EUV beam. The reticle crossflow should be high to minimize residence time of any free particles in the volume beneath the reticle, while avoiding turbulences or backflows; resulting flow speed is to be in order of 100 m/s and the neutral drag force at 5 Pa H₂ is then $\sim 5 \cdot 10^{-15}$ N.

The Coulomb force is the result of the EUV-induced photoelectric emission on the floating reticle surface, which transiently charges the reticle positively. As submicron particles will be negatively charged by the more mobile electrons in the plasma this will result in an attractive electric force on the particles towards the reticle. As the reticle is conductive, the surface charge will extend beyond the plasma and this force will attract particles over a wide area, as shown in Figure 13. In between the EUV pulses, the plasma will compensate the surface charge, and the force drops to zero. Still, averaged over the pulse interval an attractive force results, which is not compensated by the neutral drag force, as this force is orthogonal to the Coulomb force. The Coulomb force will build up over multiple pulses, so the crossflow must be designed such that the residence time of the particle beneath the reticle is minimized and the repeating Coulomb force cannot integrate to a large enough displacement to end up on the reticle surface. Given the aspect ratio of the reticle dimension to the slit height underneath the reticle of $\sim 10:1$, this means the neutral drag force must be at least an order of magnitude higher than the average electrical force.

The ion drag force is the result of momentum transfer from moving ions to charged nanoparticles in the plasma, either by direct impact or by elastic scattering of the ion in the Coulomb field around the nanoparticle. The ion drag force points in the direction of the ion flow, irrespective of the charge of the nanoparticle. During the short transient of the EUV pulse, in the irradiated area ions will be pushed away from the surface as the surface is charged positively by the photoelectric effect, and ion drag will point away from the reticle, counteracting the Coulomb force in the irradiated area. In between the pulses, ion drag is only significant near the plasma-reticle boundary, and will point towards the reticle. Even if the ion drag force may be of same order of

magnitude as the Coulomb force, it only acts in a very limited volume very close to the reticle surface around the EUV beam, and hence it may typically be ignored.

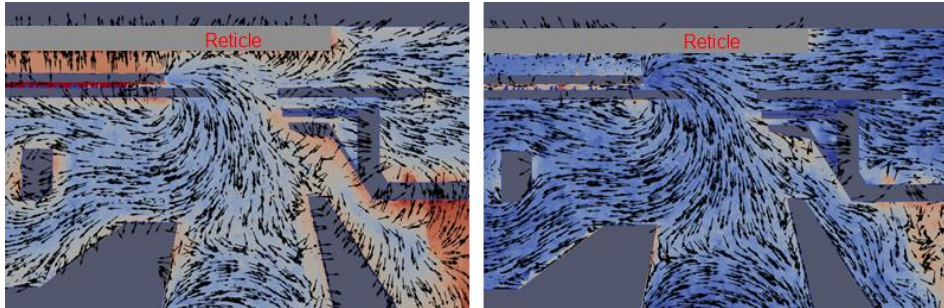


Figure 13: Particle-in-Cell simulations of the force map for a 100-nm diameter particle in the region around the reticle. Left: at the end of the EUV pulse. Right: in between pulses. Red indicates an electrical force higher than the neutral drag force, while blue indicates a lower electrical force; arrows indicate local direction of combined force. Simulations courtesy of ISAN.

1.9. Layout of this thesis

This thesis will outline the characteristics of the EUV-induced plasma within the scanner, focusing on the impact thereof on particle contamination control and on the scanner electrostatics. Section 2 will describe the generation of EUV, and section 3 will detail out how the EUV induces a plasma in the scanner background gas, including modeling aspects and in-situ measurements. Subsequently, section 4 and 5 will go into the electrical interaction between plasma, particles and surfaces, and chapter 6 will describe the physical/chemical interaction between the EUV-induced plasma and materials. Chapter 7 will provide conclusions and recommendations for future investigations.

1.10. References

- ¹ G. Moore, “Cramming More Components onto Integrated Circuits”, *Electronics* (1965)
- ² G. Moore, “Progress in digital integrated electronics”, *Electron devices meeting* (1975)
- ³ <http://www.singularity.com/charts/page67.html>
- ⁴ A. Wong, “Resolution Enhancement Techniques in Optical Lithography”, SPIE Press, Bellingham (2001)
- ⁵ K. Hoh et al, “Feasibility study on extreme UV/soft x-ray projection-type lithography”, *Bell Electrotech. Lab.* (1985)
- ⁶ A. Pirati et al, “EUV Lithography Performance for Manufacturing: Status and Outlook”, *Proc. of SPIE Vol. 9976* (2016)
- ⁷ M. van de Kerkhof et al, “Lithography for now and the future”, *Solid-State Electronics* (2019)
- ⁸ V. Banine et al, “EUV lithography: Main challenges”, *Proc. of SPIE Vol. 5401* (2003)
- ⁹ M. van de Kerkhof et al, “Advanced particle contamination control in EUV scanners”, *Proc. of SPIE Vol. 10957* (2019)
- ¹⁰ M. van de Kerkhof et al, “Plasma-assisted Discharges and Charging in EUV-induced Plasma”, *Journal of Micro/Nanopatterning, Materials, and Metrology* (2021)
- ¹¹ X. Wang et al, “Dust charging and transport on airless planetary bodies”, *Geophysical Research Letters* (2016).
- ¹² T. Nordheim et al, “Surface charging and electrostatic dust acceleration at the nucleus of comet 67P during periods of low activity”, *Planetary and Space Science* (2015)
- ¹³ N. Afshar-Mohajer et al, “Review of dust transport and mitigation technologies in lunar and martian atmospheres”, *Advances in Space Research* (2015).
- ¹⁴ <https://www.anandtech.com/show/16028/better-yield-on-5nm-than-7nm-tsmc-update-on-defect-rates-for-n5> (2020)
- ¹⁵ D. Brouns et al, “NXE pellicle: offering a EUV pellicle solution to the industry" *Proc. of SPIE Vol. 9776* (2016)
- ¹⁶ M. Lercel et al, “EUV reticle defectivity protection options”, *Proc. of SPIE Vol. 11148* (2019)
- ¹⁷ H. Perko, “Theoretical and experimental investigations in planetary dust adhesion”,

PhD thesis, Colorado State University (2002)

¹⁸ Z. Sternovsky et al, “Contact charging of lunar and Martian dust simulants”, *Journal of Geophysical Research: Planets* (2002)

¹⁹ X. Wang et al, “Charge of dust on surfaces in plasma”, *IEEE Transactions on Plasma Science* (2007)

²⁰ G. Peter Castle, “A century of development in applied electrostatics; nothing static here”, *IEEE Transactions on Dielectrics and Electrical Insulation* (2011)

²¹ M. van de Kerkhof et al, “Advanced particle contamination control in EUV scanners”, *Proc. Of SPIE Vol. 10957* (2019)

²² B. Hammer et al, “CO chemisorption at metal surfaces and overlayers”, *Phys. Rev. Letters* (1996)

²³ H. Krupp, “Particles adhesion theory and experiment”, *Advances in Colloid and Interface Science* (1967)

²⁴ L. Bergström, ‘Hamaker constants of inorganic materials’, *Advances in Colloid and Interface Science* (1997)

²⁵ J. Israelachvili, “Intermolecular and surface forces”, 3rd edition, Academic Press, London (2011)

²⁶ H. Perko et al, “Surface cleanliness effect on lunar soil shear strength”, *Journal of Geotechnical and Geoenvironmental Engineering* (2001)

²⁷ M. Goetzinger et al, “Particle Adhesion Force Distributions on Rough Surfaces”, *Langmuir* (2004)

²⁸ S. de Vries, internal ASML report (2018)

²⁹ H. Perko, “Surface cleanliness based dust adhesion model”, *Space* (1998)

³⁰ M. van de Kerkhof et al, “Particulate and molecular contamination control in EUV-induced H₂-plasma in EUV lithographic scanner”, *Proc. of SPIE Vol. 11489* (2020)

2

EUV generation and spectrum

This chapter is based on following publication:

- *Mark van de Kerkhof, Fei Liu, Marieke Meeuwissen, Xueqing Zhang, Muharrem Bayraktar, Robert de Kruij, Natalia Davydova, “High-power EUV lithography: spectral purity and imaging performance”, Journal of Micro/Nanolithography, MEMS, and MOEMS (2020)*

2.1. Introduction

The Laser Produced Plasma (LPP) as used in the ASML EUV scanner systems, generates EUV by pulsed irradiation of Sn droplets by a 10.6 μm wavelength CO₂ laser¹. Pulse frequency is 50 kHz, and pulse length is <100 ns, as sketched in Figure 1. Nominal EUV energy per pulse is 5 mJ, to give an output of 250 W.

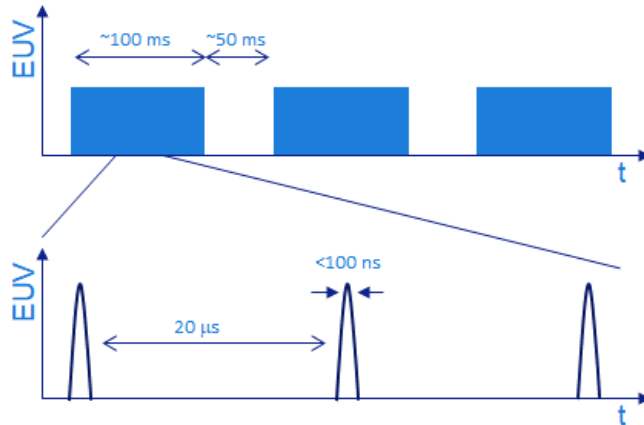


Figure 1: Sketch of EUV pulse train (top) and individual pulses (bottom).

The narrow-band 13.5 nm wavelength is created by the resonance peaks of multiply ionized Sn ions², plus a broadband thermal spectrum. Away from the main 13.5 nm resonant peak, the spectrum can be approximated as Planck-like blackbody radiation, with details that will depend on the plasma parameters which in turn are determined by source operating conditions. In general, out-of-band EUV (outside of the primary band of 13.2-13.8 nm) is undesirable, since it might cause spurious mirror heating for the scanner mirrors. Further downstream this out-of-band EUV will be step-by-step reduced by the repeated selective reflectivity of the consecutive narrow-band Bragg-type multi-layer (ML) mirrors, so it does not contribute to imaging (or image contrast degradation) at wafer level³. The VUV component between 70 nm and 110 nm is also effectively suppressed by absorption by the background hydrogen gas⁴; however, this suppression becomes less effective above 110 nm. The narrow-band ML mirrors mitigate the UV component, especially in the range between 110 nm and 200 nm. Figure 2 shows the H₂ photoionization and photo-dissociation cross section from 50 nm to 115 nm, and the spectral filtering by the ML mirrors.

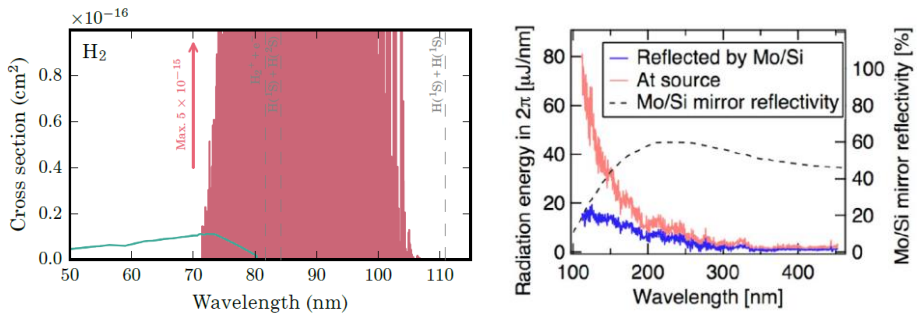


Figure 2: Left: Cross sections of H₂ molecules and absorption zones beneath 110 nm, with photo-dissociation in red and photoionization in green; from Heays⁴. Right: suppression of UV spectrum below 200 nm by a single ML mirror reflection and absorption to create LPP source output⁵.

Typical photoresists at wafer level are based on organic molecules that are intrinsically sensitive to UV light from 150 to 300 nm, resulting in possible contrast loss⁶. This imposes strict requirements on the UV/EUV ratio in resist at wafer level for EUV scanners.

Even if the out-of-band radiation does not reach the wafer, the detailed source spectrum is still relevant for the EUV-induced plasma in the scanner, as the ionization cross section and secondary electron yield are significantly higher for longer wavelengths and significant spectral content might be present in the band around 50 nm (see e.g. Figure 4). Differences in VUV/UV spectra are also a concern when translating findings from off-line EUV/plasma setups to scanner, as many off-line sources have significantly higher VUV/UV content.

2.2. LPP EUV generation

High-power LPP systems achieve high Conversion Efficiency (CE) by using two closely timed IR-laser pulses per EUV pulse, in order to both optimize EUV emission by the Sn ions and reduce the opacity of the outer layers⁷. First, the pre-pulse shapes and expands the liquid Sn droplets into a 2D pancake-like shape, reducing the Sn density and opacity in the direction of EUV emission. Next, the short energetic IR pulse increases the electron temperature to 30-60 eV and the ion density to $\sim 10^{24}$ - 10^{25} m⁻³,

for optimum EUV emission. The high-level LPP EUV source operation scheme is shown in Figure 3.

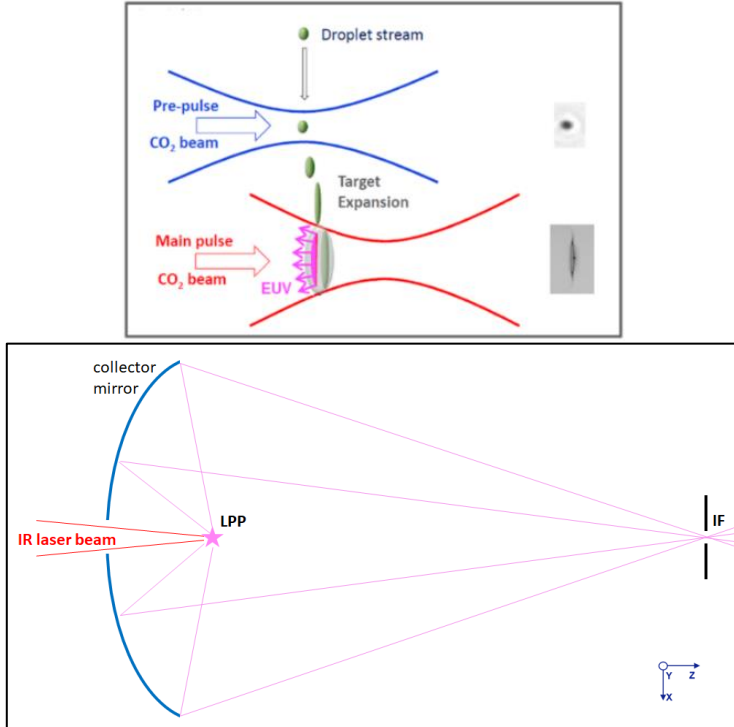


Figure 3: Principle of double-pulse scheme of high-power LPP EUV source; EUV is emitted backwards in a half-sphere and is reflected by a collector mirror into the scanner. Bottom: normal-incidence collector mirror and imaging of primary LPP plasma emission onto Intermediate Focus (IF) at Source output point.

As the tin target is expanding from the pre-pulse, a high-power (>20 kW), 10.6 μm wavelength short-pulse CO₂ laser Main Pulse (MP) beam is used to rapidly heat and ionize the disk-like tin target. An intensely hot plasma with a temperature of several 10's of eV is generated, and it efficiently emits EUV radiation by multiply ionized Sn ions on top of blackbody radiation, in accordance with Wien's classical law⁸:

$$\lambda_{max} [nm] \cong 3 \cdot 10^6 / T_e [K] \cong 250 / T_e [eV] \quad (2.1)$$

Which corresponds to a plasma electron temperature of ~ 20 eV for $\lambda_{\max} = 13.5$ nm⁹. In practice, this approximation turns out to be a lower boundary and LPP EUV production at $\lambda = 13.5$ nm was found to be most efficient at $T_e = 30$ -100 eV¹⁰.

2.3. LPP VUV and UV emission

Besides EUV, also VUV and UV are emitted as blackbody radiation and from lower ionization states of Sn, especially from the slightly cooler periphery of the Sn plasma, and during cooling-down of the plasma¹¹. The resulting VUV and UV spectrum is a function of the target shaping and source operating conditions. The UV/EUV ratio closely correlates with the IR-to-EUV conversion efficiency (CE), which means that this ratio may be expected to stay constant or decrease as EUV power is increased for future generations.

A more uniformly hot Sn plasma, by optimized pre-pulse, will help to reduce the energy in these unwanted wavelength bands, and concentrate energy in the EUV wavelength band. More mass-limited targets, such as smaller Sn droplets, will also help to reduce the energy in the out-of-band radiation, as is illustrated in Figure 4; this should be balanced again absolute EUV power and droplet stability.

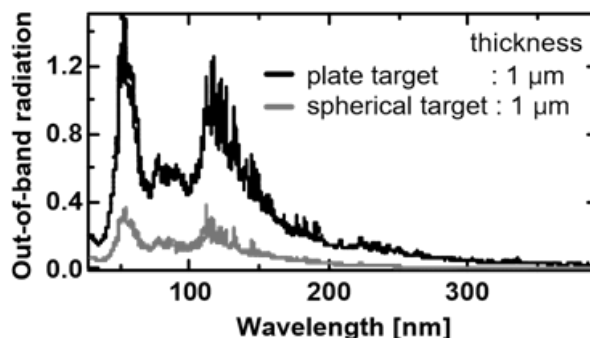


Figure 4: Full-spectrum out-of-band measurement by Sakaguchi, comparing extended Sn plate target to mass-limited Sn droplet target, showing ~ 4 x less out-of-band radiation for mass-limited droplet¹¹.

Increasing the IR laser pulse energy also helps to improve the ratio of UV/EUV, since EUV emission increases more strongly than UV emission due to the resulting increase in electron density and electron temperature¹². This was confirmed by in-house measurements on a LPP proto, as shown in Figure 5. Whether this continues to hold as pulse energies continue to increase is an open question, as the UV/EUV curve can be seen to start to flatten out for highest IR pulse energies.

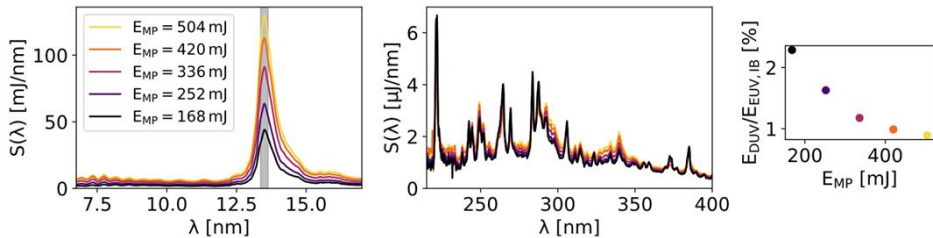
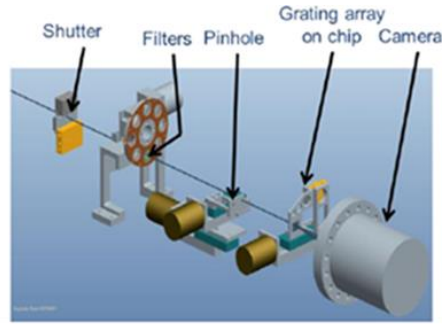


Figure 5: Measurement of EUV and UV for increasing IR laser pulse energies on LPP proto, showing linear increase in EUV output versus minor increase in UV, resulting in an improving UV/EUV ratio for higher IR pulse energy¹³.

2.4. VUV and UV spectrometry

VUV and UV spectra were measured directly on the EUV-producing Sn-plasma, from a metrology port orthogonal to the drive laser axis using a broadband transmission grating spectrometer developed by University of Twente¹⁴. For the UV spectra measurements, the camera integration time was set to 0.5 s, and therefore each spectrum is the result of averaging approximately 25000 EUV pulses, given the 50 kHz frequency of the LPP source. The detailed spectral measurement setup is shown in Figure 6.



(a)

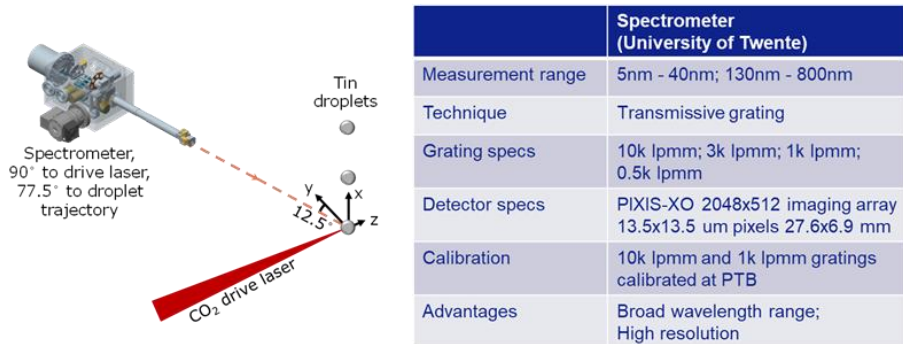


Figure 6: Top: Key components of EUV transmission grating spectrometer; bottom left: schematics of spectra measurement setup; bottom right: spectrometer specifications sheet; from Bayraktar¹⁵ and Liu¹⁶.

Figure 7 shows spectra from 10 nm to 60 nm, measured on a LPP proto system. Two sets of data which were acquired under the same source operation condition but at different time are plotted to show the good reproducibility. The spectrometer is accurate in the range of interest around 13.5 nm, but above 25 nm the measured spectrum is disturbed by the high diffraction orders from the main peak around 13.5 nm; for this spectral range (25-60 nm) novel measurement techniques are currently being investigated. Figure 7 also shows the normalized EUV spectra comparison between a 125W and a 250W LPP source, zooming in on the 7-16 nm range. The higher power source has a slightly better spectral purity above 13.5 nm due to higher MP power density and resulting higher electron temperature and density in the Sn plasma.

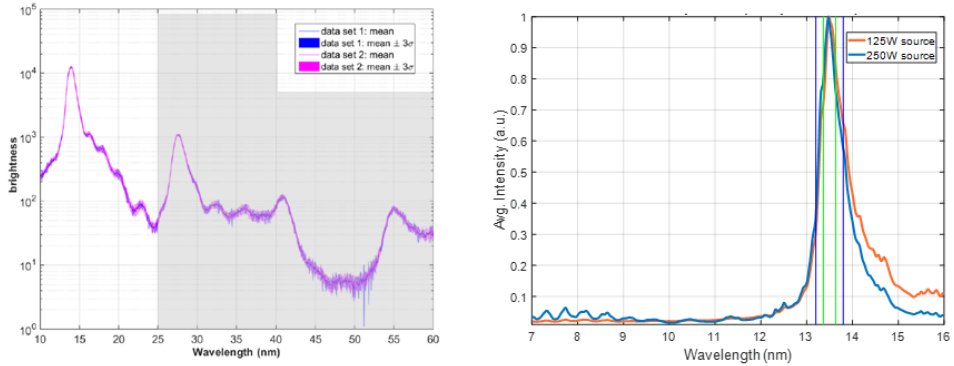


Figure 7: Left: EUV spectrum as measured for wavelength range of 10 nm to 25 nm; for $\lambda > 25$ nm, higher diffraction orders from the grating result in major measurement artefacts. Right: Zoom-in on 13.5 nm region of EUV spectra from 125W and 250W source; 250W source clearly shows better spectral purity.

Figure 8 shows the spectrum from 130 to 400 nm, normalized to the EUV power; the UV/EUV ratio is comparable between source powers of 125 and 250 W. Besides continuous blackbody radiation, UV emission lines may be identified from the lower ionization states of Sn: Sn^{1+} , Sn^{2+} , Sn^{3+} .

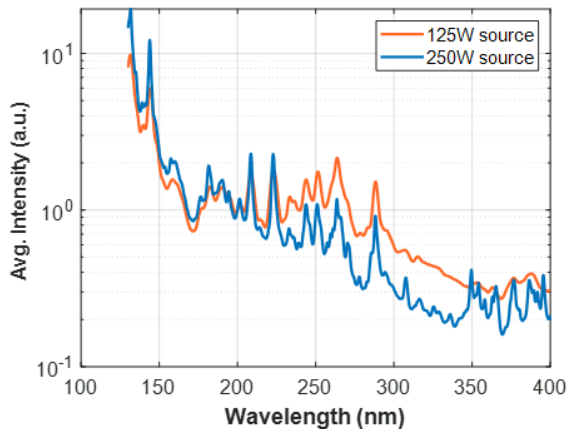


Figure 8: UV spectra directly measured from Sn plasma and normalized to the EUV power; ratio UV/EUV is roughly the same for both 125W and 250W.

2.5. UV at wafer level and imaging impact

As outlined above, the VUV is strongly attenuated by the series of multilayer mirrors in the scanner and the hydrogen background gas. At reticle the VUV/EUV ratio is less than 1%, and <0.1% reaches the wafer, so this is no concern for imaging and may also be neglected for in terms of plasma characteristics. The UV is not absorbed by the gas and reasonably reflected by the mirrors, so will reach both reticle and wafer. Using the UV reflectivities of the scanner mirrors, the UV spectrum of the Sn plasma may be translated to wafer level, as illustrated in Figure 9. The overall UV level at reticle may be expected to be in range of 1-5%, and at wafer to be in range of 0.5-2%.

Since some unknowns remain in this estimate, such as the UV emission angular dependency of the plasma, and the wavelength-dependent sensitivity of the photoresist, the final UV performance qualification is done at wafer level, based on dose-to-clear exposure measurements in resist. In this standardized qualification test, reticles with both multilayer (ML) and chromium areas are exposed through dose to determine the dose-to-clear for EUV and UV respectively⁶; Cr has a high UV reflectance of ~60% for wavelengths above 190 nm and very low EUV reflectance <0.05%. In practice, UV/EUV ratio is determined in a specific test resist (typically EUVJ-3030; sensitive up to ~300 nm) as the ratio of dose-to-clear from ML reticle E_0^{ML} , and the dose-to-clear from Cr reticle E_0^{Cr} :

$$UV/EUV = E_0^{ML} / E_0^{Cr} \cdot 100\% \quad (2.2)$$

This is an average value for the entire UV wavelength range up to 300 nm. Typical measured performance for an NXE:3400B with an optimized LPP source is ~0.5% in resist at wafer level (see also Figure 9). This may be translated to an estimated ~1.5% UV/EUV ratio at reticle level.

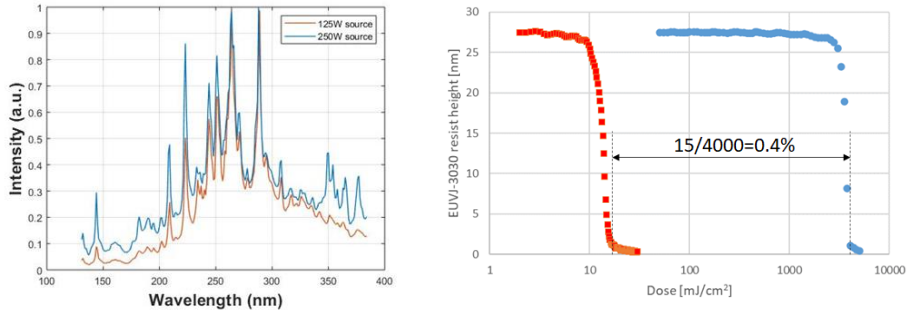


Figure 9: Left: translation of UV spectra from 125W source and 250W source to wafer level; note that the wafer level spectra are derived from measurement directly at LPP source and have been normalized to their respective peak values. Right: dose-to-clear curves for EUV (red) and UV (blue) showing 0.4% UV/EUV ratio.

Properly designed EUV resists are not sensitive to UV light above 300 nm¹⁶, while wavelengths below 110 nm are not transmitted through the hydrogen background gas, and wavelengths below 200 nm are effectively suppressed by the ML mirrors. Thus, main focus should be on the range of 200-300 nm.

Since the longer wavelengths of UV cannot carry the fine spatial information of the patterns to be imaged by EUV, it may be treated as a form of straylight. This contribution is relatively uniform over the field, and at a level of ~0.5% UV it will give a small bias in Critical Dimension (CD) that may be ignored in practice. However, at the edge there may be some spillover of UV from the image border, which may lead to an edge CD shift, as outlined in Figure 10. At the corners, the edge spillover from three neighboring fields add up and the corner CD shift will increase to three times the edge CD shift. This is mitigated by placing a so-called black border around the image field on the reticle, with ultralow reflectance for both EUV and UV.

The regular Ta-based EUV absorber is insufficient for this purpose as it still has up to 2% EUV reflectance, as well as ~15% DUV reflectance, which could result in >1 nm edge/corner CD-shifts.

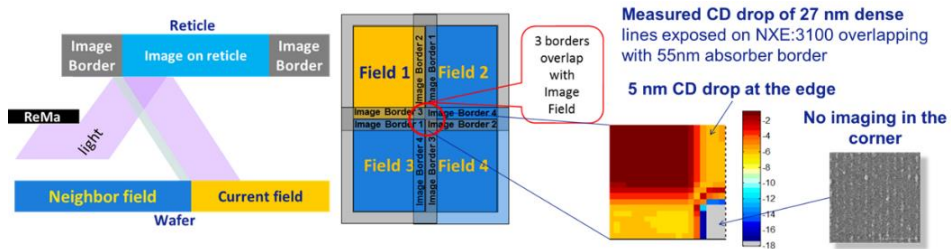


Figure 10: Illustration of need for non-reflective image border and non-reflective Reticle Masking blades to avoid spurious exposure of neighboring fields by EUV and/or DUV⁶.

To investigate the UV contribution to edge and corner CD performance, imaging qualification tests have been carried out with and without a Dynamic Gas Lock membrane (DGLM) above the wafer, which acts as a spectral purity filter¹⁷. Off-line tests at the Physikalisch-Technische Bundesanstalt (PTB) in Berlin measured >99% UV suppression by the DGLM¹⁷. In this qualification test, FWCDU (Full-Wafer CD Uniformity) wafers were exposed on same day just before and directly after building in of the DGLM, and the respective intra-die fingerprints (corrected for reticle writing errors and shadow-correction) were compared to determine the crosstalk impact of UV from neighboring fields. The intra-die fingerprint results in Figure 11 show that for both with and without DGLM the corner and edge Δ CD are all <0.1 nm (which is within N5 and N3 node requirements). By the introduction of a DGLM this is further reduced to ~0.04 nm; this small residual cannot be attributed to UV and is most likely due to spurious EUV reflections and/or straylight.

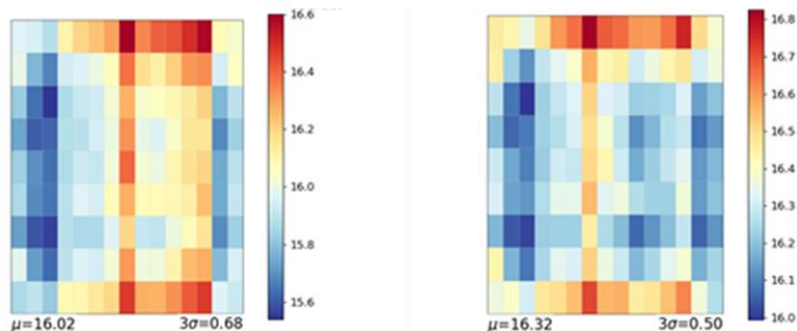


Figure 11: Intra-die fingerprint of 16 nm Dense Lines/Spaces, showing almost identical edge/corner effect without (left) and with (right) DGLM; common fingerprint in X was caused by a sub-optimal scanner calibration. Common edge/corner effect is attributed to EUV reflections, while delta edge/corner effect may be due to UV.

2.6. UV afterglow and impact on plasma

The Sn plasma will peak in EUV emission within a few tens of nanoseconds and will simultaneously swiftly expand. By the end of the IR pulse, as the plasma is colder and the density of the plasma reduces by expansion, the ions will start to recombine and emission will shift from EUV to UV. This will lead to a UV afterglow that will persist for some fraction of a microsecond after the EUV itself has died out. Indeed, significant UV afterglow has been measured for extended solid-state targets¹⁸, but for mass-limited droplet targets this should be (much) smaller as the ion density will drop fast in the expanding droplet. Also, the expanding droplet will exceed the size of the primary focus that is transmitted through IF, which means that not all UV light will be transmitted into the scanner (see Figure 3). Still as long as the emission is within a region around primary focus of $\sim 1 \times 1 \times 1.5$ mm³ (larger in Z-direction than in radial direction), an appreciable amount will be transmitted into scanner; see Figure 12. Taking the velocity of 10-30 eV Sn ions to be roughly 4-7 km/s and predominantly in Z-direction, the timescale for the recombining plasma to go out of focus may be estimated to be ~ 0.2 - 0.35 μ s.

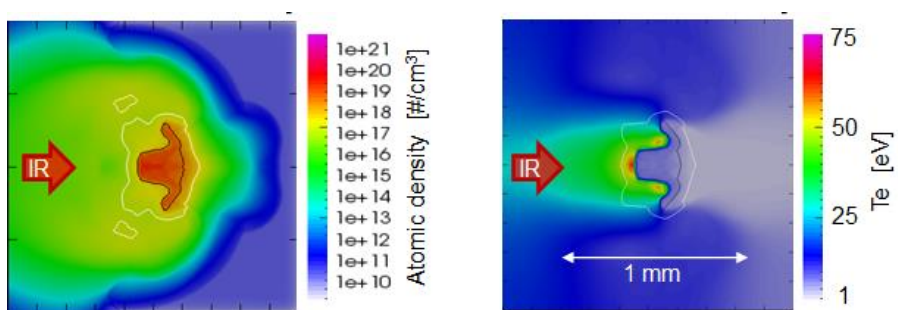


Figure 12: The droplet at the start of the IR pulse; showing the region of high atomic density of the Sn target and the hot plasma in front of it. Simulation courtesy of ISAN.

This estimate for the delay is of course rather handwaving, but currently no measurement techniques are available that are both time-resolved and spectrally

resolved for this part of the spectrum. As shall be seen in subsequent sections, this UV afterglow may have a major impact on the EUV-induced plasma in the scanner.

2.7. Conclusion

The principles of EUV generation by laser-produced plasma (LPP) were presented. Besides EUV this gives rise to VUV and UV spectral components that may impact imaging as well as scanner plasma characteristics. It is shown that VUV is absorbed by the mirrors and the gas in the scanner, and may be neglected at both reticle and wafer level. VUV may impact offline test setups with less attenuating mirrors, so must be considered in translating results of these setups to scanner. UV is not absorbed strongly in scanner and might impact resist imaging at wafer level, though this has been shown to be minor. The plasma impact of UV will be discussed in the next sections, where it will be shown that especially the UV afterglow, which may last for 0.2-0.35 μs after the EUV pulse, may impact the scanner plasma. Again, the UV/EUV ratio might be different for offline test setups, and especially for different source types; this must be taken into account in translating results of these setups to scanner.

Measured source emission spectra from high power EUV sources were presented, showing that UV/EUV ratio is roughly constant or may even improve for increasing source power. Thus, EUV imaging performance is robust against variations in CE and targeting. In principle, this also opens opportunities to optimize the LPP source independently for both power, imaging and desired plasma characteristics.

2.8. References

¹ N. Bowering et al, “Performance results of laser-produced plasma test and prototype light sources for EUV lithography”, J. Micro/Nanolith. MEMS MOEMS (2009)

² O. Versolato, “Physics of laser-driven tin plasma sources of EUV radiation for nanolithography”, Plasma Sources Science and Technology (2019)

-
- ³ M. van de Kerkhof et al, “High-power EUV lithography: spectral purity and imaging performance”, J. Micro/Nanolith. MEMS MOEMS (2020)
- ⁴ A. Heays et al, “Photodissociation and photoionisation of atoms and molecules of astrophysical interest”, A&A (2017)
- ⁵ H. Sakaguchi et al, “Absolute evaluation of out-of-band radiation from laser-produced tin plasmas for extreme ultraviolet lithography”, Applied Physics Letters (2008)
- ⁶ N. Davydova et al, “Impact of an etched EUV mask black border on imaging: part II”, Proc. of SPIE Vol. 8880, Photomask Technology 2013 (2013)
- ⁷ I. Fomenko et al, “Light sources for high-volume manufacturing EUV lithography: technology, performance, and power scaling”. Advanced Optical Technologies (2017)
- ⁸ G. Wannier, ‘Statistical Physics’, Dover Publications. [Chapter 10.2] (1987)
- ⁹ H. Nishimura et al, ‘Development of extreme-ultraviolet light source by laser-produced plasma’, Review of laser Engineering (2008)
- ¹⁰ I. Fomenkov, EUV Source Workshop, edited by V. Bakshi (2018)
- ¹¹ H. Sakaguchi et al, “Spectroscopy of out-of-band radiation from laser-produced tin plasma of euv light source”, <http://www.ile.osaka-u.ac.jp/zone1/public/publication/apr/2006/pdf/3/3.17.pdf> (2006)
- ¹² F. Torretti et al, “Spectral characterization of an industrial EUV light source for nanolithography”, J. Phys. D: Appl. Phys. (2020)
- ¹³ E. Davis, internal ASML report (2019)
- ¹⁴ M. M. Bayraktar et al, “Broadband transmission grating spectrometer for measuring the emission spectrum of EUV sources”, NEVAC blad 54 (2016)
- ¹⁵ M. Bayraktar et al, “Broadband Spectral Characterization of EUV light Sources with a Transmission Grating Spectrometer”, EUV Source Workshop, Dublin (2017)
- ¹⁶ F. Liu et al, “Lithography machine in-line broadband spectrum metrology”, EUVL Workshop, Berkeley (2019)
- ¹⁷ M. van de Kerkhof et al, “Enabling sub-10nm node lithography: presenting the NXE:3400B EUV scanner”, Proc. of SPIE Vol. 10143 (2017)
- 18 H. Sakaguchi et al, “Spectroscopy of out-of-band radiation from laser-produced tin plasma of euv light source”, <http://www.ile.osaka-u.ac.jp/zone1/public/publication/apr/2006/pdf/3/3.17.pdf> (2006)

3

EUV-induced plasma and scanner confinement

This chapter is based on following publication:

- *Mark van de Kerkhof, Andrei Yakunin, Dmitry Astakhov, Maarten van Kampen, Vadim Banine, "EUV-induced Hydrogen Plasma and Confinement in Scanner", Journal of Micro/Nanopatterning, Materials, and Metrology (2021)*

3.1. Introduction

EUV Lithography uses 13.5 nm EUV radiation, which is generated in pulsed mode operation by a Laser-Produced Plasma (LPP) in the EUV Source. Theoretically, it would be ideal to do EUV lithography in vacuum conditions since EUV photons are absorbed

by any medium. However, in practice a background gas of roughly 5 Pa hydrogen (H_2) is used, to maintain self-cleaning conditions for the sensitive EUV mirrors. Hydrogen was chosen as background gas, because of the low EUV-absorption and high chemical activity of H-radicals and ions¹. This gas is excited into a low-density H_2 plasma by the EUV radiation. Detailed understanding of the EUV-induced plasma is crucial, as this creates a chemically reactive environment for both the mirrors, the reticle and the surrounding construction materials.

Although most of the described physical mechanisms are generic for any radiation-induced plasma, this section will zoom in on the specific case of a confined plasma, meaning that the dimensions of the walls confining the plasma are of same order of magnitude as the mean free path lengths of the electrons and ions. Specifically, the plasma details of the so-called Reticle Mini-Environment (RME, see Figure 1) will be worked out in detail. This area is of particular interest for plasma-reticle interactions and particle contamination control². Mutatis mutandis, the same underlying physics will apply to other areas of the scanner.

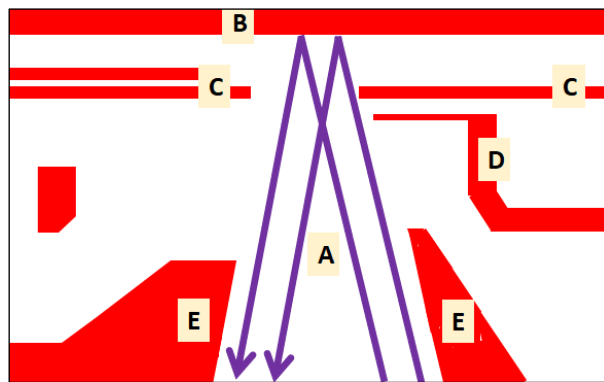


Figure 1: Schematic of scanner Reticle Mini-Environment (RME), showing EUV beam (A), reticle surface (B), reticle masking blades (C), uniformity correction fingers (D) and beam confinement (E).

3.2. EUV beam

EUV light is commercially generated from a hot plasma. The dominant EUV Source technology is laser-produced plasma (LPP), in which pulsed bursts of EUV are emitted by a tin (Sn) plasma which is created by an intense pulsed IR laser. An intensely hot plasma with a temperature of several 10's of eV is generated, which efficiently emits EUV radiation at the primary resonances of multiply ionized Sn around 13.5 nm³, plus broadband blackbody radiation. However, this spectrum is filtered by the series of narrow-band Bragg-reflection mirrors in the scanner, so the photon spectrum inside the scanner at reticle and wafer level may be assumed to be 13.5 nm ($\pm 1.5\%$)⁴. This is in contrast to many laboratory setups, which are often based on EUV sources using grazing incidence collector optics without inherent spectral filtering.

Besides EUV, also UV is emitted as lower ionization states and as blackbody radiation. UV is generated mainly in the cooler parts of the Sn plasma, and during cooling-down of the Sn plasma. For a properly optimized Sn plasma, the UV contribution will be in order of ~1%, and may be ignored during the EUV pulse. However, the UV afterglow may persist for some fraction of a μ s during the cooling-down and recombination phase of the Sn plasma, after EUV generation has stopped. From depth of focus and ion velocity estimates, it may be estimated that the UV afterglow duration could be ~0.2-0.35 μ s. Even at ~1% of the EUV intensity, such a UV afterglow might influence the scanner plasma by efficient photo-emission of relatively cold electrons from surfaces around the EUV beam, as will be described in this section.

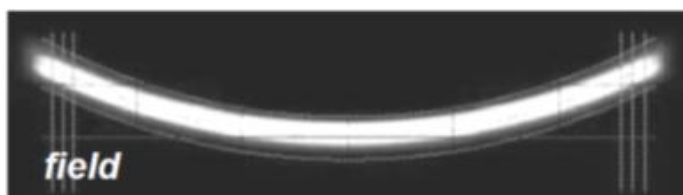


Figure 2: EUV beam cross section close to reticle⁵.

Generally speaking, the EUV power will be reduced by ~30-35% at every mirror reflection⁶, so will decrease stepwise from Source to wafer. However, as the beam is focused and defocused by the optical power of the mirrors, the EUV irradiance will vary in a more complex manner⁵. At reticle level, in the RME, the EUV power is attenuated to roughly 50 W, and the EUV beam is essentially rectangular in shape (actually the rectangle is somewhat curved, see Figure 2), with a slit length of about 11 cm and width in scanning direction of about 1 cm. The intensity distribution may be considered uniform in slit direction and roughly Gaussian in the scanning direction. The main EUV properties for a 250 W LPP Source at RME are summarized in Table 1:

Table 1: EUV beam properties at RME for 250 W LPP Source

Parameter	Value
EUV power at reticle	50 W
Beam dimensions	11 x 1 cm ²
Photon flux	~10 ²¹ s ⁻¹ .m ⁻²
Photon energy	92 eV (±1 eV)
Pulse frequency	50 kHz
Pulse length	<100 ns

3.3. EUV-induced plasma

Photoionization by the high-frequency pulsed EUV results in repeating cycles of plasma generation, expansion, cooling and recombination; with sharp transients around the short <100 ns EUV pulse and a repetition period of 20 μs. Electrons are created by ionization of gas molecules, photo-electric effect and secondary electron emission from plasma-facing surfaces; and are lost by absorption at these surfaces. Ions are created by photoionization and lost by recombination at the walls. At higher ionization degrees, also volume recombination will result in loss of ions and electrons. Several phases can be distinguished (transition moments are indicative and will depend on pressure, power and plasma geometry), as outlined in Figure 3:

0 – 0.2 μs	Photo-ionization and photo-electric electrons
0.2 – 1 μs	Secondary ionization, fast electron cooling, fast expansion
1 – 20 μs	Ambipolar diffusion, decay and slow electron cooling
20 μs	Next EUV pulse: repeat

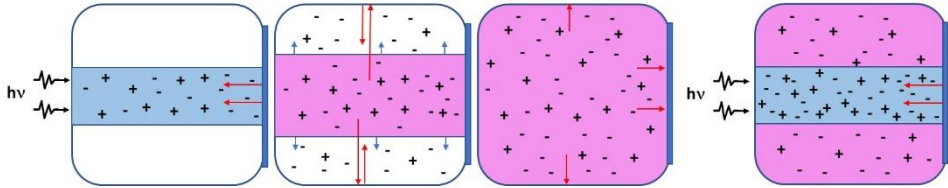


Figure 3: Phases of pulsed EUV-induced hydrogen plasma, showing (a) primary ionization and photoelectric effect, (b) expansion and electron exchange, (c) diffusion and decay, and (d) next EUV pulse. Red arrows indicate main electron fluxes to and from mirror surface (on the right) and other walls.

These phases will be described in more detail in the following sections.

3.3.1. Plasma basics and equations

The definition of a plasma is a quasi-neutral ionized gas governed by the strong interaction between electrons and ions, and by the different thermodynamical properties of each species. This state may be created by e.g. discharges, or by ionizing radiation such as EUV. A textbook plasma will be in local thermal equilibrium (LTE), and the electron energy distribution will be Maxwellian. Based on these assumptions, standard equations can be found for the most important plasma parameters: temperature, Debye length, plasma frequency, sheath potential and sheath electrical field. As we shall see, the pulsed EUV-induced plasma will be strongly transient and will typically not be in local thermal equilibrium, and the electron energy distribution will not be Maxwellian⁷. This in turn means that many classical plasma assumptions will not or not always apply, and care must be taken with the standard equations for Debye length, plasma sheath et cetera⁸. Still, the resulting quasi-steady-state background

plasma can often be approximated well enough in classical terms, even if the transient peaks may deviate from this. The Debye electrical shielding length is given by:

$$\lambda_D = \sqrt{\frac{\epsilon_0 T_e}{n_e e}} \quad (3.1)$$

with ϵ_0 the permittivity of free space, e the elementary charge, T_e the electron temperature in eV and n_e the electron density.

The characteristic time scale of Debye shielding by electrons is the inverse of the plasma electron frequency $\omega_{pe} = \sqrt{e^2 n_e / \epsilon_0 m_e}$, and the plasma ion frequency is $\omega_{pi} = \sqrt{e^2 n_i / \epsilon_0 m_i}$. Typical values for EUV-induced scanner plasma are $\lambda_D \cong 0.1$ mm, $\omega_{pe} \cong 10^9$ s⁻¹, $\omega_{pi} \cong 10^7$ s⁻¹; giving a plasma response time of ~ 0.1 μ s.

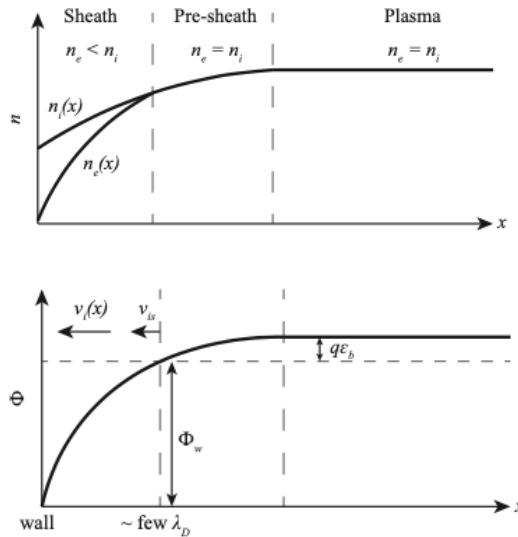


Figure 4: Illustration of the sheath, with the left graph showing the ion and electron densities and the right showing the potential distribution and the resulting ion acceleration. From Van de Ven⁹.

In the bulk of the plasma, the coulomb forces between electrons and ions will prevent charge separation beyond the Debye length, maintaining quasi-neutrality and a negligible electrical field. However, at the plasma-wall interface, the higher mobility of

the electrons leads to a sheath region where the density of electrons is smaller than the density of ions. Thus, a space charge region is formed near the wall, which attracts ions until equilibrium is reached, as illustrated in Figure 4. The resulting potential distribution and electric field in the sheath are determined by the local plasma density and electron temperature. The sheath width for an unbiased wall will be a few Debye lengths, and may be approximated by:

$$L_s \cong 3 \cdot \lambda_D = 3 \cdot \sqrt{\frac{\epsilon_0 T_e}{n_e e}} \quad (3.2)$$

A typical value for the sheath width in scanner is ~ 0.3 mm. The plasma-to-wall potential is closely linked to the electron temperature (combining sheath potential with the pre-sheath Bohm potential).

$$\phi_p = -T_e \ln\left(\frac{m_i}{2\pi m_e}\right)^{1/2} - \frac{1}{2}T_e \quad (3.3)$$

In which the sheath potential and presheath Bohm potential $\Phi_b = \frac{1}{2}T_e$ have been combined⁸. For hydrogen, with H_3^+ as the dominant ion ($m_i = 3$ amu), this leads to a plasma-wall potential $\phi_p \cong -4T_e$. At a typical scanner pressure of ~ 5 Pa no collisions will take place across the narrow sheath and the ion will be accelerated to a kinetic energy at impact of:

$$U_{ion} = q/e \cdot \phi_p \cong 4 \cdot T_e \quad (3.4)$$

For the afterglow plasma with T_e in order of 0.1 eV this gives a first-order estimate of ~ 1 eV for the ion energy. While the plasma potential and ion energy will be low during the afterglow in between pulses, they may reach significant values in the transients during and after the EUV pulse. All ions entering the sheath from the presheath will be swiftly accelerated towards the surface by the electrical sheath field. The ion flux to the

wall $\varphi_{i,w}$ is the product of the local ion density in the presheath $n_{i,ps}$ and the Bohm velocity $v_B = \sqrt{e \cdot T_e / m_i}$:

$$\varphi_{i,w} = n_{i,ps} \cdot v_B = n_{i,ps} \cdot \sqrt{T_e} \cdot \sqrt{e/m_i} \quad (3.5)$$

Within the conductive plasma the electrical field will be effectively zero over distances longer than the Debye length, while the sheath region shows an exponentially decreasing electrical field E_s from a maximum value ϕ_p at the wall to approximately zero at the sheath edge. Near the wall, the value will be approximately:

$$E_s(0) = \frac{d\phi(0)}{dx} \cong -\frac{2}{L_s} \cdot \phi_p \cong -2.5 \cdot \sqrt{\frac{n_e e T_e}{\epsilon_0}} \quad (3.6)$$

While the electrical field will be negligible in the afterglow, during the transient phase it may reach values of $E_s(0) \sim 100$ kV/m, as the transient electron energies may be above $T_e > 10$ eV (and $\lambda_D \cong 0.5$ mm)¹⁰.

For a pulsed plasma, the plasma will cool down and diffuse out during the afterglow, but if the pulse period is shorter than the decay time, the next pulse will be a combination of the residual afterglow plasma and the newly created plasma. These two contributions will have independent electron energy distributions. The combined electron energy distribution may be approximated by a bi-Maxwellian distribution, in which the plasma potential is typically dominated by the high-energy population, with a (downward) correction by the low-energy population equation. Assuming the high-energy population is small relative to the low-energy population, and provided the flux of high-energy electrons is higher than the ion flux¹¹, Godyak derived a modification to the sheath potential equation for a bi-Maxwellian distribution¹²:

$$\phi_p \cong -T_{e2} \left\{ 4.6 - \ln \left(\frac{n_1}{n_2} \cdot \sqrt{T_{e1}/T_{e2}} \right) \right\} \quad (3.7)$$

With T_{e2} and T_{e1} the electron temperature of the high and low energy populations respectively, and n_2 and n_1 the corresponding electron densities; the numerical factor 4.6 is specific for hydrogen¹². As above here the Bohm presheath potential has been added to the sheath potential. The strong effect of the high-energy population on the sheath potential can be understood by the fact that more energetic electrons will be able to escape the potential well formed by the positive space charge of the plasma, while low-energy electrons are effectively trapped nearer to the center of the plasma. Conversely, bulk parameters like Debye length and diffusion constant will be dominated by the overall average electron energy, which is typically dominated by the larger low-energy electron population. In a radiation-induced plasma, a split electron population might also occur because of low-energy secondary electrons being generated from irradiated surfaces, in addition to the electrons generated in the gas ionization process. In case of a pulsed radiation-induced plasma, these effects will combine to three (or more) electron populations, in which case T_{e2} should be the temperature associated with the fraction with the highest energy (again with the condition that the flux of this fraction must be higher than the ion flux), and T_{e1} the combined average of the other fractions. In such cases, analytical expressions cannot be derived anymore and modeling should take over.

3.3.2. *Plasma diagnostics*

The photoelectric currents induced by EUV and EUV-induced fluorescence complicate plasma measurements and diagnostics, rendering Langmuir probes difficult to interpret¹³. For our measurements of temporally resolved ion fluxes and energies, we use a retarding field energy analyzer (RFEA; type Semion Single Sensor from Impedans¹⁴); extensive details are given by Van de Ven¹⁵. Also, the RFEA concept is sensitive to spurious photoelectrons from the internal grids, creating major artefacts during the EUV pulse and directly afterwards. For the present work, the RFEA readout electronics and sampling rate were optimized to minimize the ‘unusable’ time interval to $\sim 0.2 \mu\text{s}$.

Species-resolved ion energy distributions have been measured using an Electrostatic Quadrupole Plasma analyzer (EQP1000, Hiden Analytical), an ion mass spectrometer enabling mass and energy resolved measurements; details are again given by Van de Ven⁹. The EQP does not provide time-resolution to better than 3 μs , but will capture the transient first $\sim 1 \mu\text{s}$ as part of the overall ion energy distribution.

3.3.3. Plasma modeling: hybrid PIC

The pulsed photo-ionization origin of the plasma leads to important differences from textbook plasma, such as strong transients and a non-Maxwellian energy distribution function during and after the EUV pulse (of $<100 \text{ ns}$). This precludes the use of fluid-based models, which rely on continuity equations for moments of the distribution functions for electron density, velocities and energies. Instead, a kinetic model must be used that can solve the full equations for the electron distribution functions without any a priori assumptions about their shapes, such as (Monte-Carlo) Particle-in-Cell (PIC). The essence of the PIC model used consists of a Poisson equation solver, followed by updating the charged particles positions and velocities based on the obtained field distribution and individual particle velocities¹⁶. This also allows accurate tracking of the ions, which have mean free path lengths in order of mm's in low-pressure H_2 , and thus will experience only a few collisions with neutral gas molecules before hitting a surface. This PIC model has been tailored for simulation of EUV-induced plasma¹⁷, and the resulting model has been validated for EUV at a relevant pressure of 5 Pa in an off-line test setup using an Electrostatic Quadrupole Plasma (EQP) Analyzer¹⁸, as shown in Figure 5.

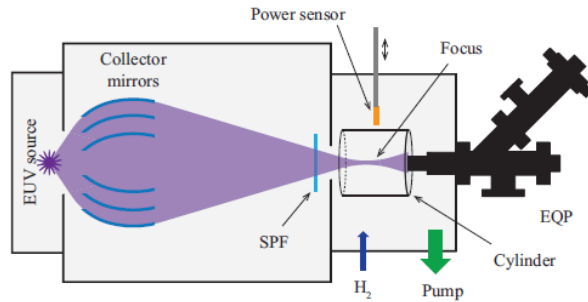
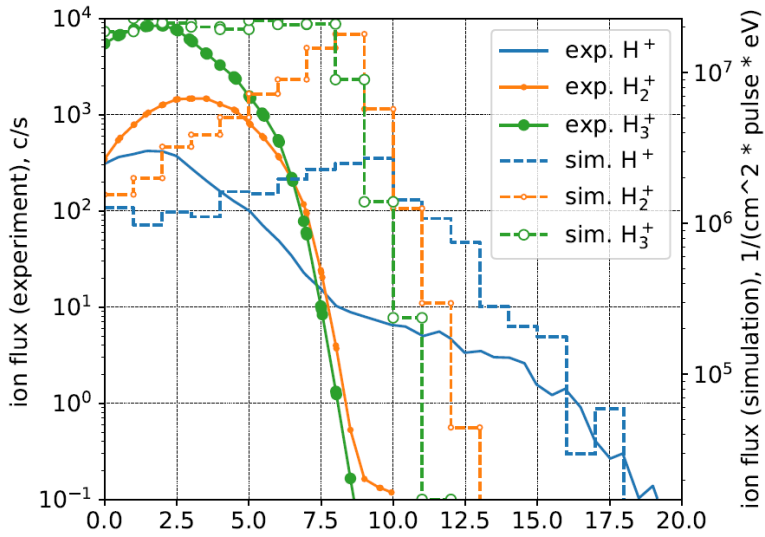


Figure 5: EUV-induced ion energy density functions, as simulated by PIC model (solid lines) and measured by EQP (dashed lines) in off-line EUV set-up (bottom)⁹.

A drawback of the kinetic PIC-approach is the high computational cost for larger volumes and/or longer timescales. Typical decay times of the scanner plasma at pressures of 1-10 Pa will be longer than the pulse interval of 20 μ s and plasma will build up over several pulses. For these conditions direct multi-pulse PIC simulations are still possible, but the run time of such simulations becomes prohibitive, since this is dominated by the simulation of the decay of the cold plasma and an explicit PIC model needs to run with mesh cell size of few Debye radii and time step Δt smaller than the inverse plasma electron frequency, or $\Delta t < 1/\omega_{pe} = 0.5$ ns for a 250 W EUV Source (it should be noted that for the decay of the cold EUV induced plasma those conditions

are typically even more restrictive than for the hot phase during EUV pulse, since the electron temperature of the plasma decreases faster than the ion and electron density). To resolve this a dedicated hybrid 3D-PIC model has been developed, which uses a rigorous kinetic model for the initial non-Maxwellian phase during and directly after the EUV-pulse, up till $\sim 2 \mu\text{s}$; and a fast fluid-like drift-diffusion model for the electron density and energies in the subsequent diffusion phase, when the deviation from a Maxwellian energy distribution becomes small enough to ignore. The transition criterium was taken to be when the electron high energy tail dropped below 8 eV, in which case all electronic energy loss processes except vibrational and rotational processes may be neglected and all remaining reaction rates are accurately approximated by a Maxwellian distribution (of $T_e < 1 \text{ eV}$). The ions are still modeled kinetically, which is needed because of the lack of collisions. Focus of the code development was the (unstructured) meshing complexities of the relevant 3D geometries, with many slits, electrically floating surfaces and dielectric surfaces. Such a hybrid model allows to significantly accelerate multi-pulse simulations¹⁹, since the evolution of the cold afterglow plasma between EUV pulses now needs to be described only with resolution of ion time scales (in order of $\tau_i = 30 \text{ ns}$ for 5 Pa and 250 W EUV Source). Figure 6 shows the switching moment from full PIC to Hybrid mode as well as the gain in model performance. The overall performance gain in temporal hybrid mode is $\sim 4x$ over full pulse cycle of $20 \mu\text{s}$, with further runtime reduction potential identified in coarser meshing. The general validity of such an approach for hydrogen pressures around 5 Pa has been demonstrated by Van de Ven⁹, as shown in Figure 6.

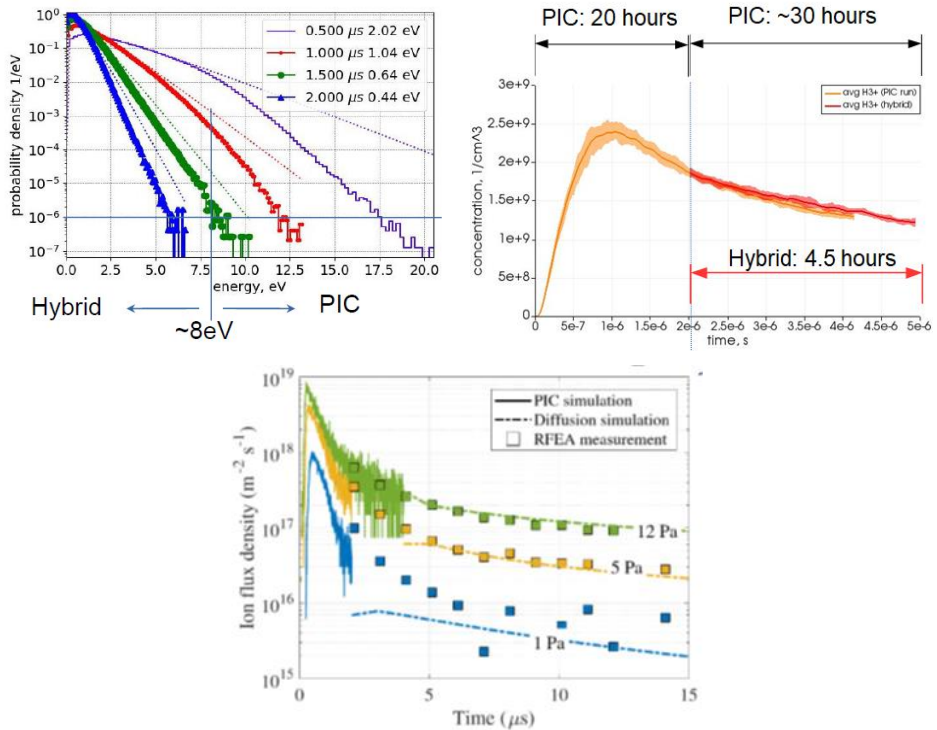


Figure 6: Left: 3D PIC-Hybrid switch condition. Right: reduction of simulation time by hybrid model for first 5 μs . Bottom: validation of hybrid model approach by RFEA⁹.

This approach also enables modeling of multiple pulses. As the hybrid model reaches the time of the next EUV pulse, the drift-diffusion model is converted back to be starting point for next iteration of numerical particle-in-cell, maintaining the obtained spatial and average electron energy distributions. Subsequently, the next EUV pulse is added to this distribution and the next model iteration starts. During this next EUV pulse the energetic photo-electrons and associated ions will be added to the existing colder populations of electrons and ions. Pulse by pulse, the electron density will build up until equilibrium is reached with diffusion losses to the walls and volume recombination, which will depend on the confinement geometry; resulting in a quasi-steady-state background with transient peaks in electron temperature, ion density and ion flux for each EUV pulse. For an open plasma geometry, this equilibrium might take hundreds of pulses to reach, while for a confined geometry such as the scanner RME, this might be reached within a few pulses, as shown in Figure 7.

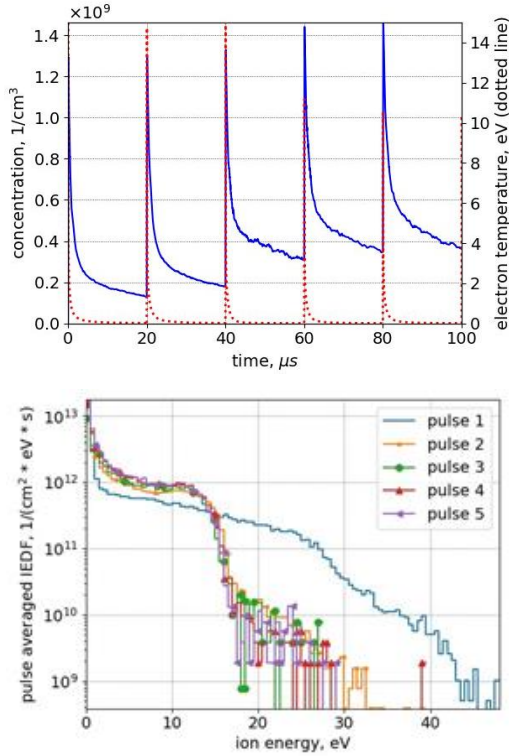


Figure 7: Top: example of hybrid PIC modeling of evolution of electron density and electron temperature in a pulsed plasma, in the center of the EUV beam below the reticle. Build-up of stable background with a few pulses can be clearly observed. Bottom: evolution of pulse-averaged ion energy distribution function (IEDF) at the edge of the beam.

3.3.4. Plasma generation

The 92 eV EUV photons will lead to photo-ionization of the hydrogen background gas. The total cross section for photo-ionization of hydrogen for 92 eV photons is $\sigma_{h\nu} = 6.2 \cdot 10^{-24}$ m^2 and gas density at room temperature and a pressure of 5 Pa is $n_{H_2} = 1.21 \cdot 10^{21}$ m^{-3} , resulting in an attenuation length of $l = (n_{H_2} \sigma_{h\nu})^{-1} = 0.13$ km^{20} . This is much larger than the plasma dimensions within the scanner, so the initial electron and ion production per unit volume $n_{h\nu}$ from photon-ionization can be estimated using a linear approximation of the Beer-Lambert law of absorption:

$$\frac{dn_{hv}}{dt} = \frac{P_{euV}}{h\nu} \cdot n_{H_2} \cdot \sigma_{hv} \quad (3.8)$$

With P_{euV} the EUV power (and $\varphi_{hv} = P_{euV}/h\nu$ the average photon flux density). Assuming a 250 W EUV source, and a local EUV power of ~50 W at the regions of interest in the scanner, at a pressure of around 5 Pa the initial plasma production will be in order of $10^{19} \text{ m}^{-3}\text{s}^{-1}$. Taking lateral beam dimensions of $\sim 11 \times 1 \text{ cm}^2$, the average ion flux will be in order of $10^{17} \text{ m}^{-2}\text{s}^{-1}$. At 50 kHz Source frequency, the integrated initial ion density over a single pulse will be in order of $10^{15} \text{ m}^{-3}\text{s}^{-1}$, and the plasma ionization degree will be in order of $10^{-4} \%$.

The dominant photo-ionization mechanisms for molecular hydrogen are non-dissociative (~80% branching ratio) and dissociative single ionization (~15% branching ratio)^{21,22}:



The ionization energy of hydrogen is 15.4 eV^{23} , and for non-dissociative photoionization the large excess energy of 76 eV is divided over the resulting electron and ion. Momentum conservation and the large ratio in mass between ion and electron dictate that the excess energy for non-dissociative ionization is carried for >99.9% by the photoelectron, while the ions remain within roughly twice room temperature. For dissociative ionizations, the energy is more evenly distributed with the photoelectron carrying 60-70 eV and the ions and radicals each carrying in order of 10 eV^{24} . In this process, the radical atom may end up in an excited electronic state, increasing its total

energy further. The resulting plasma will thus contain slow H_2^+ and fast H^+ ions, and fast radicals.

The peak plasma and radical densities will increase further by secondary electron-impact ionizations by the energetic photoelectrons:



The energetic photoelectrons will quickly lose energy by collisions with the neutral hydrogen molecules and resulting secondary ionizations, dissociations and excitations, or will be lost to the walls. As shown in Figure 8 the dominant electron-impact process is ionization to H_2^+ , with a branching ratio of ~60% for 76 eV electrons, and on average ~0.6 additional electrons will be formed per collision. The ionization energy loss is 15.4 eV, and the remaining energy is divided over the electrons, or an (average) electron energy of ~30 eV. This may still be sufficient for an additional ionization and dissociation, after which the electron energy will have dropped below 10 eV and further collisions will only result in excitations of electronic and ro-vibrational states. Combining these ionizing and dissociating steps results in a potential formation of ~2.5 ions per absorbed photon, and up to 8 hydrogen radicals. For a confined plasma, a finite fraction of the electrons will be lost to the wall and the number of ions and radicals generated will be lower.

The inelastic mean free path λ_e and electron-neutral collision frequency f_{en} of the electrons are (neglecting the inefficient energy transfer by momentum transfer for electron energies above 1 eV)²⁵:

$$\lambda_e(\varepsilon) = \frac{1}{\sigma_{en}(\varepsilon) \cdot n_{H_2}} \quad (3.14)$$

$$f_{en}(\varepsilon) = \frac{v_e(\varepsilon)}{\lambda_e(\varepsilon)} = \sqrt{2\varepsilon/m_e} \cdot \sigma_{en}(\varepsilon) \cdot n_{H_2} \quad (3.15)$$

With ε the electron energy, v_e the electron velocity and σ_{en} the energy-dependent electron-neutral cross section for inelastic collisions. The cumulative inelastic cross section for electron energies of >25 eV is $\sigma_{en} = 1.7 \cdot 10^{-20} \text{ m}^2$ at 5 Pa H_2 ,²⁵ resulting in an initial mean free path of $\lambda_e = 4.9$ cm and collision frequency f_{en} of ~ 100 MHz. For an EUV beam width of ~ 1 cm or smaller, this means the majority of the fast electrons escape the beam volume and secondary ionizations and radical formation mainly take place outside the original beam volume. In addition, the high initial electron energy leads to a rapid initial expansion of the plasma to fill the surrounding ~ 1 cm around the beam in the first ~ 0.1 μs , after which the expansion rate drops as the electrons cool down.

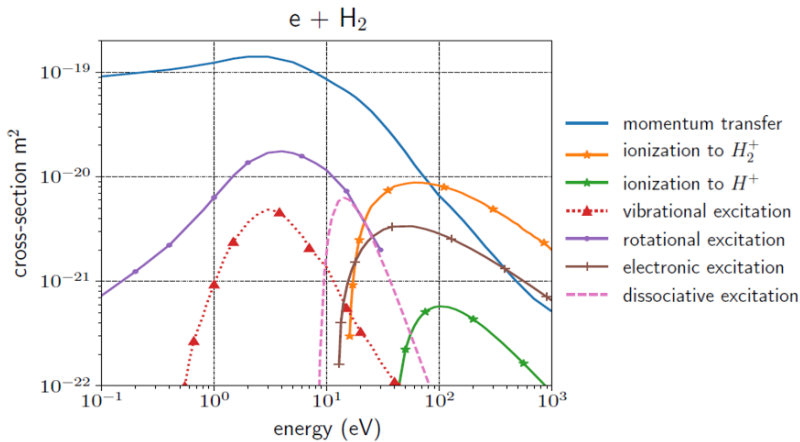


Figure 8: Cross sections of possible electron-neutral collisions. Based on data from Tawara²⁶ and Yoon²⁵.

Ion-molecule collisions of the cold H_2^+ ions with H_2 result in H_3^+ by the highly efficient proton hop mechanism, resulting in H_3^+ as the dominant ion after ~ 0.5 μs , as also observed in the interstellar hydrogen plasma²⁷. The ~ 1.7 eV energy released in this exothermic process will be distributed between internal excitation of the molecular ion and kinetic energy of the H radical and the molecular ion, which again is a source of relatively hot radicals.



The interactions of H^+ with H_2 are dominated by momentum transfer, although asymmetric charge transfer to H_2^+ is also possible, e.g. when the H^+ ions are accelerated in the sheath to >3 eV ($\sigma = \sim 10^{-20} \text{ m}^2$)²⁸. The resulting ion distribution after the first microsecond will be roughly 90% H_3^+ and 10% H^+ .

3.3.5. Photoelectric effect

Mirrors and construction materials emit electrons when irradiated by photons with an energy $h\nu$ above the work function of the material²⁹. The quantum efficiency is governed by the penetration depth of the photons (which increases with photon energy), and hence in general decreases for higher photon energy³⁰. In terms of power (#e/W), this is further exacerbated by the lower number of photons per joule for higher photon energy. As the penetration depth of EUV photons is significantly larger than the mean free path length for electron-electron collisions in the solid, the primary electrons undergo many scattering events before reaching the surface, resulting in predominantly low energies for any electrons being emitted⁷.

For metals the electron quantum yield is typically in order of a few percent for EUV photons. For the ruthenium (Ru) mirror caplayer the secondary electron yield (SEY) has been measured to be 2%, with an electron energy spectrum dominated by low-energy electrons³¹; this electron energy distribution may reasonably be approximated by a Maxwellian distribution with $T_e \approx 3$ eV³².

For the example of the RME, conservatively estimating the reticle SEY to be 2% and taking a photon flux density of $10^{21} \text{ s}^{-1} \cdot \text{m}^{-2}$, the secondary electron current density may be estimated to be $\sim 2 \cdot 10^{19} \text{ s}^{-1} \cdot \text{m}^{-2}$ (or $\sim 3 \text{ A/m}^2$), which is larger than the gas ionization contribution. In practice, this current will be self-limiting by formation of an instantaneous negative space charge layer next to the surface that will trap the low-energy electrons and return these to the surface. In combination with simultaneous gas ionization by EUV, this negative space layer will be partially compensated by the overlap with the positive space layer of the ionized gas some electrons, allowing more

low-energy secondary electrons to escape from the surface and more high-energy photoelectrons to escape to the surface. The electron flux from the surface during the EUV pulse suppresses formation of a classical sheath during the pulse and the plasma-to-surface potential will be reduced in this phase. At the end of EUV pulse, the photoelectric electron flux stops and a classical sheath will develop, but with a delay and reduced maximum potential³³. This will significantly reduce the transient electron energies and resulting peak ion energies.

The hydrogen plasma will be significantly modified by the relatively cold electrons from the photoelectric effect in the vicinity of the reticle or a mirror or other EUV-irradiated surface. The secondary electrons will form a significant population with respect to the energetic electron from gas ionization, and the resulting plasma must be treated as a bi-Maxwellian distribution. This will significantly reduce the transient electron energies and resulting plasma characteristics.

As the work function of most metals and construction materials is in order of 5 eV, all out-of-band radiation with wavelengths up to 200 nm should be considered for total photoelectric effect. During the EUV pulse, the out-of-band contribution of ~1% may be ignored as a minor perturbation, but these wavelengths may persist in the cooling-down phase after the EUV pulse as a UV afterglow, which may continue to release low-energy photoelectrons for several tenths of microseconds after the EUV has died out (see section 2.6). These UV photons will not ionize, but will generate additional low-energy secondary photo-electrons from irradiated surfaces, thereby charging the plasma volume negatively for a longer time.

Even for a minor UV afterglow of ~1%, this can have a significant effect on the plasma, since both the quantum efficiency and the number of photons per Watt will be roughly an order of magnitude higher for UV than for EUV³⁰. Thus, the number of photoelectrons generated in the afterglow may be in same order of magnitude as the EUV-induced plasma electrons and development of a classical sheath will be delayed until the afterglow dies out.

3.3.6. Wall losses, electron exchange and electron cooling

For a closely confined plasma, loss of energetic electrons to the walls may dominate over inelastic or ionizing collisions, with a fraction f_w of the energetic photoelectrons being lost to the wall without further ionizing collisions events:

$$f_w = e^{-\frac{\Lambda_w}{\lambda_e}} \quad (3.17)$$

With Λ_w the typical length of the confinement, and λ_e the mean free path of the electrons. For a confined EUV-induced plasma with $\Lambda_w=1.5$ cm and $\lambda_e=4.9$ cm, a significant fraction of $f_w \approx 74\%$ of the absorbed EUV energy may be lost to the walls and significantly less secondary ionizations take place, resulting in a $\sim 2x$ lower plasma density as compared to an open plasma⁹.

Previous investigations assumed this would be counteracted by the almost instantaneous formation of a potential well which subsequently repels and confines the majority of fast electrons^{34,9}. However, for the high-energy photoelectrons from EUV ionization, secondary electron emission (SEE) from the surface becomes a significant effect, which so far seems to have been overlooked. For typical construction materials such as stainless steel and aluminum, the yield of (low-energy) secondary electrons has been measured to be above unity for 76 eV³⁵. In other words, the plasma-facing surfaces will tend to charge positive rather than negative, so no potential well is formed near walls and no electron trapping or ion acceleration occurs in this phase.

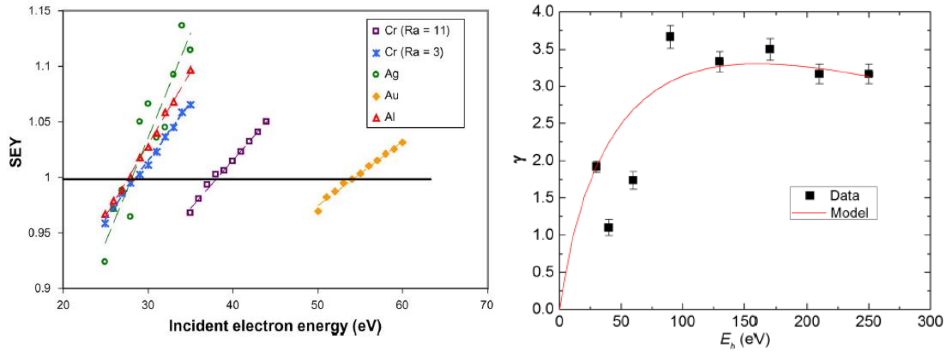


Figure 9: Examples of secondary electron yield SEY as function of incident electron energy. Left for Cr, Al, Ag, Au; from Balcon³⁵. Right for stainless steel; from Wang³⁶.

This SEY > 1 for 76 eV is not generally predicted by the universal curve of Lin³⁷, which was set up with a focus on higher energy electrons and for ideal metal surface states. For energies well below the maximum yield energy (typically 0.4-0.6 keV for construction materials), it is advisable to use an empirical linearization based on literature data and/or measurements, and to blend that smoothly into the universal curve above ~100 eV. This is the approach that was incorporated into our 3D-PIC model.

The secondary electrons will have lower energies, and may be approximated by a Maxwellian distribution with $T_e \approx 3$ eV, similar as for photo-generated secondary electrons. The resulting overall electron distribution will be bi-Maxwellian with a split in low-energy and high-energy fractions and an average energy well below 10 eV. As the remaining plasma electrons cool down by collisions to below 30 eV after ~25 ns (see Figure 10), the SEY will drop below unity, and the wall will start to charge negatively. A classical plasma-wall sheath will subsequently develop, albeit at a later time and with significantly lower sheath potential than if no secondary electron emission is taken into consideration. The details of this transition depend strongly on wall material and surface finishing, as illustrated in Figure 9 for the example of chrome (Cr), and no generic analytical solution can be given.

Besides electron exchange at the walls, the energetic photoelectrons lose their energy fast in ionizing and dissociating collisions with the neutral molecules. The initial electron energy distributions from photo-ionization is not in thermal equilibrium and does not follow a Maxwellian distribution; this is significant for the resulting plasma properties until the electrons cool down to below the ionization threshold, after which the plasma may be satisfactorily approximated by a Maxwellian distribution. As the electron energy drops below 10 eV, further cooling will proceed at a progressively lower rate by ro-vibrational excitations and finally momentum transfers. Thermalization by electron-electron collisions becomes relevant only when the plasma has cooled down to below 1 eV⁹.

The electron energy loss rate will change step-wise as different collision types with different energy losses become less or more important; also, the gradual decrease in collision frequency with decreasing energy will result in a gradual reduction of cooling rate, as illustrated in Figure 10. The initial electron energy of 75 eV will drop to below 10 eV within 0.1 μ s, and to below 0.5 eV within 5 μ s. Further cooling and thermalization by elastic collisions will be slow and may take >100 μ s. The energy decrease over time may be approximated by piece-wise exponential functions with increasing time constants for the different energy ranges.

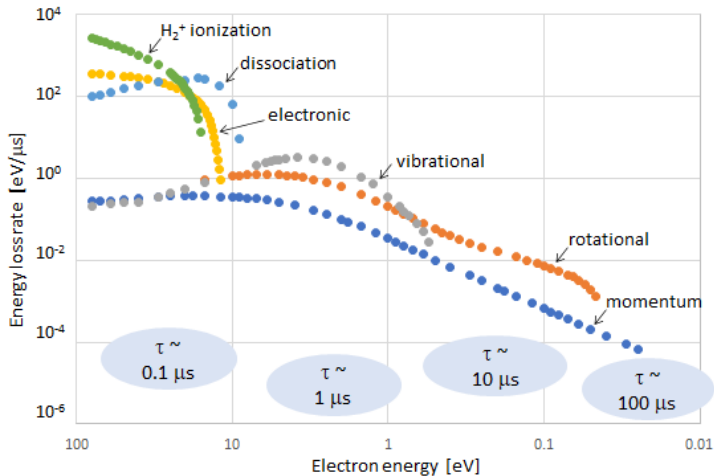


Figure 10: Electron energy loss rates by inelastic collisions; based on data from Yoon²⁵ and Tawara²⁶.

It should be noted that as the density of metastable vibrationally excited H₂ molecules builds up, an equilibrium might form where electrons also experience super-elastic collisions and a long-lasting electron fraction with 0.5 eV energy may be sustained (corresponding to the vibrational energy quantum of 0.516 eV³⁸)³⁹.

3.3.7. Diffusion, flux and energy

In the plasma bulk, where there is no electrical field, the velocity of the electrons depends on their energy, $v_e = \sqrt{2\varepsilon/m_e}$, and may be as high as $\sim 10^6$ m/s. As the electron energy drops to 1 eV, the velocity becomes in order of 10^5 m/s. Though very high, such an electron speed is finite with respect to the fast transients and for a typical distance of 1 cm may result in finite delays in order of 0.1 μ s.

At the edge of the plasma quasi-neutrality is no longer valid and the electrons will be decelerated by the coulomb interaction with the heavier and slower ions; this mutual interaction results in ambipolar diffusion, slowing down the electrons and speeding up the ions. During the EUV pulse, for a confined plasma the entire volume will be filled with ions via primary and secondary ionizations, after which the ions will diffuse out towards the walls. The ambipolar diffusion constant D_a scales with pressure and electron temperature⁴⁰:

$$D_a = \mu_i^0 \cdot \frac{p_0}{p_{H_2}} \cdot (T_e + T_i) \cong \mu_i^0 \cdot \frac{p_0}{p_{H_2}} \cdot T_e \quad (3.18)$$

With $\mu_i^0 = 1.1 \cdot 10^{-3}$ m²/Vs the ion mobility of H₃⁺ in hydrogen at atmospheric pressure ($p_0 = 10^5$ Pa)⁴¹, p_{H_2} the hydrogen pressure in Pa and $T_{e,i}$ the electron and ion energies in eV. The continuum assumption underlying equation 3.18 is only a rough approximation for a bi-Maxwellian distribution, and more rigorous numerical PIC-models are needed for the transient phase during and after the EUV pulse.

In case of a bi-Maxwellian split electron energy distribution, the effective electron temperature may be a function of distance to the wall, which in turn may give rise to

discontinuities in the diffusion-driven ion flux for different time-scales, with the short term being driven by the high-energy fraction (T_{e2}) and the long term by the average electron temperature (T_{e1}).

As the plasma ions diffuse outwards reach the surrounding walls, they will recombine with the electrons already present at the wall surfaces, and the lifetime of the plasma pulse is thus limited by ambipolar diffusion. In view of the low ionization degree, volume recombination will be a minor effect; whether it can be ignored completely will depend mainly on pressure and wall distance⁴². The ambipolar diffusion time constant is:

$$\tau_a = \frac{\Lambda_w^2}{D_a} \cong \frac{\Lambda_w^2 \cdot p_{H2}}{\mu_i^0 \cdot p_0} \cdot \frac{1}{T_e} \quad (3.19)$$

with Λ_w the typical length of the plasma confinement, which for a rectangular geometry may be found from:

$$1/\Lambda_w^2 = 1/L_x^2 + 1/L_y^2 + 1/L_z^2 \quad (3.20)$$

The RME may be approximated by a rectangular box with $L_x=12$ cm, $L_y=2$ cm (the beam itself is $\sim 11 \times 1$ cm², as described above; the z-dimension of the box is arbitrary and may be taken equal to the smallest dimension, or $L_z=2$ cm). This results in a typical length of $\Lambda_w \approx 1.5$ cm for the RME. Taking $\Lambda_w=1.5$ cm, and an electron temperature of 0.1 eV, a typical value for the long-term diffusion time constant will be $\tau_a \cong 100$ μ s. It should be noted that diffusion losses will be slower for higher pressure, whereas collisional losses will be faster for higher pressure.

When the sheath has formed at the plasma-facing surface, all ions entering the sheath from the presheath will be accelerated towards the surface. The ion flux to the wall $\phi_{i,w}$ is the product of the ion density in the presheath $n_{i,ps}$ and the Bohm velocity. The ion density in the presheath is determined by the ambipolar flow velocity from the EUV beam towards the surface. Diffusional transport takes a relatively long time from beam

to wall so will not respond to the instantaneous value of the electron temperature. The Bohm velocity on the other hand will be proportional to the instantaneous value of $\sqrt{T_{e2}}$ and this will drive the dynamics of the ion flux to peak with the transient peak and rapid fall in T_{e2} during and directly after the EUV pulse.

As outlined above, initial sheath formation at the plasma-facing surfaces is frustrated by secondary electron emission. In the initial phase with $SEY > 1$, a space-charge-limited negative sheath layer (SCL)⁴³, or even an inverse sheath⁴⁴, will form near the walls. As the photoelectrons cool down to below ~ 30 eV the SEY will drop below unity. As sketched in Figure 11, the space-charge-limited sheath will then transition to a classical plasma-wall sheath, albeit with reduced sheath potential. As the classical sheath is formed the ion flux will start to rise on a timescale of a fraction of a microsecond, limited by ion inertia and the finite force of the electrical sheath field. The delay in formation of a classical sheath results in a dead period in ion flux after the EUV pulse; also by the time the sheath is formed the electrons will have cooled down to energies below 10 eV, and the effective electron temperature will be in order of ~ 1 eV. The SCL period may be extended by the UV afterglow of the EUV pulse, which for an LPP Source may continue to release low-energy photoelectrons for up to ~ 0.3 μ s after the EUV has died out, maintaining a negative space-charge layer during that time.

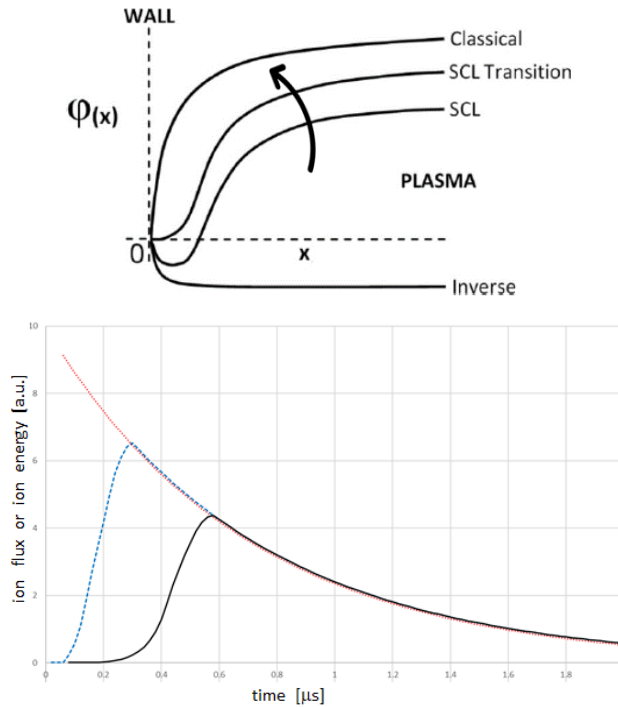


Figure 11: Top: sheath evolution over time, including secondary electron emission from fast electrons and UV afterglow; adapted from Campanell⁴⁴. Bottom: artist impression of the ion flux/energy transient by the intersection of sheath formation and electron cooling curve (red line), without (blue line) and with delay from SCL (black line).

As the classical sheath is formed over a time span of $\sim 0.1\text{-}0.2 \mu\text{s}$, the ion energy will rise with the increasing plasma-wall potential, as well as the ion flux. However, simultaneously the overall electron energies are decreasing fast, and correspondingly both sheath potential and Bohm velocity. The combined effect is a sharp peak followed by an exponential decrease in both ion flux and ion energy, following the decrease in fast electron energy, as sketched in Figure 11.

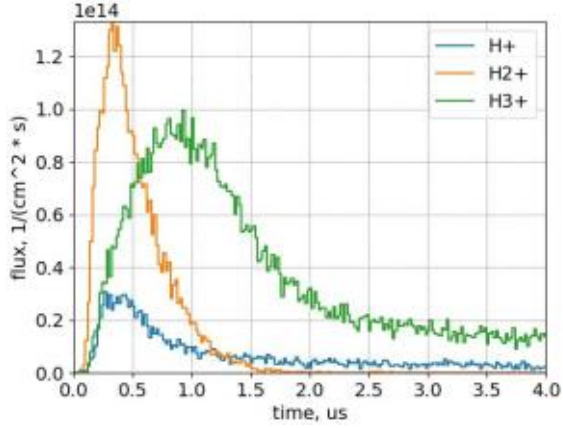
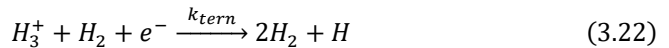


Figure 12: Modeled transient ion dynamics at the edge of the EUV beam (beam width 1cm).

These phases of dead time, peak and decrease also show clearly in the PIC model results for both ion energy and ion flux, as shown in Figure 12. For hydrogen, the transient period in the first microsecond is convoluted with the overlapping transition from H_2^+ to H_3^+ , which leads to the later peak in H_3^+ and results in H_2^+ as the most abundant energetic species, even if H_3^+ is the most abundant ion overall. Detailed interpretation of hydrogen ion spectra requires an approach that is selective to ion species as well as time-resolved.

3.3.8. Volume recombination

Although earlier work reported that volume recombination could be ignored at pressures of 10 Pa and below, internal measurements have shown this is not always the case. For volume recombination, both binary and ternary recombination should be considered, with reaction rates of $k_{bin} = \sim 2 \cdot 10^{-8} \text{ cm}^3\text{s}^{-1}$ (for $\sim 0.1 \text{ eV}$ electrons) and $k_{tern} = 8.7 \cdot 10^{-23} \text{ cm}^6\text{s}^{-1}$ respectively^{45,46}.



Close to room temperature, ternary recombination is expected to dominate over the binary dissociative recombination for hydrogen pressures above ~ 2 Pa ($n_{H_2} \cong 5 \cdot 10^{20}$ m⁻³, and $n_{H_2} \cdot k_{tern} > k_{bin}$). Ion generation scales with pressure (and EUV intensity), and diffusion transport scales with pressure (and inversely with distance to the wall), while equation 3.22 shows that ternary recombination scales with pressure to the third power (and with distance). For very low pressures the ion flux will increase with pressure at any given distance. For higher pressures, the third-power pressure scaling of recombination will result in a balance of ion source and loss terms, and the ion flux will reach a maximum; beyond that the ion flux will decrease for a further pressure increase. Recombination and diffusion also depend on distance, shifting the location of this maximum to lower pressures further away from the beam. For a given distance, increasing EUV power will shift the maximum to a somewhat lower pressure.

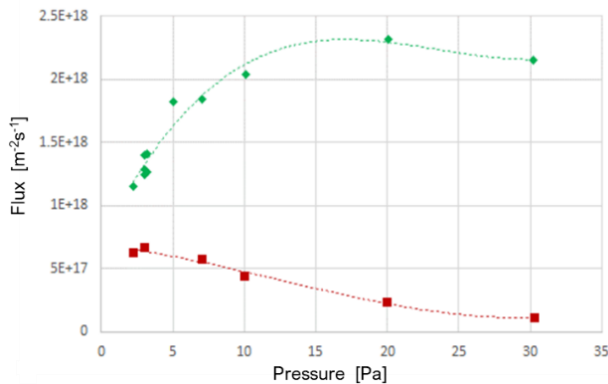


Figure 13: Ion flux as function of pressure, measured at the edge of the EUV beam (diamonds) and at a distance of 4 cm (squares) from the beam edge⁴⁷.

For 5 Pa, and confinement with typical length $\Lambda_w=1.5$ cm, Figure 13 shows recombination is minor and ion flux to the walls will scale more or less linearly with pressure and with power. For a less confined, more open plasma this transition point will shift to a lower pressure, in which case recombination may become significant also for 5 Pa.

3.3.9. Pulsed mode operation

The LPP EUV Source operates at a cycle time of 20 μs , with an EUV pulse length of <100 ns. As the plasma does not extinguish completely within 20 μs , there will be pulse-by-pulse build-up towards a quasi-steady-state plasma, with repeating transient peaks every 20 μs . During scanner exposures the EUV pulse train will typically run for ~5000 pulses and will then be interrupted for several milliseconds, during which time the plasma will extinguish completely. This mode of operation means that the vast majority of pulses will be fired on top of a steady-state background plasma, and start-up and decay effects may effectively be ignored.

Extending the single-pulse bi-Maxwellian treatment above, there will initially be three electron populations in the transient phase after the pulse: a hot fraction driven by gas ionization, a cooler fraction driven by secondary electron emission from the walls and a cold fraction from the background plasma. In this case, the gas ionization fraction, with the highest energy, will define T_{e2} initially, and the collisional cooling of these electrons will drive the plasma potential transient after the pulse. However, as outlined above the negative space charge from the secondary electrons from the wall might prevent a classical sheath build-up in the first ~0.2-0.3 μs so this might not translate one on one into ion energies. After ~2 μs the populations will effectively merge, and the afterglow and global diffusion will be driven by the average electron temperature.

For an open plasma, ambipolar diffusion will be much slower than the pulse cycle and plasma will build up until volume recombination balances plasma generation at high enough electron and ion densities; the pulses can then be treated as perturbations and the plasma can be reasonably approximated by a continuous ionization source of same average power instead of a pulsed plasma, enabling continuum theories and corresponding fluid models⁴⁸. For a confined plasma, or very close to the mirror or reticle, diffusion losses to the surface will limit the build-up and the plasma properties may to a large degree be determined by the repeating transient peaks; this requires explicit PIC modeling and nonlocal kinetics⁴⁹.

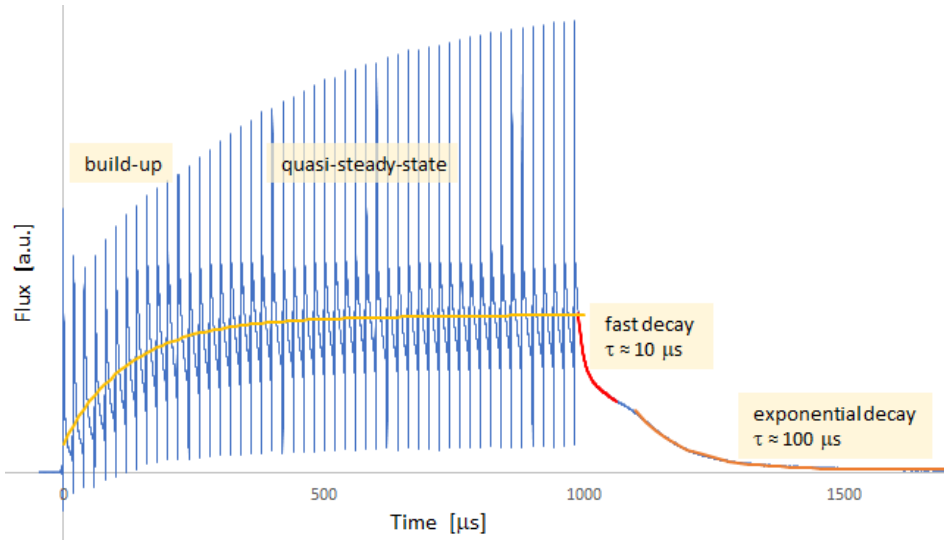


Figure 14: Build-up, steady-state and decay of pulsed EUV-induced plasma, as measured by RFEA in LPP testrig at 5 Pa⁴⁷.

For a relatively open plasma, Figure 14 shows the measured buildup and decay of the ion flux, and the pulses on top of an evolving background. Both the global build-up and long-term decay can be fitted by an exponential diffusion with time constant in order of $\tau_a \cong 100 \mu\text{s}$, which corresponds to a background electron temperature close to room temperature. As may be observed, the decay for the first $\sim 50 \mu\text{s}$ after the last EUV pulse, and also in between the EUV pulses, is significantly faster with a time constant of $\sim 10 \mu\text{s}$, corresponding to a significantly higher apparent $T_e \cong 0.5 \text{ eV}$. This may be qualitatively explained by a bi-Maxwellian split electron population where part of the electrons receive energy from super-elastic collisions with vibrationally excited hydrogen molecules, with a vibrational energy quantum of 0.516 eV^9 ; similar behavior has been observed also in other pulsed hydrogen⁵⁰ and argon⁵¹ plasma's. The flux decay time-constant in this phase is driven by the cooling time-constant of the high-energy electron fraction (T_{e2}), which is driven by collisions and thus scales with pressure ($\tau_{a,ini} \sim 1/p$; while the long-term diffusion-driven τ_a decay time-constant scales inversely with pressure $\tau_a \sim p$).

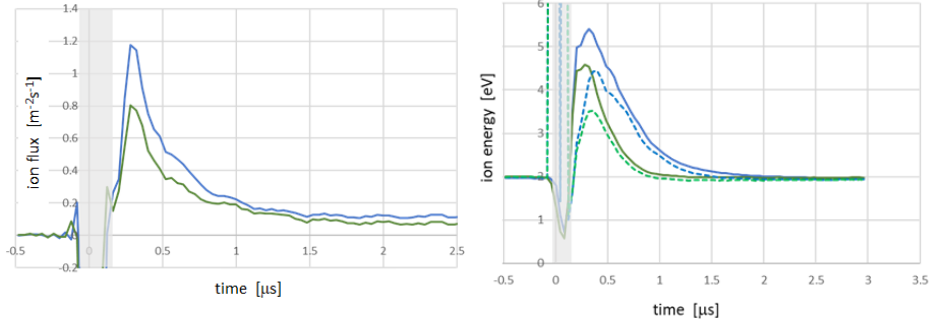


Figure 15: RFEA measurement of transient ion energy and flux in quasi-steady-state; RFEA blind time of $0.2 \mu\text{s}$ is marked in gray. Top: ion flux peak measured at 4 cm from the beam edge. Bottom: ion energy peak for pressure of 5 (blue) and 10 Pa (green), at 0 cm (solid lines) and at 4 cm (dashed lines) from the EUV beam edge.

The peaks in ion flux and energy occur when the sheath formation intersects with the photoelectron cooling curve. This intersection depends on wall geometry, pressure and background plasma. The exponential energy decay is driven by collisional cooling, with f_{en} scaling linearly with pressure, and does not depend on distance. This faster cooling results in a lower ion energy by the time the sheath is formed. However, this is (partly) balanced by faster sheath formation for higher pressure, as for higher pressure the conductivity of the plasma increases and the initial negative space charge layer from the SEE term is dissipated faster. The net result is that peak energy drops with increasing pressure, as shown in Figure 15.

In between the pulses the ion energy drops fast to a metastable platform of roughly 2 eV, which corresponds to an electron temperature $T_e \cong 0.5 \text{ eV}$, using equation 3.4. This is significantly higher than the expected $T_e < 0.1 \text{ eV}$ ⁹, but is consistent with the measured decay time constant, as well as with earlier off-line experiments³⁹. As discussed above, this may be explained by super-elastic collisions with vibrationally excited hydrogen molecules.

Figure 15 also shows that at 4 cm distance from the beam, the ion peak is delayed a further 80 ns and the peak energy is accordingly lower, intersecting with the cooling curve at later time; this may be explained by the finite speed of the electrons traveling between the EUV beam and the surface/sensor ($v_e \cong 6 \cdot 10^5 \text{ m/s}$ around 1 eV),

resulting in delayed formation of plasma potential and sheath at larger distances. At 4 cm distance from the beam, the ion flux is observed to decrease for higher pressure, driven by faster cooling and resulting slower diffusion to this distance, consistent with Figure 13. Perhaps surprisingly, a higher pressure may thus result in a reduced ion load to plasma-facing surfaces, both in terms of flux and peak energy (for a wall sufficiently far from the EUV beam). This could be considered an artefact of a relatively open plasma; for a more closely confined plasma with $\Lambda_w=1.5$ cm, ion flux will increase for higher pressure until >10 Pa.

As diffusion is relatively slow, the fast exponential decay of the flux is mainly driven by the evolution of the Bohm velocity. However, the sheath width may change fast, in which case less or more ions are captured by the sheath; thus, the flux decay curve over time might be more complex and might show dips (when sheath decreases) or bumps (when sheath increases). The coinciding peaks in ion energy and flux result in an enhanced fraction of high-energy ions, which may be significant for the plasma-wall interactions, as these typically exhibit non-linear response to ion energy, such as sharp energy thresholds for e.g. sputtering (when exceeding the sputtering threshold) or ion-enhanced chemical reactions (when exceeding the surface binding energy).

During the first pulses of the burst the background plasma contribution grows, again reducing the relative contribution from the SEE terms and thus allowing the sheath to form faster; this will result in increasing ion energy peak, as shown in Figure 16. The balance between the different electron contributions from gas ionization and SEE terms is also influenced by the source frequency, with a longer pulse interval resulting in a lower background plasma at the next pulse. This increases the relative contribution from the SEE terms and delays the sheath formation, resulting in a lower ion energy peak for longer pulse interval, as shown in Figure 16. Conversely, increasing the source frequency will reduce the pulse interval and will this result in higher ion peak ion energies.

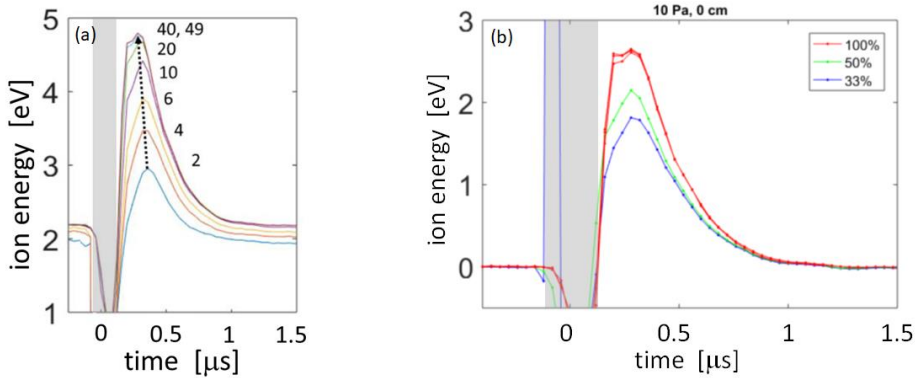


Figure 16: RFEA measurement of ion energy, at 10 Pa, next to the EUV beam. Left: ion energy as function of pulse number at start of the burst. Right: ion energy as function of pulse duty cycle (100%=20 μs pulse interval; 50%=40 μs, 33%=60 μs). RFEA blind time of 0.2 μs is marked in gray.

Despite the qualitative understanding of the underlying mechanisms, the shifting balance between gas ionization and SEE terms cannot be described analytically and (hybrid) PIC modeling is required. However, also a PIC model relies on many manual input parameters for e.g. the duration of the UV afterglow and the actual secondary electron emission of real materials and surfaces, so model validation remains crucial, for each EUV source type and for each vacuum vessel design.

The extended tail with 2 eV is not predicted by model, most likely because the super-elastic effect is not captured sufficiently in the model. There is also some discussion on the absolute value of the RFEA energy measurements. During the EUV pulse, the RFEA is clearly affected by spurious photoelectric effects (greyed-out zones in Figure 15 and Figure 16). Also, especially in the fast transient after the EUV pulse, some crosstalk between readout and grids cannot be excluded. Work has started to install an EQP on the LPP Source testrig to verify these aspects of the RFEA.

3.3.10. Radicals

As outlined above, neutral H* radicals will be formed in and near the EUV beam and will diffuse out to the walls. However, the radicals only have a finite likelihood of wall recombination, and for a confined plasma the radical density will build up much more

than the ions. The radical recombination coefficient γ of the walls may vary significantly for different materials, and will also be significantly influenced by the surface state; for clean construction metals it may be assumed to be in order of 0.1.⁵² Furthermore, wall recombination of the H_3^+ ions will create ~ 2 H-radicals per recombining ion on average⁵³. Volume recombination of radicals requires 3-body collisions in view of momentum and energy conservation, so may typically be ignored.

This combination of finite recombination probability and generation at the walls leads to significant build-up of radical flux. One of the important parameters in plasma chemistry is the flux ratio of radicals to ions, which is governed by the respective photon yields and the radical recombination coefficient (ion recombination coefficient is taken to be unity):

$$\frac{\varphi_r}{\varphi_i} \cong \frac{1}{\gamma} \cdot \frac{\eta_r}{\eta_i} \quad (3.23)$$

With φ_r and φ_i the radical and ion fluxes, and η_r and η_i the respective yields per photon. Working out the different reaction pathways for ionization, dissociation and recombination, the yield ratio is roughly 5 radicals per ion. Assuming a recombination coefficient $\gamma \approx 0.1$, radical fluxes may be ~ 50 x higher than ion fluxes for a confined plasma. It should be noted that in contrast to ions, the resulting radical density distribution will be more or less constant in the volume around the EUV beam and will not show appreciable peaking in the beam itself; so the radical-to-ion ratio will be lower inside the beam (and near the mirror surface) and higher further away from the beam. The radicals will not respond to the fast transient electron energy peaks and may be treated as a continuous flux.

The production processes of radicals will result in electronically excited radicals as well as radicals with high kinetic energies of roughly 1 to 8 eV (for dissociative ionization), which will be thermalized by momentum exchange with the background gas and the walls within a few μ s. The majority of the radical flux may thus be assumed to be close to room temperature, but with a broad distribution and a tail with high energies.

Such electronically excited and/or high-energy radicals will be significantly more chemically reactive and will easily overcome absorption barriers of hydrogen into metals or semi-metals, possibly leading to supersaturated surface layers and blistering⁵⁴.

3.3.11. Gas flow

For completeness, also the loss term by flow (or convection) should be considered, as gas in the scanner or test setup will typically be circulated. This is given by the convection residence time τ_{CR} :

$$\tau_{CR} = \frac{\Lambda_p}{v_{H_2}} \quad (3.24)$$

With Λ_p the plasma dimension in the flow direction and v_{H_2} the flow velocity. For a typical flow of $v_{H_2} = 100$ m/s and a plasma confinement size of $\Lambda_p = 2$ cm, $\tau_{CR} \cong 0.2$ ms, which is higher than the ambipolar diffusion constant above but not by orders of magnitude. The flow may therefore have a modest impact, increasing the effective decay rate by $\sim 10\%$. As this effect is small with respect to the other uncertainties, gas flow has been excluded from the 3D Hybrid PIC model and from the present analysis in this paper.

3.3.12. Gas purity

The gas purity is an intrinsic concern for the EUV scanner, because of several reasons: outgassing of reticles coming in from ambient, micro-leaks from load locks and robots, and outgassing from vessel walls (as the delicate scanner system cannot be baked out at high temperature). This can lead to trace gas levels in the RME of N_2 , O_2 , H_2O and volatile hydrocarbons. Even trace levels of these molecules may change the plasma chemistry, driven by higher EUV absorption to form N_2^+ and O_2^+/O_2^- , by exothermic proton transfer to form N_2H^+ and H_3O^+ , and by hydrogen chemistry to form

carbon/nitrogen-containing ions²⁷. The change in plasma composition might also change the plasma characteristics, as these heavier ions would diffuse out more slowly and would thus show more plasma build-up over pulses. Earlier investigations, using isolated pulses, showed that trace amounts of N₂ might indeed affect the plasma composition and chemistry, but do not change the IEDF of the hydrogen ions significantly⁵⁵. This was confirmed recently on a LPP testrig for regular 50 kHz multi-pulse mode of operation. No measurable difference in IEDF was observed for an addition of 10⁻² Pa of N₂ level in 5-10 Pa H₂, as shown in Figure 17.

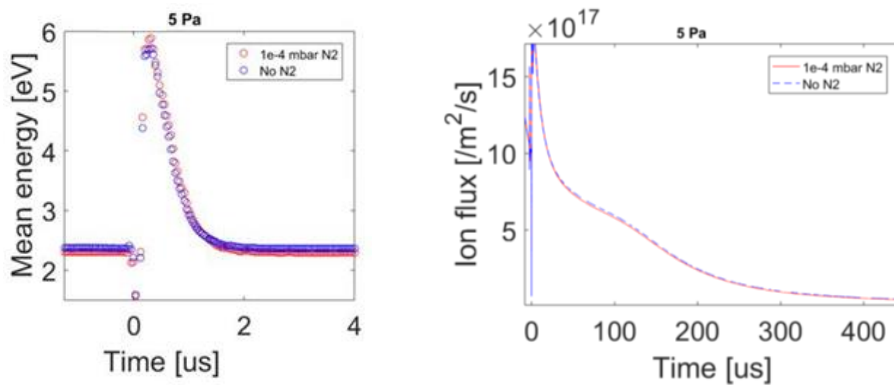


Figure 17: Transient ion energy after EUV pulse, with and without addition of N₂, measured in LPP testrig at the edge to the beam for 5 Pa. Left for fast transient, right for long-term decay after last pulse⁴⁷.

Still, care should be taken about gas purity since the heavier ions may have significantly more impact on materials at same ion energy, and both oxygen and nitrogen compounds may be chemically active^{56,57}. Also, hydrocarbons and volatile hydrides may have significant impact already at trace levels since these may be decomposed by the EUV to result in deposition of carbonaceous layers on mirrors⁵⁸ and reticles⁵⁹.

3.4. Reticle mini-environment

In the scanner, the EUV-induced plasma will be different for different locations within the scanner, since every successive mirror in the optical system will absorb ~30% of light⁶⁰; the typical range of plasma parameters at reticle level are given in Table 2.

Furthermore, at reticle level the geometry around the beam is severely constrained, with reticle masking blades and other surfaces at close proximity, as illustrated in Figure 18. As outlined in section 3.2, the typical length of the RME confinement is $\Lambda_w \approx 1.5$ cm, and only limited build-up of plasma over multiple pulses will occur. The RME dimensions are in order of the mean free path length of the electrons and ions, so ions will experience only few collisions, if any. The resulting narrow slits suppress ambipolar plasma diffusion, but fast photo-electrons may travel through these slits to create secondary ionization events up to ~ 10 cm from the EUV beam. At this location of the scanner, no measurements are possible, and we have to rely on the PIC model and the validation thereof as described above.

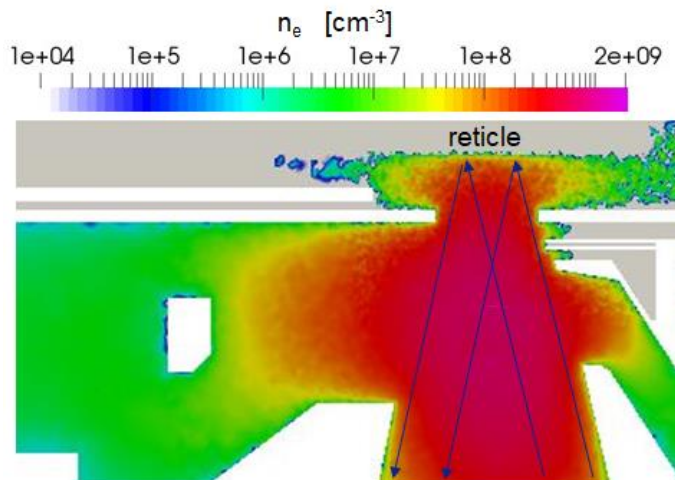


Figure 18: Left: schematic of EUV-induced plasma in RME, showing high plasma density in EUV beam (arrows), but also plasma expansion throughout the volume and in between reticle and reticle masking blades (see Figure 1 for components).

The reticle itself is a patterned reflector. It is irradiated with an EUV beam from the illuminator and reflects the light back into the projection optics, with a diffraction pattern containing the reticle pattern information. The reticle is floating, with independent conductive backside and frontside layers⁶¹. The surrounding surfaces, such as reticle masking blades, uniformity correction blades and other plasma-facing walls are conductive and grounded. As outlined in section 3.3.5, photoelectric effect is significant in the vicinity of mirrors or reticle, and more electrons will actually be

generated from the surface by photoemission than by gas ionization. This results in transient positive charging of the reticle frontside to ~ 30 V during the EUV pulse⁶¹, as shown in Figure 19. When irradiation stops, the low-energy electrons will be re-absorbed by the positively charged surface, which in combination with the electrons from the ionized gas will bring the surface to the same potential as the plasma within the first ~ 1 μ s.

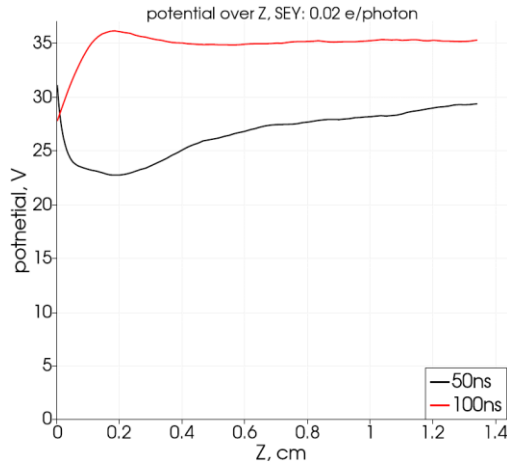


Figure 19: Modeled impact of SEE /SEY on plasma-wall potential at 50 ns (black) and 100 ns (red), showing the initial inverse sheath and subsequent fast transition to classical sheath.

This transient reticle-plasma potential will significantly suppress the peak ion energies towards the reticle in the high-energy phase during and directly after the EUV pulse³².

Table 2: Summary of EUV-induced plasma parameters in RME

Parameter	Value
Incident EUV power	50 W
Plasma electron/ion density	$\sim 10^{15} \text{ m}^{-3}$
Ionization degree	$\sim 10^{-4} \%$
Ion flux	$\sim 10^{17} \text{ m}^{-2}\text{s}^{-1}$
Ion energy	$< 10 \text{ eV}$
Radical flux	$\sim 10^{19} \text{ m}^{-2}\text{s}^{-1}$

3.5. *Off-line emulation of scanner plasma*

For studies of plasma-material interactions as well as plasma-particle interactions it is beneficial to reproduce the EUV-induced plasma conditions inside the scanner with the help of smaller laboratory EUV sources. Typically, laboratory sources have less output power than a commercial LPP EUV Source, so setups often employ a significantly smaller spot to reproduce a similar time averaged EUV irradiance. Beam spots of ~ 1 cm or smaller will show pronounced ion diffusion to the sides, reducing the effective ion load to the irradiated spot, and increasing the ratio of photons to ions and radicals. Also, the repetition rate might be quite different. The scanner LPP Source operates at 50 kHz, while a synchrotron may runs at ~ 0.5 GHz (e.g. PTB Berlin) and a DPP source may run at 1-10 kHz; this is also reflected in the pulse energies, which will be $\sim 10^5$ times higher for DPP than for synchrotron for the same focus spot size. These deltas will significantly change the balance between the quasi-steady-state plasma and the transient peaks, so will result in a different IEDF. A synchrotron may be treated as a continuous source, DPP as isolated pulses, and scanner LPP will be in the middle.

In order to illustrate this, let us study a model situation where the laboratory source focuses EUV radiation into a spot with area 0.1 cm^2 , with a power density of 0.1 mJ/cm^2 per pulse. Three different types of sources are considered: one with a very high repetition rate of 0.5 GHz (synchrotron), one with 50 kHz repetition rate (laboratory LPP) and one with a repetition rate of 5 kHz (DPP). To make the comparison, we used a scanner-like baseline use case with an EUV beam uniformly filling a circle with area 10 cm^2 , using the same EUV irradiance for all sources. Figure 20 shows simulation results for the ion flux to the surface for these four cases. The 0.5 GHz source results in too low ion energies, even if the energy integrated flux in the exposure spot is similar to the baseline case. The 50 kHz source repetition rate results in a similar high energy ion tail as for the scanner case, but the high plasma potential, which is formed during the EUV pulse, causes fast radial expansion of the plasma and reduced ion dose in the exposed area. The case with 5 kHz repetition rate results in high ion energies, and further

reduction of ions in the exposure spot due to enhanced plasma expansion; also, the 10x higher peak irradiance during the pulse at this lower frequency might change the plasma-material interaction.

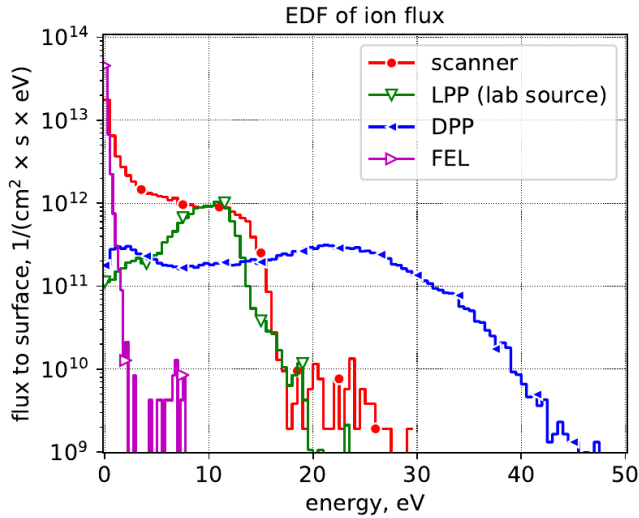


Figure 20: Ion energy distribution function summed over ion types, around center area of spot (~ 0.07 cm²).

So even if the laboratory source can deliver an EUV irradiance matching to scanner, the experimental setup might still need to compensate for the differences in the ion fluxes from the LPP EUV source. To some degree these differences may be corrected: for the 0.5 GHz case the exposed sample could be biased to get the desired energy spectrum, and for the 5 kHz laboratory source a combination of bias and pressure could be used to tune the spectrum. Also, a combination of EUV Source and an inductively/capacitively coupled plasma, and/or a radical source, could be used to achieve the desired ion fluxes and energies.

Besides the temporal and spatial differences, also the spectrum of laboratory setups might be significantly different from the scanner. This might originate from differences in the EUV source (e.g. using Xe instead of Sn, or DPP instead of LPP), or from less effective spectral filtering in the ionizing 14-80 nm wavelength range (e.g. by using

grazing-incidence mirrors instead of normal-incidence Bragg mirrors). Even the extended wavelength range up till ~ 200 nm might be relevant in view of surface electrons potentially being released by photoelectric effect.

The resulting significant discrepancies in plasma characteristics form a major complication in comparing laboratory setups to scanner conditions, and put critical requirements on the physical accuracy of the models used for interpreting and translating results.

To circumvent the issues described above, it is recommended to combine independent sources of EUV photons, ions and radicals. E.g. by combining a focused EUV beam with filament-based radical generation and with biasing of sample and surrounding walls for the ion flux and energies. In case, the EUV photons are not considered relevant, for example a combination of fast electrons from an e-beam and lower-energy electrons from an ICP plasma and a hot-filament radical source could also be a good alternative.

3.6. Conclusion

The existing descriptions of more or less open EUV-induced plasma's were extended with a treatment of confinement, with plasma-facing walls at a distance of order of the mean free path length of the energetic photoelectrons; it was found this requires explicit inclusion of the relatively low-energy secondary electron emission from the walls, which may be induced by photoelectric effect or by secondary electron emission by the energetic photoelectrons.

For a pulsed plasma with a period shorter than the decay time of the plasma, the plasma will consist of a quasi-steady-state cold background plasma, and periodic transient peaks in ion energy and ion flux. This requires a bi-Maxwellian treatment. In terms of modeling, this means no assumptions can be made on the electron distribution functions, and a (Monte-Carlo) Particle-in-Cell (PIC) model is needed. We have presented an extension of the PIC model approach to complex 3D geometries and to multiple pulses, by using a Hybrid PIC-diffusion approach.

It was found that plasma confinement and resulting contributions from secondary electron emission delay the formation of the plasma sheath and thereby reduce the peak ion energies, to below the sputtering threshold for mirrors and construction materials. This holds both for close confinement around the beam as well as for close proximity to an EUV-mirror or the reticle. Materials with a high secondary electron emission may also be beneficiary in this respect, but care should be taken that all materials are robust against hydrogen radicals and ion-enhanced chemical reactions with hydrogen. The UV afterglow of EUV generation might last longer than the EUV pulse itself, and might thereby frustrate sheath formation for some tenths of a microsecond; this also results in reduced peak ion energies as the energetic electrons will cool down fast in the meantime.

In many descriptions of EUV-induced plasma's, radicals are ignored. However, close to the EUV-beam, radicals may have high kinetic energies of >1 eV and might be in an electronically excited state, both of which may further increase reaction rates and enhance hydrogen absorption into (semi)metals. Besides enhanced chemical reaction rates, the high-energy radical fraction in a confined EUV-induced plasma is also a concern for many metals as these radicals will penetrate beyond the surface barrier and may result in e.g. hydrogen embrittlement or blistering, and in case of coatings in loss of adhesion and delamination.

Some discrepancies are observed between the modeled energies and the measured energies. The overestimation in the model for the peak energies in the transient phase is attributed to the possibly too conservative model estimates for the UV afterglow; to clarify this, a time-resolved UV/VUV spectrometer will need to be developed.

The underestimation in the model for the mid-term ion energies is attributed to the super-elastic collision effect not being captured sufficiently in the model. There is also some discussion on the absolute value of the RFEA energy measurements, as the RFEA itself is clearly affected by photoelectric effect from the EUV pulse in the transient phase. Work has started to install an EQP on the LPP Source testrig to verify these aspects of the RFEA.

The peculiarities and transients of the scanner hydrogen plasma make it difficult to translate findings from off-line laboratory EUV setups to scanner. Lower or higher pulse frequencies, as well as small focused spots or different confinement geometries may change the interplay between photons, ions and radicals. Deeper understanding of the scanner plasma will allow better interpretation and translation of findings on off-line setups. It is recommended to explore the use of combined setups to better emulate the EUV plasma, e.g. a combination of ICP plasma with fast electrons from an e-beam and a hot-filament radical source.

Looking towards the future, the EUV power will continue to rise to enable throughput improvements in the scanner. The ion flux will scale linearly with increasing EUV pulse energy, while the ion energy is independent of this, as all electron populations scale equally with power. In case EUV power should be increased further by increasing the LPP frequency, the balance between the electron contributions from the gas and from the surface will shift towards the gas, and as a result the ion energy will increase.

3.7. *References*

-
- ¹ O. Braginsky et al, “Removal of amorphous C and Sn on Mo: Si multilayer mirror surface in Hydrogen plasma and afterglow”, *Journal of Applied Physics* (2012)
- ² M. van de Kerkhof et al, “Advanced particle contamination control in EUV scanners”, *Proc. Of SPIE Vol. 10957* (2019)
- ³ F. Torretti et al, “Spectral characterization of an industrial EUV light source for nanolithography”, *J. Phys. D: Appl. Phys.* (2019)
- ⁴ M. van de Kerkhof et al, ‘Spectral purity performance of high-power EUV systems’, *Proc. of SPIE Vol. 11323* (2020)
- ⁵ M. Lowisch et al, “Optics for EUV production”, *Proc. of SPIE Vol. 8679* (2010)
- ⁶ E. Louis, et al, “Multilayer coated reflective optics for extreme UV lithography”, *Microelectronic Engineering*, (1995)

-
- ⁷ M. van der Velden, “Radiation Generated Plasmas: A Challenge in Modern Lithography” PhD thesis (2008)
- ⁸ M. Lieberman, “Principles of plasma discharges and materials processing” (2005)
- ⁹ T. van de Ven, “Ion fluxes towards surfaces exposed to EUV-induced plasmas”, PhD thesis, Technical University Eindhoven (2018)
- ¹⁰ M. van de Kerkhof et al, “Advanced particle contamination control in EUV scanners”, Proc. Of SPIE Vol. 10957 (2019)
- ¹¹ V. Demidov et al, “Nonlocal effects in a bounded afterglow plasma with fast electrons” IEEE Transactions on plasma science (2006)
- ¹² V. Godyak et al, “Tonks-Langmuir problem for a bi-Maxwellian plasma”, IEEE transactions on plasma science (1995)
- ¹³ M. van der Velden, “Radiation Generated Plasmas: A Challenge in Modern Lithography” PhD thesis (2008)
- ¹⁴ <https://www.impedans.com/semion-single-sensor> (2021)
- ¹⁵ T. van de Ven et al, “Analysis of retarding field energy analyzer transmission by simulation of ion trajectories”, Review of Scientific Instruments (2018)
- ¹⁶ M. van der Velden et al, “Particle-in-cell Monte Carlo simulations of an extreme ultraviolet radiation driven plasma”, Phys. Rev. E (2006)
- ¹⁷ D. Astakhov et al, “Exploring the electron density in plasma induced by EUV radiation: II. Numerical studies in argon and hydrogen”, J. Phys. D Appl. Phys. (2016)
- ¹⁸ T. van de Ven, “Ion energy distributions in highly transient EUV induced plasma in hydrogen”, J. Appl. Phys. (2018)
- ¹⁹ A. Lipatov, “The Hybrid Multiscale Simulation Technology: An Introduction with Application to Astrophysical and Laboratory Plasmas”, Springer Berlin Heidelberg, Berlin (2002)
- ²⁰ J. Samson et al, “Total photoabsorption cross sections of H₂ from 18 to 113 eV”, J. Opt. Soc. Am. B (1994)
- ²¹ Y. Chung et al, “Dissociative photoionization of H₂ from 18 to 124 eV”, J. Chem. Phys. 99 (1993)
- ²² H. Kossmann et al, “Photoionisation cross section of H₂”, Journal of Physics B: Atomic, Molecular and Optical Physics (1989)
- ²³ T. Sharp, “Potential-energy curves for molecular hydrogen and its ions”, Atomic Data and Nuclear Data Tables 2 (1970)

-
- ²⁴ J. Berkowitz, "Atomic and Molecular Photoabsorption: Absolute Partial Cross Sections", Elsevier Science (2015)
- ²⁵ J. Yoon et al, "Cross Sections for Electron Collisions with Hydrogen Molecules", J. Phys. Chem. Ref. Data (2008)
- ²⁶ H. Tawara et al, "Cross sections and related data for electron collisions with hydrogen molecules and molecular ions", Journal of Physical and Chemical Reference Data 19.3 (1990)
- ²⁷ T. Oka, "Interstellar H₃⁺", Chem. Rev. 113 (2013)
- ²⁸ T. Tabata, "Analytic cross sections for collisions of H⁺, H₂⁺, H₃⁺, H, H₂, and H⁻ with hydrogen molecules", At. Data Nucl. Data Tables (2000)
- ²⁹ H. Hertz, "Ueber einen Einfluss des ultravioletten Lichtes auf die electrische Entladung", Ann. der Physik und Chemie (1887)
- ³⁰ R. Day et al, "Photoelectric quantum efficiencies and filter window absorption coefficients from 20 eV to 10 keV", Journal of Applied Physics (1981)
- ³¹ B. Yakshinskiy, "Carbon accumulation and mitigation processes, and secondary electron yields of ruthenium surfaces", Proc. of SPIE Vol. 6517 (2007)
- ³² P. Krainov et al, "Dielectric particle lofting from dielectric substrate exposed to low-energy electron beam", Plasma Sources Science and Technology (2020)
- ³³ M. van der Velden et al, "Kinetic simulation of an extreme ultraviolet radiation driven plasma near a multilayer mirror" J. Appl. Phys. (2006)
- ³⁴ R. van der Horst, "Electron dynamics in EUV-induced plasmas", PhD thesis, Technical University Eindhoven (2016)
- ³⁵ N. Balcon et al, "Secondary electron emission on space materials: Evaluation of the total secondary electron yield from surface potential measurements", IEEE Transactions on Plasma Science (2011)
- ³⁶ X. Wang et al, "Plasma potential in the sheaths of electron-emitting surfaces in space", Geophysical Research Letters (2016)
- ³⁷ Y. Lin et al, "A New Examination of Secondary Electron Yield Data", Surface and Interface Analysis (2005)
- ³⁸ B. Tembe, "Electron thermalization in gases. V. Diatomic molecules H₂, N₂, and CO", J. Chem. Phys. (1983)
- ³⁹ J. Beckers et al, "Time-resolved ion energy distribution functions in the afterglow of an EUV-induced plasma", Applied Physics Letters (2019)

-
- ⁴⁰ H. Ellis et al, "Transport properties of gaseous ions over a wide energy range", *At. Data Nucl. Data Tables* 17(1) (1976)
- ⁴¹ D. Albritton et al, " Mobilities of mass-identified H₃⁺ and H⁺ ions in hydrogen", *Phys. Rev.* (1968)
- ⁴² R. Plasil et al, 'Advanced integrated stationary afterglow method for experimental study of recombination of processes of H₃⁺ and H₃⁺ ions with electrons', *Int. J. Mass Spectrom.* (2002)
- ⁴³ G. Hobbs et al, "Heat flow through a Langmuir sheath in the presence of electron emission" *Plasma Physics* (1967)
- ⁴⁴ M. Campanell, "Negative plasma potential relative to electron-emitting surfaces." *Physical Review E* (2013)
- ⁴⁵ M. Larsson et al, "The dissociative recombination of H₃⁺ – a saga coming to an end?", *Chemical Physics Letters* (2008)
- ⁴⁶ P. Dohnal, "H₂-assisted ternary recombination of H₃⁺ with electrons at 300 K", *Physical Review A* (2014)
- ⁴⁷ M. van Kampen, internal ASML report (2020)
- ⁴⁸ M. Lieberman et al, "Global models of pulse-power-modulated high-density low-pressure discharges", *Plasma Sources Sci. Techn.* (1996)
- ⁴⁹ V. Demidov et al, "Nonlocal effects in a bounded afterglow plasma with fast electrons", *IEEE Transactions on Plasma Science* (2006)
- ⁵⁰ M. Osiac et al, "Plasma boundary sheath in the afterglow of a pulsed inductively coupled RF plasma", *Plasma Sources Sci. and Techn.* (2007)
- ⁵¹ A. Maresca et al, "Experimental study of diffusive cooling of electrons in a pulsed inductively coupled plasma", *Physical Review* (2002)
- ⁵² M. Mozetič et al, "Recombination of neutral hydrogen atoms on AISI 304 stainless steel surface", *Appl. Surf. Sc.* (1999)
- ⁵³ I. Mendez et al, "Atom and ion chemistry in low pressure hydrogen DC plasmas", *Journal of Physical Chemistry A* (2006)
- ⁵⁴ W. Shu et al, "Microstructure dependence of deuterium retention and blistering in the near-surface region of tungsten exposed to high flux deuterium plasmas of 38 eV at 315 K", *Physica Scripta* (2007)
- ⁵⁵ J. Beckers et al, "Energy distribution functions for ions from pulsed EUV-induced plasmas in low pressure N₂-diluted H₂ gas", *Applied Physics Letters* (2019)

-
- ⁵⁶ P. Phadke et al, “Sputtering and nitridation of transition metal surfaces under low energy, steady state nitrogen ion bombardment” Appl. Surf. Sci. (2020)
- ⁵⁷ P. Phadke et al, “Oxidation and sputtering of transition metals by oxygen ions at steady state: Sputtering and radiation enhanced diffusion near sputter threshold”, Appl. Surf. Sci. (2020)
- ⁵⁸ J. Hollenshead et al, “Modeling radiation-induced carbon contamination of extreme ultraviolet optics”, J. Vac. Sci. Technol. B (2006)
- ⁵⁹ Y. Fan et al, “Carbon contamination topography analysis of EUV masks”, Proc. of SPIE Vol. 7636 (2010)
- ⁶⁰ E. Louis, et al, “Multilayer coated reflective optics for extreme UV lithography”, Microelectronic Engineering, 27 (1995)
- ⁶¹ M. van de Kerkhof et al, “Plasma-assisted Discharges and Charging in EUV-induced Plasma”, Journal of Micro/Nanopatterning, Materials, and Metrology (2021)

4

4. Plasma-assisted discharges and charging

This chapter is based on following publication:

- *Mark van de Kerkhof, Andrei Yakunin, Vladimir Kvon, Selwyn Cats, Luuk Heijmans, Manis Chaudhuri, Dmitry Astakhov, "Plasma-assisted Discharges and Charging in EUV-induced Plasma", Journal of Micro/Nanopatterning, Materials, and Metrology (2021)*

4.1. Introduction

The EUV-induced plasma can interact with the electrostatics and electronics in the lithographic scanner in several ways: it can e.g. reduce the safe voltage in terms of gas breakdown and can charge floating surfaces. In the subsequent sections these aspects will be described in more detail and design consideration will be discussed.

As outlined in section 3, in theory the energetic photoelectrons of 76 eV, as created in hydrogen ionization by 92 eV EUV photons, may set up a maximum plasma-to-wall potential difference in order of $76 \text{ V}^{\frac{1}{2}}$. In practice, this plasma-wall potential will be reduced by photo-electric effect which results in low-energy electrons being released from any wall (or mirror) irradiated by the EUV beam or by EUV flare, by secondary electron emission, and by charge compensation by ions; the resulting steady state potential of floating surfaces and dielectrics exposed to the EUV-induced plasma is in order of a few volts (typically $\sim 2 \text{ V}$). The mean free path of the energetic photoelectrons will be $\sim 5 \text{ cm}$ at 5 Pa , and the plasma will be larger in dimensions than the EUV beam itself, so charging of floating surfaces within the scanner vessel may occur up to significant distances from the EUV beam.

Care should be taken with using standard equations for the plasma sheath and potential drop over the sheath, since the underlying thermal equilibrium assumptions are not always satisfied, but they give a reasonable approximation for the steady-state background plasma in between the EUV pulses. For a 250 W Source, the sheath thickness can be estimated to be in order of $\sim 0.1\text{-}1 \text{ mm}$ in and close to the EUV beam; the electric field at the surface may be estimated to peak at up to $\sim 100 \text{ kV/m}$ inside the beam during the EUV pulse, and up to $\sim 10 \text{ kV/m}$ close to the beam.

For particle contamination control, the RME zone of the scanner around the reticle is of specific interest, as particles on the reticle have the most severe impact. The reticle is clamped to a scanning stage and faces downwards, with metal reticle masking blades and other conductive surfaces in close proximity. The resulting slits suppress diffusion of the plasma, and transport of plasma through these slits is largely driven by the fast photo-electrons, as shown in Figure 1.

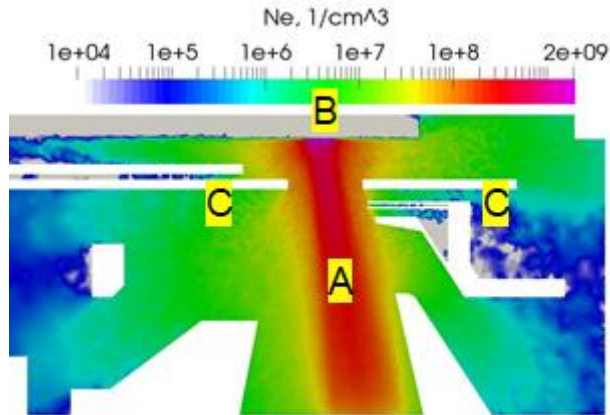


Figure 1: Schematic of reticle zone, showing EUV beam region (A), floating reticle surface (B), grounded reticle masking blades (C). During the EUV pulse the photoelectrons from the EUV beam penetrate through the slits and plasma may exist well beyond the confines of the beam.

The strong transients and non-Maxwellian energy distribution function during and after the EUV pulses precludes the use of fluid-like models, which rely on continuity equations for moments of the distribution functions for electron density, velocities and energies. Instead, a kinetic model must be used, such as (Monte-Carlo) Particle-in-Cell (PIC)². Recently, we have further extended this model to a full 3D PIC model, with options to speed up calculations by hybridization of the model with a fluid-like model for the cooled electrons.

4.2. Plasma and electronics: plasma assisted discharges

Classically, the risk of discharges is described by the Paschen criterion. This describes the condition where the gain factor by cathode electron generation plus gas ionizations by accelerating electrons exceeds the loss factor of electrons to the anode surface, to trigger a self-amplifying discharge³. This requires that electrons can gain enough energy between collisions, requiring a sufficiently long mean free path and high enough electric field, but also have sufficient collisions. These considerations yield a voltage threshold as function of gas type, pressure and distance, above which a self-amplifying avalanche effect will occur, driving the current through the gas sharply up. This

breakdown voltage can be plotted versus pressure-times-distance (p.d), which is called the Paschen curve (see Figure 2). Compared to air, hydrogen has a relatively low minimum breakdown voltage of 273 V, at $p.d = 1.5 \text{ Pa}\cdot\text{m}^4$; for pressures of $\sim 5 \text{ Pa}$ this translates to critical distances of $\sim 30 \text{ cm}$.

For a near-vacuum system, left of the minimum, the Paschen criterion in principle allows very high voltages⁵. Care should be taken though for long discharge path lines (e.g. to vessel walls), and for points of field amplification, such as a sharp edge or protrusion, or a particle, especially at the anode⁶. A notable concern is coating edges, such as on both backside and frontside of the reticle coating edge, which will have an effective submicron edge radius, resulting in significant field amplification (which can be exacerbated by the triple point junction of dielectric glass substrate, conductive coating and vacuum). Also, care should be taken that AC or switching voltages can reduce the Paschen threshold⁷. Given the high energy densities, a Paschen-discharge may easily both generate and release particles, mainly by local overheating at the point of contact of the electrons.

While the Paschen criterion has proven to work well in ambient conditions (to the right of the minimum), the concept is more tenuous in (near-)vacuum, for several reasons: surface properties and feedback mechanisms become more important w.r.t. gas properties, adsorbed gases can become dominant over background gas (especially H_2O , but also e.g. O_2 and N_2), and curved electrical field lines at electrode edges can lead to longer discharge paths⁸. At the same time, surfaces can act both as electron sinks and (secondary) electron sources; thus, as illustrated in e.g. Figure 2, the minimum breakdown voltage may be increased in presence of surfaces, but the steep slope for the low-p.d regime may also be significantly reduced: in this case, even at low p.d values, critical discharge voltages may remain limited to well below 1 kV, in contradiction of Paschen prediction.

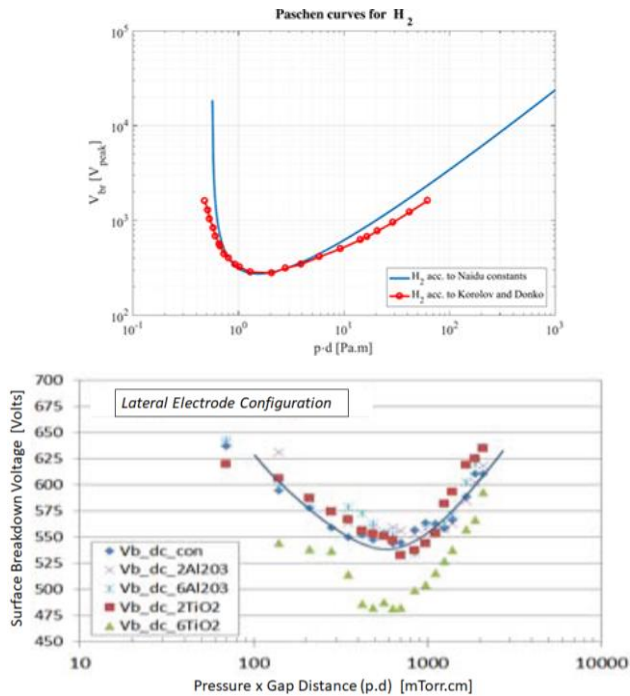


Figure 2: Top: Paschen curve for H₂, showing good match between analytical expression and measurements⁹. Bottom: Modified breakdown curves in presence of a surface (insulating epoxy, with different Al₂O₃/TiO₂ nanoparticle additions), showing a much more gentle slope at low $p \cdot d$ -values (from Li¹⁰).

In-house experiments confirmed these trends, as shown in Figure 3. A slowly increasing voltage (2 V/s) was applied to a reticle placed on top of a standard baseplate in a low-pressure N₂ environment, with insulating polyimide spacers of $\sim 100 \mu\text{m}$. This confirmed discharges at voltages well below the Paschen prediction and with a weaker pressure dependence than predicted by classical Paschen theory, consistent with the findings in Figure 2. Figure 3 also shows that while lower pressure allows for somewhat higher voltage, the amplitude of the discharge is larger. Tests at 5 Pa did not show discharges up to 800 V.

The discharges caused particle removal from the reticle. In the experiment, the baseplate was seeded with $5 \mu\text{m}$ SiO₂ particles. These were observed to be removed from the baseplate and transferred to the reticle. This is not simple electrostatic release, as one might expect for field strengths in order of $\sim 5 \text{ MV/m}$ ¹¹, because it is not observed for 5 Pa and lower pressures, which were exposed to the highest fields: up to

8 MV/m. It is correlated to the local discharges that happen at pressures of 10 and 40 Pa at lower field strengths (respectively 7 MV/m and 4.5 MV/m). Our proposed explanation is that the particles act as field amplification points to trigger discharges which also release the particle; so far this hypothesis could not be positively confirmed due to insufficient accuracy in measuring pre and post conditions.

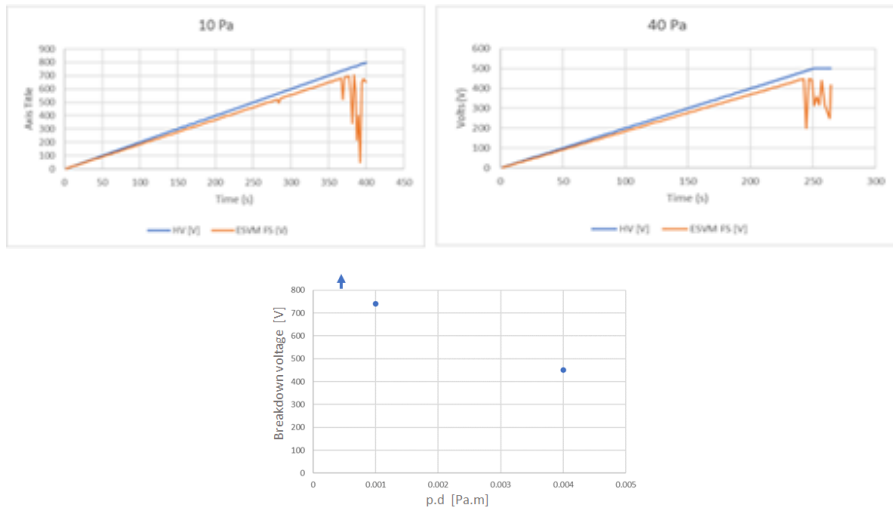


Figure 3: Top: gradual voltage ramp at 2 V/s until breakdown for 10 and 40 Pa; blue line is applied voltage to frontside, red line is frontside voltage measured by SVM. Bottom: summary of the breakdown voltages versus p.d (no discharge was observed at 5 Pa for up to 800 V maximum)¹².

When surface aspects dominate, this also implies a higher likelihood of surface flashovers versus through-gas discharges to opposite surfaces¹³. For reticle discharges as outlined above, this is a concern for frontside defectivity, since a flashover from the charged backside via the floating frontside to the (grounded) baseplate would increase the risk of particles being generated that can reach the frontside. In view of this, it is advised to have dissipative reticle support studs to allow the reticle to gradually discharge to the baseplate.

In presence of plasma, the free electrons and ions invalidate the basic Paschen assumptions, and result in a significant shift of the avalanche threshold to lower voltages. In itself, the plasma will not focus either electrons or ions, so local discharge-

like damage such as overheating is not to be expected from plasma. However, in combination with an external voltage, current focusing can indeed occur, and such a plasma-assisted discharge can induce surface damage and create particles. This is obviously a concern for the high-voltage electrostatic clamps used in the EUV scanner¹⁴, so these must be perfectly shielded from EUV, including the volume extending several cm's around the EUV beam. Less straightforward is that this is also a concern for switching power supplies and circuit boards for fast sensors, which in practice can have voltages above 100 V¹⁵, so these also must be properly shielded from the EUV-induced plasma.

Interaction of a plasma with biased electrodes can lead to formation of different structures¹⁶. When the bias voltage of positively biased electrode becomes too high, formation of the so-called 'fireball' structure may occur. Formation of a 'fireball' in the scanner vessel is not intended, as it is very similar to a discharge, and a large current can be focused into a small area. In the presence of slits and complicated geometries the conditions for formation of the 'fireball' and similar discharges will be different as compared to bulk plasma.

We studied this with our PIC model, and validated experimentally in a set-up with a simplified geometry, as shown in Figure 4. This geometry was modeled using a fast 2D PIC model, for computational efficiency, with the same underlying physics and cross sections as our 3D-PIC model used for more realistic geometries.

The model shows a breakdown or discharge towards the positive anode when the plasma is switched on. This may be explained by electrons being accelerated towards the anode and achieving sufficient energy for further ionizations of hydrogen molecules. As the electrons are accelerated further to the positive anode, a positively charged plasma cloud is formed which screens the electrode potential and moves the zone of electron acceleration away from the electrode, thus effectively forming a channel of current, as illustrated in Figure 5. This is a similar mechanism to streamer formation in tip-shaped anodes¹⁷. Once this channel is fully formed, after $\sim 2\text{-}3 \mu\text{s}$, breakdown is complete as shown by the sharp increase in current.

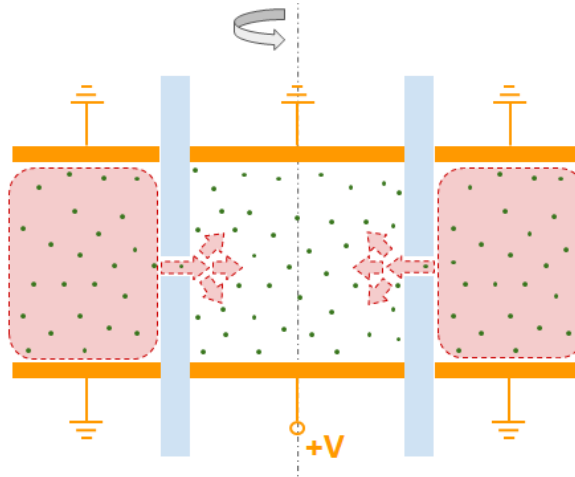


Figure 4: Simplified 2D model geometry. Depicted are the cylindrical tube with a dielectric wall (gray), electrodes (orange) and plasma-filled region (pink). Neutral H₂ gas is represented with green dots.

In contrast to Paschen theory, the plasma-assisted breakdown is not determined simply by the product of distance and pressure: for a given distance, higher pressure and/or higher plasma power result in higher plasma electron density and lower breakdown voltage.

As Figure 6 illustrates, the model shows a peaked threshold behavior in the current at the moment of breakdown for higher pressure (10 Pa); this is the so-called 'Fireball' mode. For lower pressure (1 Pa), the model shows an oscillating current, but no breakdown, since the number of ions formed in this case is too low to achieve sufficient screening of the positive electrode to move the acceleration zone away from the anode and form the conductive channel as above. In that case, the plasma formed will remain in an oscillatory anode glow mode.

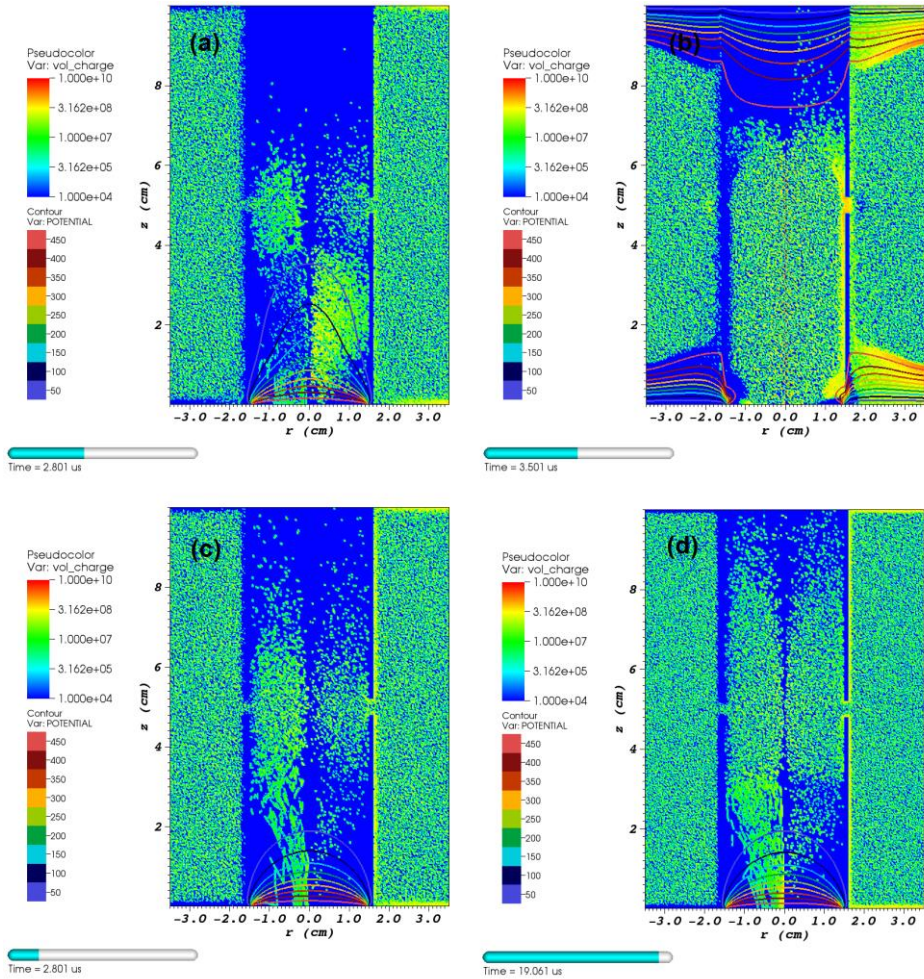


Figure 5: Simulated plasma dynamics for 10 Pa (a,b) and 1 Pa (c,d), showing electron and ion densities (left and right side of each image) and voltage contour lines, for specific time stamps. Anode potential was set to 500 V. The snapshots for 10 Pa show the transition to breakdown at $\sim 3 \mu\text{s}$, while the snapshots for 1 Pa show the more or less stable anode glow.

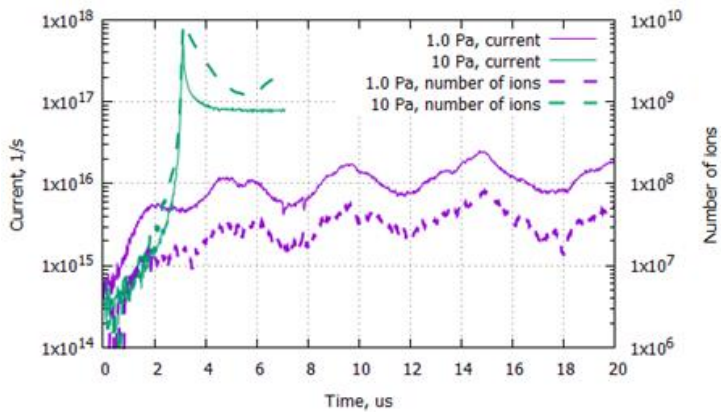


Figure 6: Model showing avalanche and breakdown at 10 Pa, with sharply peaked increase in current (green line); and oscillating glow discharge at 1 Pa (purple line).

The experimental set-up is essentially a cylindrical tube with two electrodes and an option to add free charge carriers from an RF plasma, as shown schematically in Figure 7. Hydrogen pressure was varied in the range of 1 – 10 Pa, and RF power varied between 10 to 60 W and the distance between electrodes was varied in range of 1 – 10 cm. For any given combination of these parameters, the bias voltage on the positive electrode is scanned from 0 – 250 V, remaining always below the Paschen minimum of hydrogen, while the electrode currents were measured continuously by a multimeter.

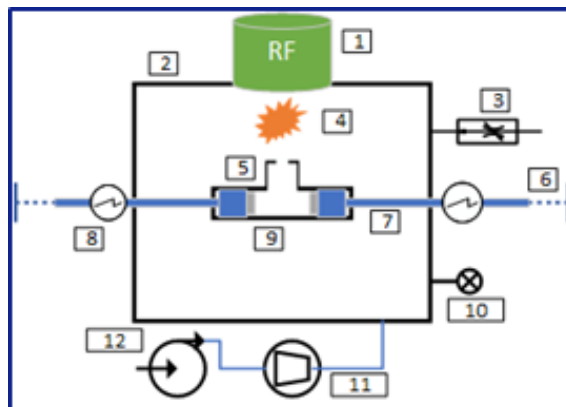


Figure 7: Experimental setup for plasma-assisted discharge: 1 – RF generator; 2 – stainless steel chamber; 3 – valve; 4 - hydrogen plasma; 5 – glass tube; 6 - micrometer translation stage; 7 – insulated PTFE rod with connector; 8 – power supply/multimeter; 9 – stainless steel electrode; 10 – pressure gauge; 11 – turbo-pump; 12 – rotary pump.

The resulting breakdown threshold was observed to be in order of ~ 100 V, significantly below the predicted Paschen threshold for this configuration and even well below the theoretical Paschen minimum of 273 V. It was also confirmed that the avalanche is directed towards the anode, while the ion current to the cathode is $\sim 10\times$ lower. As predicted by the model, the moment of breakdown shows a sharp peak in current, after which a steady high current flows and voltage drops somewhat, as shown in Figure 8. Varying conditions of electrode distance and pressure resulted in observations of breakdown below and around the Paschen minimum voltage, even for low pressure and short distances, in what classically should be a 'safe' zone of p.d-V combinations.

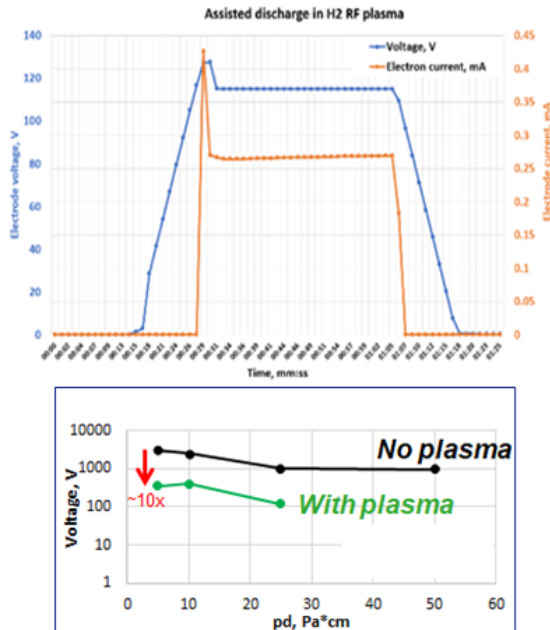


Figure 8: Top: example of plasma-assisted discharge and current when ramping up voltage between electrodes while plasma switched on in neighboring chamber (using 60W plasma, 5 Pa, 10 cm distance). Bottom: examples of significant reduction of breakdown voltage when plasma is switched on (10W plasma; 5 cm distance); both with and without plasma, the observed breakdown voltages at low pressures are all significantly reduced with respect to classical Paschen prediction of $>10^5$ V, which is attributed to the glass tube surfaces.

In general, the critical ion density n_i^{crit} to trigger a plasma-assisted discharge can be estimated from the condition of positive electrode screening: the potential drop due to volume charge should be comparable with the electrode potential drop:

$$n_i(t) > n_i^{crit} \sim \frac{2\epsilon_0}{e} \cdot \frac{\varphi}{h^2} \sim 10^8 \text{ cm}^{-3} \quad (4.1)$$

With the electrode potential drop $\varphi \approx 30\text{-}70$ eV (accelerating electrons to energies at which ionization is most efficient¹⁸), the region of ion accumulation $h \approx 1$ cm, and e the elementary charge. This estimate of n_i^{crit} is in line with the 2D PIC simulations above. In more complicated geometries, the exact value of the critical ion density will depend on the (in)homogeneity of the electric field and the distance of the plasma source to the anode. Rather than the discharge threshold being determined by voltage and the product of pressure and distance (i.e. by Paschen criterion), the discharge threshold is now driven by applied voltage V_{ext} , pressure p_{H2} and local plasma density, which in turn scales with EUV power P_{EUV} and also with pressure p_{H2} , with a correction factor γ_{dist} that describes the fall-off of plasma away from the EUV-beam:

$$n_i^{crit} \sim V_{ext} \cdot p_{H2}^2 \cdot P_{EUV} \cdot \gamma_{dist} \quad (4.2)$$

Equation 4.2 illustrates that the risk of plasma-assisted discharge needs to be re-evaluated for any increase in either EUV power, local pressures or external voltages. For the complicated internal geometries of an EUV-scanner, no analytical expression exists. However, our 3D PIC model, with the same underlying physics and cross sections as the 2D PIC model as used and validated above, can now be used to check any design proposal for safe limits on local voltages and pressures plasma-assisted discharges. Also, as general guidelines, floating or insulating surfaces should be avoided as much as possible to minimize the risk of surface flashovers, and edges and protrusions should be sufficiently rounded to avoid dangerous field amplification points.

4.3. Reticle charging and discharges

Floating surfaces and dielectrics close to the EUV-induced plasma may become charged. In particular the reticle needs to be considered in this respect, since it consists of an insulating glass substrate with a conductive coating on the backside (for electrostatic clamping purposes), and a conductive reflective multi-layer coating on the frontside; both conductive layers are floating independently; this is outlined in Figure 9.

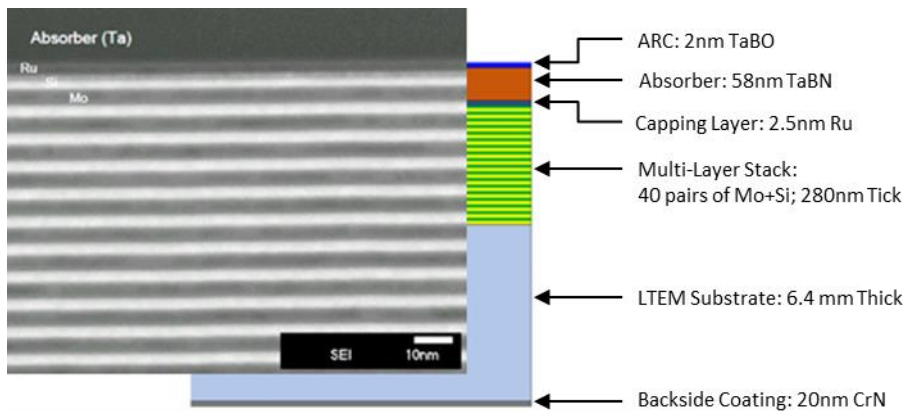


Figure 9: Sketch of reticle cross-section, showing conductive coating stacks on frontside and backside; adapted from McLellan¹⁹.

The reticle backside is clamped electrostatically to a movable positioning module, while the frontside is directly exposed to the EUV beam and EUV-induced plasma. Grounding of the reticle has proven to be impractical in view of the severe risk of particles generated when making electrical connection through the oxide top layers on the moving/scanning reticle²⁰. During exposures the reticle frontside will acquire a transient potential due to competing direct photoelectric effect from EUV irradiation (driving to positive) and subsequently de-charging from plasma, and will return to ~ 0 V after every pulse, as shown in Figure 10.

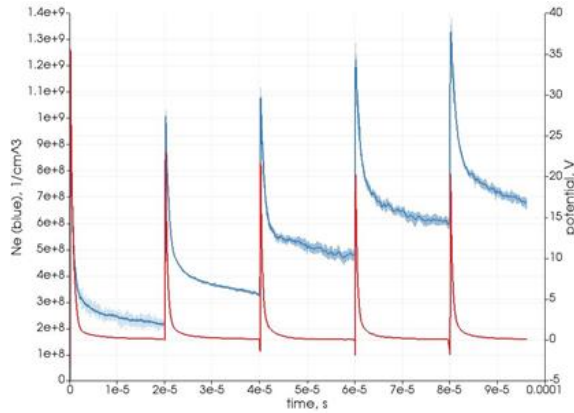


Figure 10: PIC simulation of electron density (blue line) and reticle frontside surface potential (red line), showing accumulation of plasma over pulses but no build-up of surface potential.

The reticle backside is quite different, since this is not exposed directly to EUV irradiation and shielded by the clamp. The backside coating plane is connected to the plasma volume through only a small gap, which acts as a spatial filter to suppress diffusion for both positive and negative charges. Still, two effects can result in charging of the reticle backside: secondary gas ionizations by the energetic photoelectrons and secondary electron emission by the surrounding clamp, of which secondary gas ionizations are expected to be dominant.

Secondary ionizations in the gas surrounding the reticle result in electrons propagating more or less isotropically around the actual EUV beam, which allows electrons to reach the conductive backside coating even if the coating is recessed from the edge. The ions have a lower likelihood to reach the backside as these are accelerated more along the electrical field lines, scatter less and have higher inertia; so ions will likely hit surrounding surfaces and stick there. This results in a net negative charging of the reticle backside, as is shown schematically in figure 14.

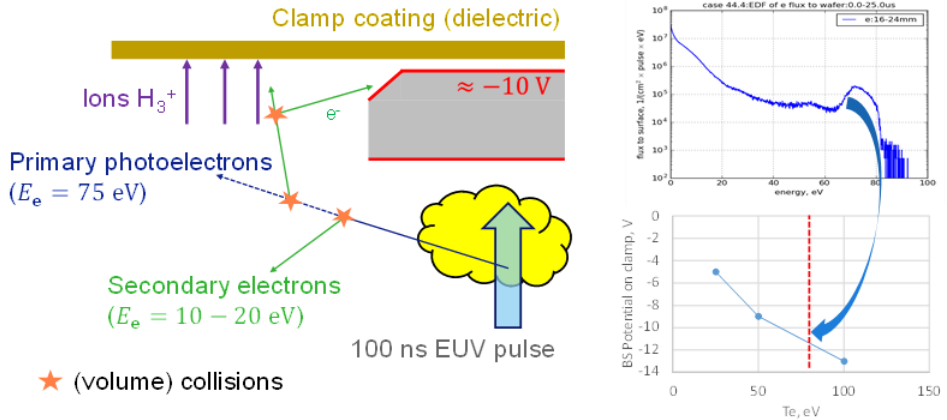


Figure 11: Left: basics of charging mechanism of reticle backside; Top right: energy spectrum of electrons reaching reticle edge modelled by 3D PIC code. Bottom right: energetic secondary electrons charge reticle backside, while ions are carried by field and momentum towards nearest wall.

As the reticle backside charge and voltage build up, electrons will be repulsed and ions attracted, which will result in an equilibrium charge and voltage, which will depend on details of plasma (e.g. EUV power, pressure and beam position with respect to reticle edge). PIC modelling for the reticle geometry in NXE:3400 of electron spectrum reaching the backside reticle edge shows that the cumulative process of charging by fast electrons and partial neutralization by ions result in an equilibrium negative voltage in order of -10 V. This voltage, and the associated excess electrons, will remain on the reticle backside after the plasma fully decays at the end of exposures. The backside voltage has been simulated to scale inversely quadratically with increasing pressure, as shown in Figure 12; this is due to the combined effect of reduced average frontside potential and increased collisions at higher pressure which act to reduce the high-energy tail of the EEDF.

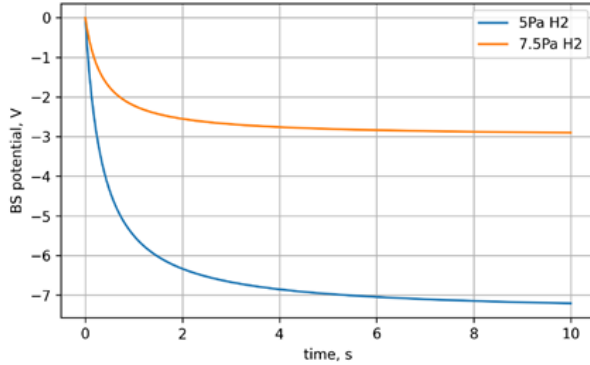


Figure 12: PIC simulations of backside voltage dependence on time and pressure, showing >2x reduction in voltage for 1.5x higher pressure.

Also reticle geometry and coating details are relevant: a recessed coating will show a higher equilibrium charge since this will increase the spatial filtering of ions, and more so than for electrons (due to secondary electron emission or bouncing of electrons from surfaces). This implies an additional consideration for the reticle backside coating beyond the existing specifications for clamping, with the coating preferably extended as close as possible to the edge. The acquired backside voltage may seem negligible, but during reticle unloading the backside voltage is amplified by the changing capacitance between reticle and clamp, as outlined in Figure 14, while the charge locked onto the floating surface remains constant²¹. This is reflected in the basic equations:

$$U = \frac{Q}{C} = \frac{Q \cdot d}{\epsilon_0 \cdot A_{cl}} \quad (4.3)$$

$$U_{unl} = U_{cl} \cdot \frac{d_{unl}}{d_{cl}} \quad (4.4)$$

With A_{cl} the (constant) area of the clamping electrode, U_{unl} the backside potential during unload, U_{cl} the backside potential as clamped, d_{cl} the distance as clamped, which is in order of microns, and d_{unl} the distance during unloading, which is in order of cm's (as sketched in Figure 13), giving a potentially >1000x increase.

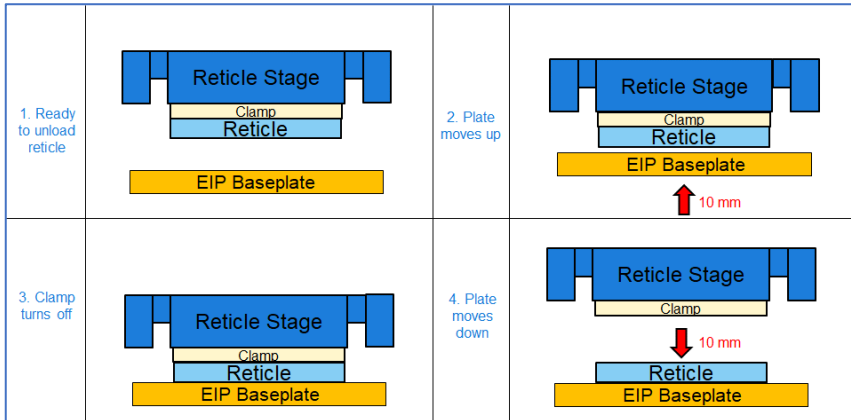


Figure 13: Illustration of reticle unloading sequence. While clamped the separation between reticle backside and clamp electrode is in order of a few micrometers, resulting in strong capacitive coupling; during unload the separation is increased to ~ 1 cm, reducing the capacitance by several orders of magnitude.

In reality, capacitive coupling between backside and frontside and to the unloading plate will complicate these equations and limit the voltage amplification to about 50x, as shown in Figure 14; this still means that during unloading the backside potential can reach a value of up to 1000 V. This is well above the Paschen minimum of ~ 275 V for H_2 , implying a risk of electrostatic breakdown and discharges.

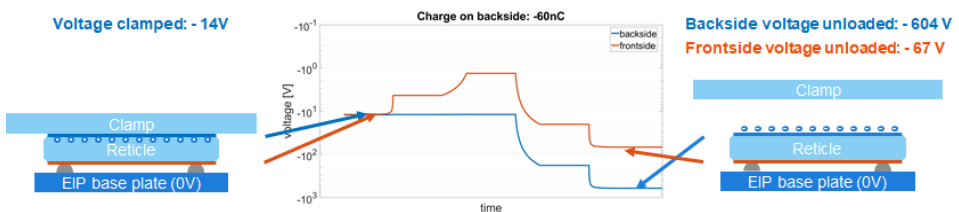


Figure 14: Example of backside (BS) potential amplification from ~ 14 V to ~ 600 V during reticle unload (blue line), caused by stepwise increasing gap between reticle and clamp; also shown is the induced frontside voltage (red line)²².

The high level of reticle charging has been confirmed by electrostatic voltage measurements (ESVM), using dual Trek PD15035 555P-style probes with a 6000B-6 sensor (in combination with a modified reticle pod to allow simultaneous access of the probes to reticle front and backside), directly after unloading the reticle from the

scanner. Figure 15 shows comparison of reticle backside voltage measured after full reticle cycle through EUV machine with and without EUV exposures. Test reticles exposed to EUV confirm the high voltage of ~ 600 V, while reticles that were not exposed to EUV remained neutral. Optical microscope inspection of these test reticles indicated cosmetic damage of reticle backside coating after EUV exposures, which could be traced back to imperfections in the coating edges on the test reticles used, but also showed a clear sensitivity to backside discharges from these high backside voltages.

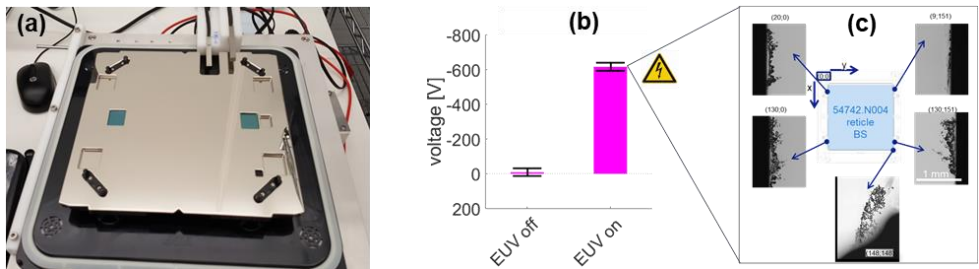


Figure 15: Left: modified reticle pod for ESVM measurements; Middle: ESVM measurement of high voltage on reticle backside when reticle has been exposed to EUV; Right: Observation of ESD damage on a test reticle.

Besides this backside discharge risk (which might in practice be acceptable, since the backside is not as critical as the imaging frontside of the reticle), the increase of backside voltage during unload also induces a frontside voltage in order of 70 V by their capacitive coupling (red line in Figure 14), which might not be so high as to cause concerns for discharges to the critical reticle frontside surface, but is a concern for particle attraction to the reticle, as demonstrated by Amemiya (see Figure 16)²³.

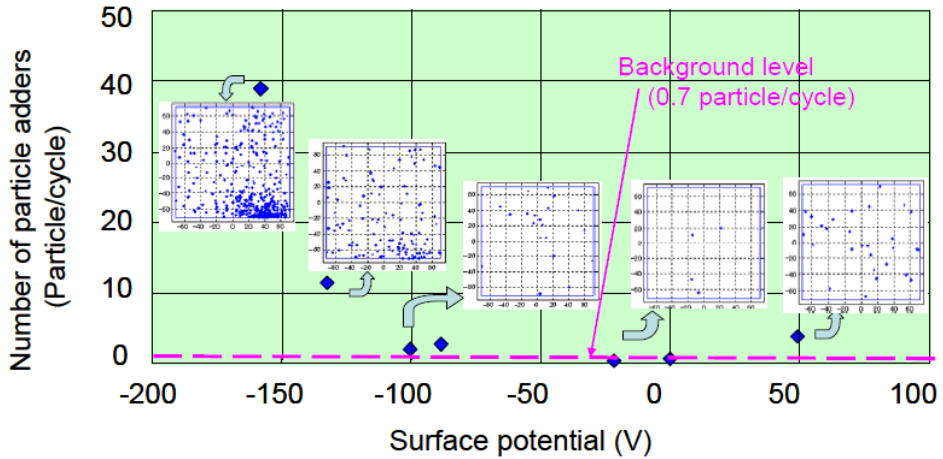


Figure 16: Particle pick-up as a function of reticle surface potential; from Amemiya⁵⁰.

Even while the EUV reticle pod is designed with electrostatics in mind (e.g. metal inner body to prevent ESD risks as present in DUV pod²⁴), the pod does not fully resolve this: frontside grounding has to be soft to prevent particle generation from hard grounding contact, so will make poor electrical contact through the insulating top oxide of the reticle frontside coating for low voltages²⁵. Although the backside pod cover itself is grounded, this does not make grounding contact to the reticle backside within the scanner vacuum system or the internal reticle library, but only makes contact when the EUV pod is locked at the load port to be removed from the scanner. It should be considered that this grounding is by soft contact to a potentially oxidized backside coating, so this contact might be poor in practice, and should not be relied upon for backside de-charging.

The issue of backside voltage excursions during unload can be remedied in two ways: 1) by creating a (negative) offset in the clamping scheme to shift the equilibrium of the EUV-plasma charging to (near) zero during the exposures, or 2) by supplying free charge carriers during the unload sequence to dynamically reduce the charge on the reticle as the voltage builds up.

A negative clamping offset has indeed been observed to result in lower backside voltage, with near-zero backside voltages during unload being achieved for an offset of

roughly -25 V, as shown in Figure 17, using ESVM. However, as can also be seen in Figure 17, for reasons of reticle chamfer and coating tolerances this offset would need to be calibrated per reticle to guarantee sufficiently low voltage at unload. The observed limit at $\sim 800\text{V}$ is most likely an artefact of the ex-situ ESVM measurements: ESVM can only be done outside of the scanner, after fully unloading the reticle, and voltages above $\sim 800\text{V}$ are expected to result in discharges during the unloading of the reticle to ambient conditions.

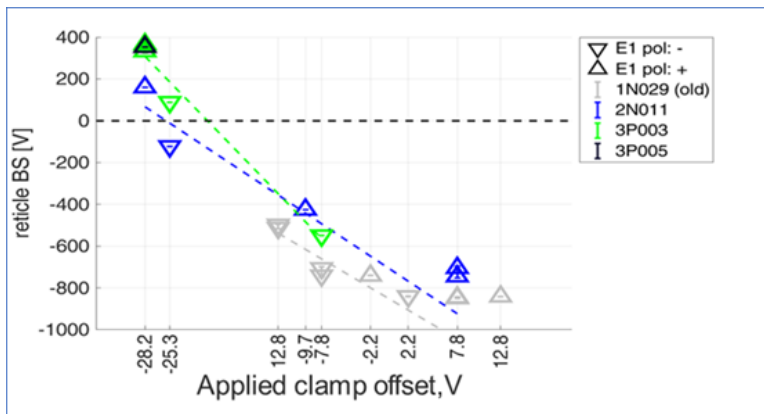


Figure 17: Reticle backside voltage as function of clamping offset; the colours denote different specimens of test reticles from two different suppliers.

An alternative solution is dynamic charge compensation during the unload sequence by creating a supply of free charge carriers; this will reduce the charge on the reticle as the voltage builds up and thus will maintain acceptably low voltage levels throughout the unloading sequence, to prevent any risk of discharge.

This could be achieved by a miniature plasma generator, such as proposed and developed by Hopwood²⁶; though such a device has been shown to work for hydrogen²⁷, the additional hardware is hard to retrofit into the existing scanner modules and reliably igniting the hydrogen plasma at $\sim 5\text{ Pa}$ is still considered a challenge. Figure 18 and Figure 19 show a successful prototype demonstration of such a device.

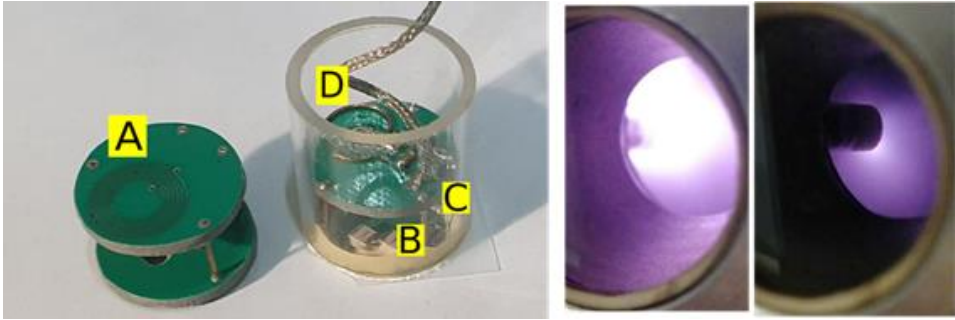


Figure 18: Left: prototype of miniature inductively-coupled plasma generator, with (A) inductive coil, (B) high-Q capacitors, (C) impedance matching and (D) RF current monitoring coil (prototype only). The diameter of the assembly is approximately 2 cm. Middle: ignition of discharge at 4.5 Pa hydrogen. Right: stable operation at 2W RF power and 4.5 Pa hydrogen. Images courtesy of ISAN.

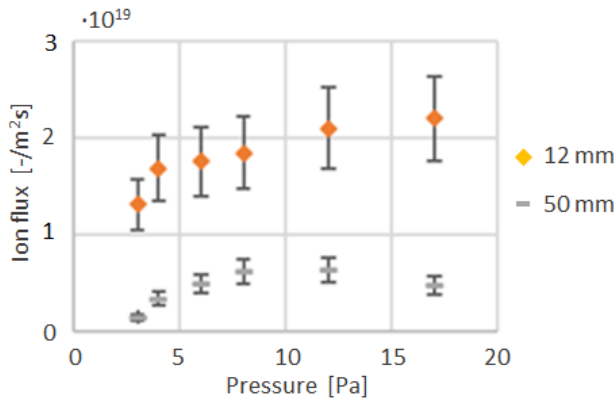


Figure 19: Measured ion flux of mini-ICP at pressures of 3, 6 and 12 Pa; measured at 1 and 5 cm distance. 20% error bars are indicative of measurement reproducibility. For reference: EUV plasma at RME is estimated to be $\sim 10^{17} \text{ m}^{-2} \text{ s}^{-1}$.

Dynamic charge compensation can also be achieved by turning on the EUV-induced plasma during the unload sequence, which has been termed “EUV@unload”²⁸. During the unload sequence the reticle is moved to a position next to the EUV beam, is placed onto a baseplate and subsequently lowered from the clamp. As the gap between reticle and clamp increases, the capacitance drops and the negative backside voltage builds up, attracting the ions from the EUV-plasma; simultaneously the opening gap allows the ions to reach the backside coating more easily to reduce the net charge. Even though the reticle is moved several cm’s away from the EUV beam during unload, the ions are

pulled towards the high negative potential on the reticle backside which develops as the reticle is moved away from the clamp. It should be noted that volume recombination is very low at this low pressure and ionization degree, so ions can travel a long distance if the directional motion in the electric field is stronger than diffusion to the walls. This is shown in Figure 20. Full scanner tests have confirmed that the EUV-induced plasma density is sufficient to counter the voltage amplification effectively, without delays or slowdowns in the unload sequence. Besides being relatively insensitive to reticle tolerances, this also has key benefits in using pre-existing hardware and having no ignition threshold.

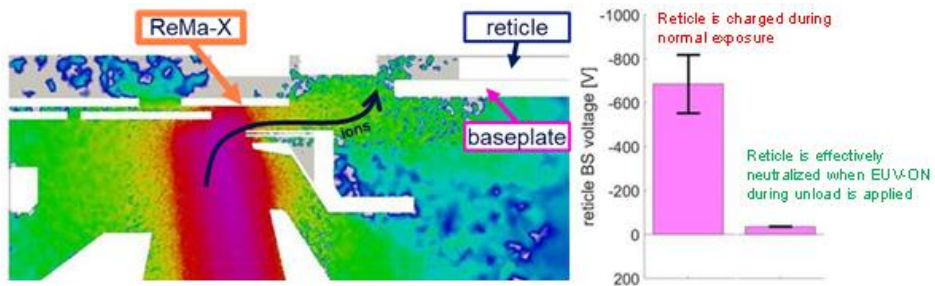


Figure 20: EUV-plasma neutralizes reticle backside during reticle unload, even with the EUV beam some cm's away. Left: reticle location with respect to EUV beam and modeled ion densities; Right: reticle backside voltage measured by ESVM, without and with EUV on during unload.

Customer data has shown that EUV@unload suppresses defectivity associated with electrostatic pick-up from the reticle pod baseplate, such as carbon-based fall-on particles, without deterioration of other particle types. Also, in-house testing on proto system (which had a known grounding issues) showed the effectiveness of EUV@unload to mitigate the resulting defectivity issue, as shown in Figure 21.

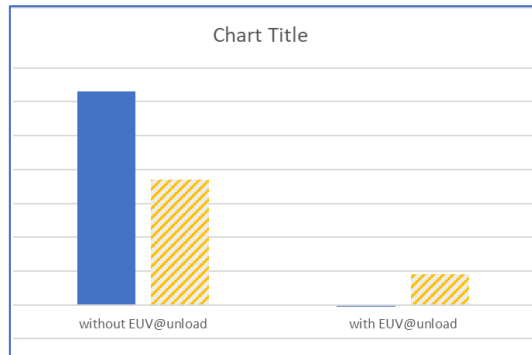


Figure 21: Effective mitigation of ESD-related particles (solid blue) by EUV@unload; ~4x improvement in non-ESD, or fall-on, particles (orange striped) cannot be attributed to EUV@unload but is likely due to flushing in between the two measurements.

Although current performance of the EUV@unload scheme is satisfactory, further improvements or accelerations are currently being investigated. One option could be to combine EUV@unload with clamp electrode biasing as outlined above, or alternatively to apply a negative bias voltage to the clamp during unloading to attract more ions from the EUV-plasma. For the long term, it is recommended to investigate grounding of both reticle surfaces during scanning; one option could be to ground the backside via hard electrical contact to the clamp and to create electrical connection between backside and frontside coatings.

4.4. Particle transport and reticle protection

Another electrostatic aspect of EUV is that the floating reticle surface will charge positively during the EUV pulse by photoelectric effect to ~20-40 V, and subsequently will be neutralized within ~5 μ s to zero volt by charge compensation from the EUV-induced plasma. This process repeats after 20 μ s with the next pulse. So on average the reticle will be charged ~1-2 V positively with respect to the surrounding grounded surfaces. As the reticle top layers (Ru cap and Ta absorber) are conductive and continuous, all of the reticle will take on this average positive potential, also the (large) part of the reticle that is away from the actual EUV-beam. Away from the EUV-beam, plasma density is too low to effectively shield the resulting electric field between reticle

and the grounded reticle masking blades at ~ 1 cm distance; the resulting average electric field close to the reticle will thus be in order of ~ 0.1 - 0.2 kV/m.

Free particles are preferentially charged negatively in and around the EUV-beam²⁹, although there might be a transient phase of positive charging by photo-electric effect³⁰. This results in an attractive electric force between reticle and particle. The charge of free particles inside the EUV beam will also show transient behavior with the EUV pulses, first briefly charging positively by photo-electric effect, then negatively due to the higher mobility of the plasma electrons, and subsequently (partly) neutralizing due to the ions, as described by Orbital Motion Limited (OML) theory³¹. Assuming thermal equilibrium, OML provides the steady state potential of the particle ϕ_p when the electron and ion fluxes are balanced:

$$\exp\left(\frac{\phi_p}{T_e}\right) = \sqrt{\frac{m_e T_i}{m_i T_e}} \left(1 - \frac{\phi_p}{T_i}\right) \quad (4.5)$$

With m_e, m_i and T_e, T_i the masses and temperatures (in eV) of the electrons and ions respectively. With the ions close to room temperature, the particle potential is mainly determined by the electron temperature. Approximating the particle by a sphere, the particle charge q_p follows from the potential via the capacitance of a sphere, and scales linearly with the particle diameter d_p ³².

$$q_p = 2\pi\epsilon_0 \cdot d_p \cdot \phi_p \quad (4.6)$$

In the transient EUV-induced plasma, no analytical equations exist for the potential or charge of a free particle, and PIC modeling is used to determine the evolution of particle charge over time. PIC simulations of the EUV-induced plasma in the region below the reticle show that micron-sized particles get a short positive charge, then flip to a negative charge, after which they reach an equilibrium between electron and ion currents, as illustrated in Figure 22; this process will be reset for every new pulse. For

submicron particles, reaching equilibrium between electrons and ions will typically take longer than the pulse interval, and negative particle charge will build up over multiple pulses until an equilibrium is reached between the photo-ionization and the electron currents, as illustrated in Figure 23. For an electron temperature of ~ 0.5 eV, the equilibrium particle charge is predicted to be roughly $\sim d_p$ [e], with d_p the particle diameter in nm.

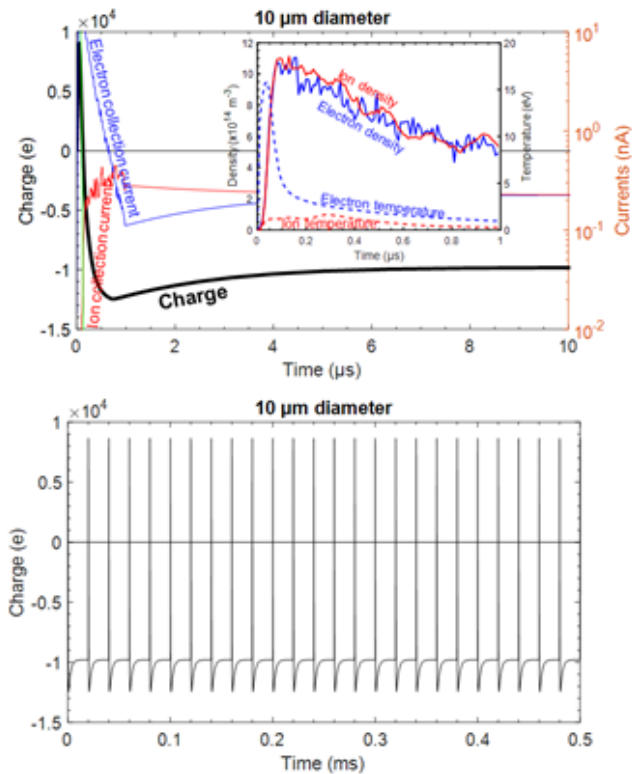


Figure 22: Left: PIC model of charging of a 10 μm particle in the EUV beam, showing fast transient positive photo-charging and subsequent negative charging (to ~ 1 e per nm); quasi steady-state charge (balanced electron and ion currents) is achieved within ~ 5 μs. The insert shows the electron and ion temperatures. Right: repeating charging pattern over multiple pulses.

Free particles next to the EUV beam will not experience the initial photo-electric effect, so particles of all sizes will charge negatively by the more mobile electrons towards will reach a quasi-steady-state equilibrium between electron and ion collection. Further

away from the beam, plasma density will drop and the charging will be much slower, but will still result in an average negative charge (again due to the more mobile electrons).

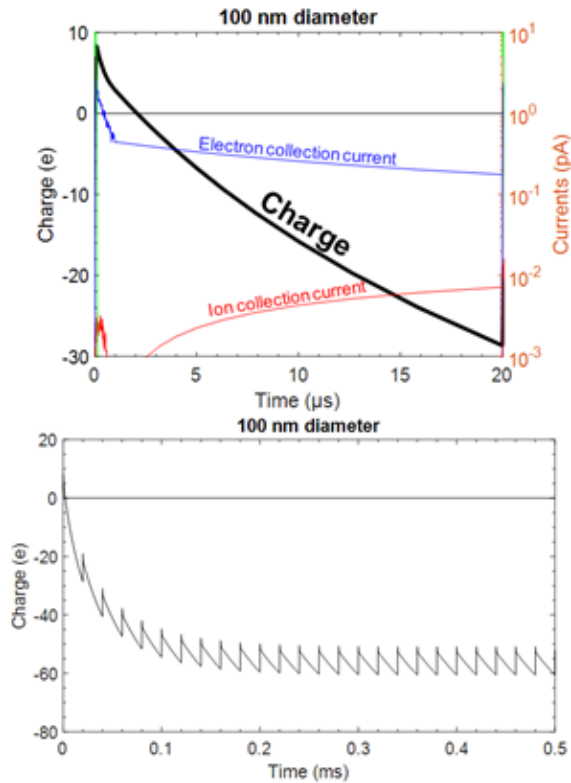


Figure 23: Left: PIC model of charging of a 100 nm particle in the EUV beam, showing fast transient positive photo-charging and subsequent negative charging. Right: increasing particle charge for over multiple pulses.

Extending the PIC simulations for particle charge with dynamic reticle potential and resulting electric fields yields an electric force on the particle near the reticle surface. Comparing the resulting electric force against the other forces that might work on a free-floating particle (gravitational force, neutral and ion drag forces, and for completeness, thermophoretic force (driven by temperature differences between the irradiated reticle surface and reticle-facing masking blades), it is clear that the dominant forces for submicron particles are the electric force and the neutral drag force, as illustrated by Figure 24.

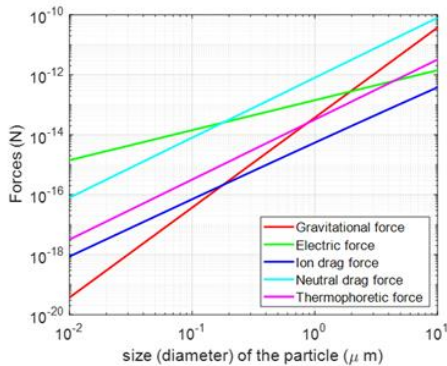


Figure 24: Volume force estimates for submicron particles in the gap between reticle and grounded reticle masking blades, for 250W Source and 5 Pa H₂.

Combining the vector force fields of electric and neutral drag forces, particle trajectories can be calculated, as shown in Figure 25. This allows to design the local flows and pressures such that no particles larger than a given critical size (50 nm in this example) will reach the reticle frontside surface. The most effective optimization parameter is pressure: increasing pressure will increase neutral drag force³³ and reduce the electric attraction force (as outlined above), but will come at expense of EUV transmission. Increasing flow in itself will increase neutral drag force and does not affect the electric force, but in practice flow and pressure are linked.

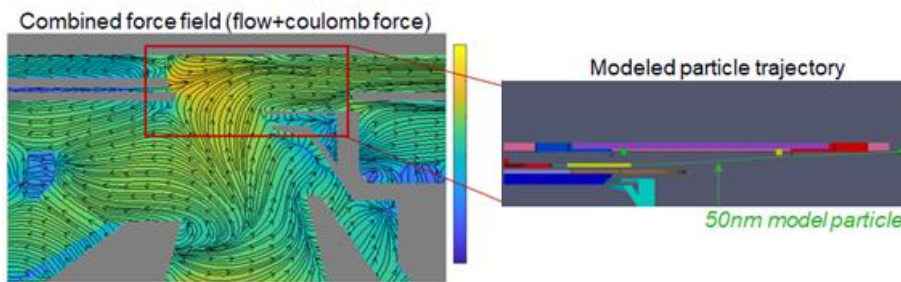


Figure 25: Left: Particle-in-Cell simulations of the force map for a 50-nm diameter particle in the reticle zone, just after the EUV pulse (180 ns). More yellow means higher force (more blue means lower); arrows indicate local direction of force. Right: modeled trajectory for a 50 nm test particle.

4.5. Conclusion

Understanding of the specific nature of the EUV-induced scanner plasma and the interaction of this plasma with surfaces and particles has improved significantly in the past years. This has allowed scanner design optimizations as well as targeted improvements in manufacturing and cleaning processes, for both plasma and related electrostatics aspects, to continue to drive down the corresponding contributors behind defectivity.

Analysis of plasma-assisted discharges has resulted in design guidelines for allowed voltages and pressures at various distances from the EUV-beam, to prevent discharges and improve the robustness of high-voltage electronics. Prevention of high reticle charging during unloading and handling, with the associated risk of discharges, removes a potential source of particles. These measures have brought particle contamination control of the EUV-scanner to a regime where customers have the freedom to operate without protective pellicle for high-volume manufacturing. For future EUV lithography systems, continued improvements in plasma models and understanding will ensure plasma-aware designs that will be compatible at increasing source powers and reducing critical particle sizes.

4.6. References

¹ T. van de Ven, “Ion fluxes towards surfaces exposed to EUV-induced plasmas”, PhD thesis Eindhoven University of Technology (2018)

² M. van der Velden et al, “Particle-in-cell Monte Carlo simulations of an extreme ultraviolet radiation driven plasma”, *Phys. Rev. E*, 73 (2006)

³ H. Kreuger, “Industrial high DC voltage: 1. Fields, 2. Breakdowns, 3. Tests”, Delft University Press, Delft (1995)

⁴ M. Naidu et al, “High Voltage Engineering”, p. 27, McGraw-Hill (1995)

⁵ R. Latham, “High voltage vacuum insulation”, Academic Press, London (1981)

-
- ⁶ P. Osmokrovic et al, “Mechanism of electrical breakdown left of Paschen minimum”, IEEE Transactions on Dielectrics and Electrical Insulation (1994)
- ⁷ E. Hastings et al, “Threshold voltage for arcing on negatively biased solar arrays”, Journal of Spacecraft and Rockets Vol. 27 (1990)
- ⁸ R. Latham, “High Voltage Vacuum Insulation, a new perspective”, Author House, Bloomington (2006)
- ⁹ I. Korolov et al, “Breakdown in hydrogen and deuterium gases in static and radio-frequency fields”, Physics of Plasmas (2015)
- ¹⁰ Z. Li et al, “Surface flashover of nanodielectrics with varying electrode architectures in partial vacuum under DC and kHz pulsed fields”, IPMHVC 2012 (2012)
- ¹¹ D. Cooper et al, “Electrostatic removal of particle singlets and doublets from conductive surfaces”, Aerosol Science and Technology (1990)
- ¹² R. van der Wilk, ASML internal report (2018)
- ¹³ H. Miller, “Flashover of insulators in vacuum: review of the phenomena and techniques to improved holdoff voltage”, IEEE transactions on electrical insulation 28 (1993)
- ¹⁴ K. Asano et al, “Fundamental Study of an Electrostatic Chuck for Silicon Wafer Handling”, Microelectronic Engineering, Vol. 38 (2002)
- ¹⁵ B. Oni, “Observations of voltage breakdown in ultra-low pressure environments under varied voltage and frequency conditions”, Journal on Electrical Engineering 12 (2019)
- ¹⁶ S. Baalrud et al, “Interaction of biased electrodes and plasmas: sheaths, double layers, and fireballs”, Plasma Sources Sci. Technol. (2020)
- ¹⁷ J. Holtzhausen et al, “High Voltage Engineering Practice and Theory”, Stellenbosch, Western Cape (2014)
- ¹⁸ J.S. Yoon et al, “Cross sections for electron collisions with hydrogen molecules”, Journal of Physical and Chemical Reference Data (2008)
- ¹⁹ P. McLellan, https://community.cadence.com/cadence_blogs_8/b/breakfast-bytes/posts/iedm-sc-euv
- ²⁰ K. Ota et al, “Evaluation results of a new EUV reticle pod having reticle grounding paths”, EUVL Symposium (2010)
- ²¹ A. van den Biggelaar, “Modeling of dynamic effects in high-voltage electrostatic clamps”, MSc thesis TU Eindhoven (2016)
- ²² J. van Duivenbode, internal ASML report (2018)

-
- ²³ M. Amemiya et al, “Experimental study of particle-free mask handling”, Proc. of SPIE 7271 (2009)
- ²⁴ G. Rider, “A critique of the approach to controlling electrostatic risk in semiconductor production and identification of a potential risk from the use of equipotential bonding”, AIMS Electronics and Electrical Engineering (2019)
- ²⁵ K. Ota et al, “Evaluation results of a new EUV reticle pod having reticle grounding paths”, Proc. of SPIE Vol. 7969 (2011)
- ²⁶ J. Hopwood et al, “Fabrication and characterization of a micromachined 5 mm inductively coupled plasma generator”, J. Vac. Sc. & Techn. B (2000)
- ²⁷ E. Osorio Oliveros, internal ASML report (2019)
- ²⁸ M. van de Kerkhof, Worldwide Patent No. WO2019197128A2 (2019)
- ²⁹ A. Sickafoose et al, “Experimental investigations on photoelectric and triboelectric charging of dust”, Journal of Geophysical Research: Space Physics (2001)
- ³⁰ S. Frazier et al, “Charging Behavior of Dust Aggregates in a Cosmic Plasma Environment”, Lunar and Planetary Science Conference No. 1719 (2013)
- ³¹ H. Mott-Smith et al, “The Theory of Collectors in Gaseous Discharges”, Phys. Rev. 28 (1926)
- ³² L. Heijmans, “Quantifying Plasma Particle Lofting”, PhD thesis Eindhoven University of Technology (2017)
- ³³ X. Chen, “The drag force acting on a spherical non-evaporating or evaporating particle immersed into a rarefied plasma flow”, J. Phys. D Appl. Phys. 29 (1996)

5

5. Charging of particles on surfaces and particle release

This chapter is based on following publications:

- *Mark van de Kerkhof, Andrei Yakunin, Vladimir Kvon, Andrey Nikipelov, Dmitry Astakhov, Pavel Krainov, Vadim Banine, "EUV-induced Hydrogen Plasma and Particle Release", Radiation Effects and Defects in Solids (submitted)*
- *Pavel Krainov, Vladimir Ivanov, Dmitry. Astakhov, Vladimir Medvedev, Vladimir Kvon, Andrei Yakunin, Mark van de Kerkhof, "Dielectric particle lofting from dielectric substrate exposed to low-energy electron beam", Plasma Sources Science and Technology (2020)*

5.1. Introduction

Particles and particle release are a crucial aspect of EUV system design, driven by extremely tight requirements on the one hand and extreme difficulties in controlling nanoparticles on the other¹. In terms of particle contamination control, Van der Waals adhesion forces will be dominant for submicron particles on a surface in (near-) vacuum. As discussed in chapter 1, the force between a spherical particle and a flat surface is given by²:

$$F_{vdW} = C_r \cdot \frac{A_H \cdot r_p}{6 \cdot z_0^2} \quad (5.1)$$

This correction factor C_r may be in a wide range of $C_r=0.001-1$, due to particle morphology, asperities and surface roughness³. The effective adhesion force may thus be some orders of magnitude smaller. The typical Van der Waals force for a 100 nm particle will be in a range of 10^{-12} - 10^{-9} N.

This section will explore particle release by charging of the particle and the surface by the EUV-induced plasma. Besides charge-driven release described here, it should be noted that the hydrogen plasma may also remove organic particles by etching, as will be described in chapter 6.

5.2. EUV generation and EUV-induced plasma

The 92 eV EUV photons will lead to photo-ionization of the hydrogen background gas, creating a plasma. As outlined in section 3, atomic and molecular hydrogen ions will be formed, and energetic photoelectrons of up to 76 eV. The pulsed EUV-induced plasma will be strongly transient and will typically not be in local thermal equilibrium (LTE), and the electron energy distribution will not be Maxwellian. This in turn means that strictly speaking many classical plasma equations will not or not always apply.

Close to a mirror or reticle, which is irradiated by EUV, the photoelectric effect will result in emission of electrons, and the irradiated surface will tend to briefly charge positively, before being neutralized by the plasma.

In a confined plasma geometry, the energetic photoelectrons of 76 eV will result in secondary electron emission when they strike the plasma-facing surfaces. For typical construction materials such as stainless steel and aluminum, the secondary electron yield (SEY) has been measured to be above unity for these incident electron energies (see section 3.3.5). This $SEY > 1$ for 76 eV is not generally predicted by the universal curve⁴, which was set up with a focus on higher energy electrons, and it is advisable to use SEY-data that was measured specifically in this regime.

The secondary electrons will have lower energies, and may be approximated by a Maxwellian distribution with $T_e \approx 3$ eV, but with a more pronounced high-energy tail of up to the energy of the incident electron. As the plasma electrons cool down quickly by collisions to below 30 eV, the SEY will drop below unity, and the wall will start to charge negatively.

5.3. Particle charging and release by plasma

Electrostatic removal or lofting of particles is well-known for conducting particles on conducting surfaces. The particle will form a protrusion on the surface which will result in charge concentration on the particle in case of an electrical field, and a resulting repelling force⁵. For submicron particles, electrical fields in order of 10-100 MV/m are needed to release particles⁶, which is some orders of magnitude higher than will occur in the EUV-induced plasma sheath⁷.

In case of a pulsed plasma, a particle on a plasma-facing surface will acquire transient charges similarly as the surface by the electron and ion fluxes from the plasma, which will result in a transient electrostatic repelling force on the particle. In contrast to a dusty surface with many particles which may influence the plasma sheath significantly, an isolated particle will be a negligible perturbation to the plasma itself and the plasma

equations and models of previous sections will hold⁸. Particle cleaning by plasma was first observed in 1992 by Sheridan⁹, in which it was noted that the charging of a particle on a surface is stronger than particle charging in the free volume of the plasma, and also that fast electrons are needed for release. These experimental findings were confirmed and elaborated on by Flanagan and Goree¹⁰.

As charging by electrons and ions (and photons) are discrete in nature, and charge transport over the oxide surface layers of most materials might be slow, stochastics can play an important role in charging and release of nano-scale particles by plasma. As discussed above, the combination of pulsed transient high-energy photoelectrons on top of a steady-state cold plasma will result in a significantly enhanced sheath electrical field (sheath potential increases while sheath width does not). Using the bi-Maxwellian approach outlined in section 3.3.1 and following Sheridan, the resulting stochastic release force will depend strongly on the photoelectron energy and weakly on the background plasma density and temperature and particle size¹¹:

$$F_{rel,avg} = Q_{avg} \cdot E_{wall} \cong C \cdot r_p^{1/2} \cdot n_e^{1/2} \cdot T_{e2}^{3/2} \cdot T_{e1}^{-1/2} \quad (5.2)$$

With r_p the particle radius, and $C \cong 3 \cdot 10^{-18}$ Nm/eV for the EUV case with primary photoelectrons of $T_{e2} \cong 20$ eV, and background plasma with $T_{e1} = 0.1$ eV and $n_e \cong 10^{15}$ m⁻³. For a 100 nm particle, this yields an average release force of $F_{rel,avg} \sim 10^{-11}$ N, which is in the lower range of the typical adhesion force of $\sim 10^{-11}$ - 10^{-9} N. The stochastics of charging however may yield charges of several times the average charge, so a stochastic force distribution with a tail of $\sim 10^{-10}$ N may occur. The tail of a stochastic distribution is unlikely, and in this case will fall-off faster than a Gaussian distribution because of the mutual repulsion of the discrete electrons (so events are not strictly independent). The partial overlap of the release and adhesion force distributions in combination with the above stochastic considerations will give rise to ‘black-swan’ particle release events with low but finite probability per pulse. One needs to keep in mind though that given the EUV pulse frequency of 50 kHz, or $\sim 10^9$ pulses per day, also such ‘black-swan’ events may become significant. The above holds for a classical sheath, which may not be the case for most construction

materials, which typically will have $SEY > 1$ at 76 eV and will thus form an inverse sheath or space-charge limited sheath. In that case, the classical sheath will only develop when the electron energy drops below the material-dependent crossover energy (of ~ 30 eV¹²). As a first approximation, applying equation 5.2 yields a reduction in the effective release force by a factor of $\sim (76/30)^{3/2} \cong 4x$. A more detailed force analysis is beyond analytical descriptions and requires PIC modeling.

The case for electron (or photon) energies above the crossover energy of the substrate was investigated by Wang¹³, showing that a secondary electron yield (SEY) of the substrate above unity, or $Y_s > 1$, may lead to a significantly higher particle release force for insulating materials (an oxidized toplayer will be sufficient insulation). This is explained by the accumulation of secondary electrons from the substrate in the cavity between the particle and the substrate, as illustrated in Figure 1. The substrate itself will on average achieve a slight positive potential of ~ 1 -2 V, to be in equilibrium with the escaping low-energy secondary electrons; however, the underside of the particle and the surface in the shadow of the particle may attain a negative potential of several tens of volts (depending on the crossover energy of the particle at which $SEY=1$)¹⁴. This can result in a high repulsive force due to the nm-scale separation in this cavity, and subsequent particle release.

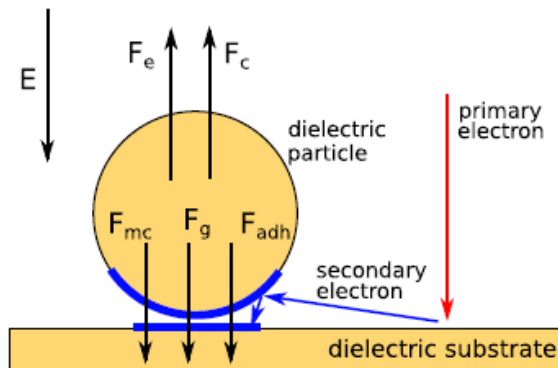


Figure 1: Primary and secondary electron flow, subsequent charging underneath particle and resulting force balance. Forces: F_g gravity, F_{adh} adhesion force, F_e the interaction with the sheath field, F_c the coulomb repulsion in the cavity, and F_{mc} the mirror charge force.

The condition $Y_s > 1$ depends on the substrate material and its surface condition, and is in order of ~ 50 eV for most (metal) oxides and dielectrics¹⁵, and somewhat higher for most metals. For the EUV-induced photoelectrons of 76 eV, this condition is typically satisfied for dielectric surfaces and oxidized metals. A secondary condition is that the SEY of the particle is lower than the SEY of the substrate so a significant portion of the secondary electrons will be re-emitted by the particle to the substrate underneath the particle to form two mutually repelling negative charge patches on both particle and surface; in other words $Y_p < Y_s$. This is illustrated in Figure 2 for examples of particle-substrate combinations of SiO₂-on-NaCl and NaCl-on-SiO₂ (with SiO₂ assumed to have SEY=1.2 and NaCl to have SEY=0.8 in the range around 76 eV). The overall negative charge of the particle may be further increased if the particle itself has a SEY well below unity for 76 eV electrons, as in practice might be the case for very irregular or rough particles, or for particles with a hydrocarbon adsorbate layer¹⁶. This release force is mitigated by mirror charge attraction to the substrate, depending on the substrate permittivity ϵ ¹⁷:

$$F_{rel} \cong \frac{Q^2}{2\pi\epsilon_0 r^2} \cdot \left(1 - \frac{r}{\sqrt{r_p^2 + r^2}}\right) - \frac{1}{4\pi\epsilon_0} \frac{\epsilon - 1}{\epsilon + 1} \frac{Q^2}{(2r)^2} \quad (5.3)$$

Where the first term is the Coulomb repulsion between the particle with radius r and the charge patch underneath, and the second term is the attractive force from the mirror charge, in the approximation that for submicron particles the charge is evenly distributed between particle and surface patch (of size $r_p \approx 1.5 \cdot r$), and that the charge on the particle may be approximated by a point charge at the center of the particle¹⁷. For a conductive surface ($\epsilon = \infty$) this may be approximated by:

$$F_{rel} \cong \frac{Q^2}{2\pi\epsilon_0 r^2} \cdot \left(1 - \frac{r}{\sqrt{r_p^2 + r^2}}\right) - \frac{1}{4\pi\epsilon_0} \frac{Q^2}{(2r)^2} \cong \frac{Q^2}{6\pi\epsilon_0 r^2} \quad (5.4)$$

For conductors with a dielectric toplayer (oxide or coating), the mirror charge term will become smaller by correction with the thickness of the dielectric ($r \rightarrow r + d_{dielec}$), resulting in a larger net repulsive force.

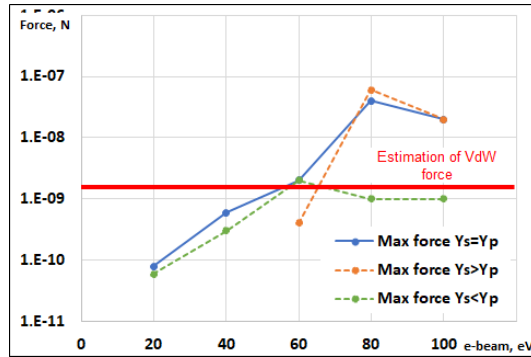


Figure 2: maximum release force by fast electrons, for substrate-to-particle SEY ratio of 1 (blue), 1.5 (orange) and 0.7 (green).

The accumulated charge in the cavity will depend on the capacitance of the particle and the accumulated voltage in the cavity: $Q = C \cdot V$. The capacitance of the particle may be approximated by $C \cong 4\pi\epsilon_0 r$ (ignoring possible deviations from spherical and the non-uniform charge distribution over the surface). The cavity voltage will be driven by the secondary electron energy distribution from the substrate and the crossover energy of the particle for SEY=1, and may be expected to be in range from 10-30 eV, depending on particle material, roughness and contamination. For a 100 nm particle, this would yield a release force in order of 10^{-9} - 10^{-8} N, which is similar to or higher than the adhesion force, as shown in Figure 2.

The above analysis focused on energetic electrons in vacuum and did not include plasma yet. Adding a low-pressure plasma to the energetic electrons will modify the charge patches in the particle-substrate cavity by low-energy plasma electrons and ions¹⁸, as shown in Figure 3. This has been modeled using PIC model, showing that over the pulses the cavity will first charge negatively by the secondary electrons and will subsequently attract ions, resulting in positive and negative patches; in the next pulse

this cycle will repeat. At low pressures, ions may accumulate in the deepest part of the cavity, thus contributing to the repulsion force.

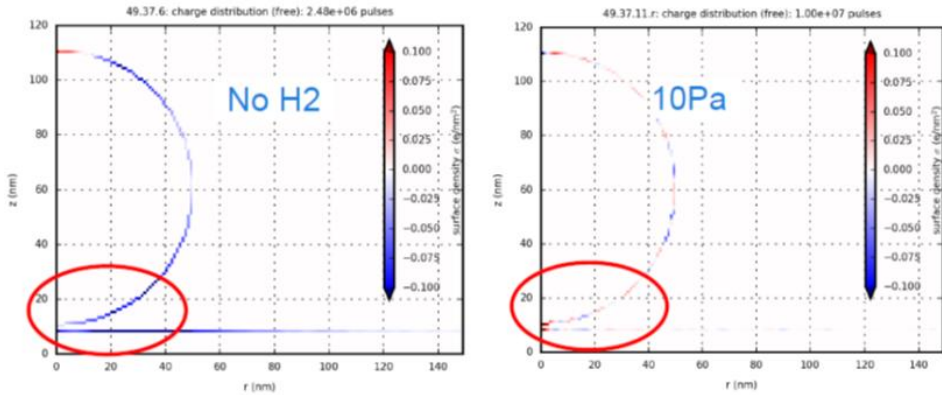


Figure 3: Modelled charge patches on particle lying on a surface, without and with hydrogen plasma. Blue areas represent local negative charge patches and red areas represent positive charge patches.

At higher pressures the low-energy electrons and ions will neutralize charge patches on and beneath the particle; this reduces the release force at higher pressure, as illustrated in Figure 4. For dielectric materials or thick dielectric coatings the electric release force is predicted to be comparable to or exceed the range of possible Van der Waals forces for submicron particles; for a thin dielectric or natural oxide, the release force will be reduced by mirror charge effect but will still be comparable to the Van der Waals force. For a conductive metal or conductive oxide surface, charge patches will not occur or only on the particle, so this release mechanism will be much smaller. It is therefore advised to use conductive metal surfaces in areas that are critical for defectivity¹⁹.

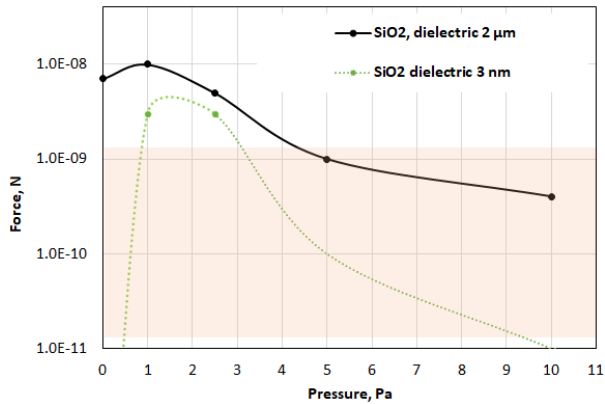


Figure 4: Modelled release force as function of pressure for 100 nm particle at two dielectric skin thicknesses. Estimated range of Van der Waals adhesion force in orange.

The range of energetic electrons will be more limited at higher pressure, so the surface area around the beam where particle may be released by this mechanism will be more confined. The pressure dependence of the release force might be explored to suppress particle release by increasing pressure within the scanner RME. Or alternatively, a temporary reduction of pressure might be considered to achieve in-situ plasma cleaning by inducing accelerated particle release.

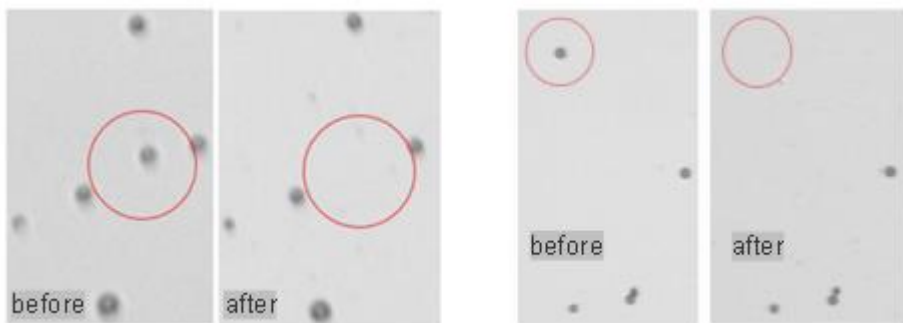


Figure 5: Experimental confirmation of release of 5 μm SiO₂ particles on Si wafer with natural oxide layer; confirming finite release probability.

This mechanism may thus lead to particle release, as indeed has been measured in vacuum using an electron beam extracted from a pulsed plasma, as shown in Figure 5. In this experiment 3000 pulses were fired with cumulative dose of 10¹⁴ electrons per

cm², at total accelerating voltage of 300 V. Tentative conclusion is that release probability is low but finite.

5.4. Conclusion

The 92 eV photons and energetic photoelectrons of up to 76 eV may release particles by electric forces. It is recommended that plasma-facing materials should have a conductive surface to minimize stochastic release force excursions, e.g. by using sufficiently noble metals (such as ruthenium) or metals with a conductive oxide (such as molybdenum).

The plasma-facing surfaces should preferably have a low secondary electron yield to minimize cavity charging underneath the particle.

A higher hydrogen pressure might also help to neutralize patch charges and reduce stochastic peaks in electric repulsion. This should be balanced with other requirements like molecular contamination and transmission.

5.5. References

¹ M. van de Kerkhof et al, “Advanced particle contamination control in EUV scanners”, Proc. Of SPIE Vol. 10957 (2019)

² J. Israelachvili, “Intermolecular and surface forces”, 3rd edition, Academic Press (2011)

³ M. Goetzinger et al, “Particle Adhesion Force Distributions on Rough Surfaces”, Langmuir Vol. 20 (2004)

⁴ Y. Lin et al, “A New Examination of Secondary Electron Yield Data, Surface and Interface Analysis” (2005)

⁵ H. Saeki et al, “New electrostatic dust collector for use in vacuum systems”, JVST A (1989)

⁶ L. Scaccabarozzi et al, “Particle cleaning of EUV reticles”, Journal of Adhesion Science and Technology (2009)

-
- ⁷ M. van de Kerkhof et al, “Understanding EUV-induced plasma and application to particle contamination control in EUV scanners”, Proc. of SPIE Vol. 11323 (2020)
- ⁸ L. Heijmans et al, “Dust on a surface in a plasma: A charge simulation”, Physics of Plasmas (2016)
- ⁹ T. Sheridan et al, “Observation of dust shedding from material bodies in a plasma”, J. Geophys. Res. 97 (1992)
- ¹⁰ T. Flanagan et al, "Dust release from surfaces exposed to plasma," Physics of Plasmas Vol. 13 (2006)
- ¹¹ T. Sheridan, “Charge fluctuations for particles on a surface exposed to plasma”, Applied Physics Letters (2011)
- ¹² N. Balcon et al, “Secondary electron emission on space materials: Evaluation of the total secondary electron yield from surface potential measurements”, IEEE Transactions on Plasma Science (2011)
- ¹³ X. Wang et al, “Dust charging and transport on airless planetary bodies”, Geophysical Research Letters (2016)
- ¹⁴ J. Schwan, “Electrostatic mechanics of dust lofting and transport on airless planetary bodies”, PhD Thesis, University of Colorado, Boulder, Colorado (2017)
- ¹⁵ H. Bruining, “Physics and Applications of Secondary Electron Emission”, Pergamon Ltd, London (1954)
- ¹⁶ D. Ruzic, et al, “Secondary electron yields of carbon-coated and polished stainless steel”, Journal of Vacuum Science and Technology (1982)
- ¹⁷ P. Krainov et al, “Dielectric particle lofting from dielectric substrate exposed to low-energy electron beam”, Plasma Sources Science and Technology (2020)
- ¹⁸ P. Krainov, “Particle lofting from substrate exposed to plasma and electron beam”, arXiv preprint arXiv:2011.09204 (2020)
- ¹⁹ M. van de Kerkhof et al, “Particulate and molecular contamination control in EUV-induced H₂-plasma in EUV lithographic scanner”, Proc. of SPIE Vol. 11489 (2020)

6

6. Plasma-material interaction and particle release

This chapter is based on following publications:

- *Mark van de Kerkhof, Andrei Yakunin, Vladimir Kvon, Andrey Nikipelov, Dmitry Astakhov, Pavel Krainov, Vadim Banine "EUV-induced Hydrogen Plasma and Particle Release", Radiation Effects and Defects in Solids (submitted)*

6.1. Introduction

The EUV-induced hydrogen plasma is a deliberate feature of EUV lithography scanner systems, that is vital in preventing mirror oxidation and continuously cleaning hydrocarbon contamination from the mirror surfaces. This principle has gradually been

perfected in past 25 years of EUV development. However, besides the mirrors, also the interaction of this aggressive plasma environment with construction and functional surfaces close to the EUV beam must be understood to secure best yield in terms of particle contamination control and highest long-term mirror reflectivity.

Also, the aspects of beam and plasma confinement, and of pressure, will be considered, as these may change the characteristics of the hydrogen plasma in terms of molecular and particulate contamination.

In terms of particle contamination control, Van der Waals adhesion forces will be dominant for submicron particles on a surface in (near-) vacuum. The force between a spherical particle and a flat surface is given by¹:

$$F_{vdW} = C_r \cdot \frac{A_H \cdot r_p}{6 \cdot z_0^2} \quad (6.1)$$

With r_p the particle radius, A_H the Hamaker constant (which for most material combinations is $A_H \cong 10^{-19}$ J), z_0 the minimum separation between surface and particle ($z_0 \cong 0.4$ nm), and C_r an empirical correction factor for a real particle. This correction factor may be in a wide range of $C_r=0.001-1$, due to particle morphology, asperities and surface roughness². The effective adhesion force may thus be some orders of magnitude smaller. The typical Van der Waals force for a 100 nm particle will thus be in a range of 10^{-12} - 10^{-9} N.

This section will explore how the plasma environment can lead to reduced adhesion and particle release³: by reduction of the adhesion force by etching and roughening, and by blistering or fragmentation of the particle.

6.2. EUV generation and EUV-induced plasma

The 92 eV EUV photons will lead to photo-ionization of the hydrogen background gas, creating a plasma. As outlined in section 3, both H^+ , H_2^+ and H-radicals will be formed,

and energetic photoelectrons of up to 76 eV. The H_2^+ will be quickly converted to H_3^+ , which will be the dominant ion after $\sim 0.5 \mu s^4$. The pulsed EUV-induced plasma will be strongly transient and will typically not be in local thermal equilibrium (LTE), and the electron energy distribution will not be Maxwellian⁵. This in turn means that strictly speaking many classical plasma equations will not or not always apply. Indeed, during and after the EUV pulse explicit kinetic equations must be used for the electrons and ions, but in the afterglow between the pulses the quasi-steady-state plasma can be approximated well enough in classical terms.

Close to a mirror or reticle, which is irradiated by EUV, photoelectric effect will result in emission of electrons by photoelectric effect⁶, and the irradiated surface will tend to charge positively. In the low-pressure regime around 5 Pa, the flux of surface electrons will be larger than the flux from gas ionization, and no sheath will form during the EUV pulse. After the EUV pulse the flux of surface electrons stops and the plasma sheath will develop. Besides by EUV, this effect may also be driven by the out-of-band and UV often accompanying the EUV pulse, which may persist for 0.2-0.3 μs after the EUV pulse.

Similarly, in a confined plasma geometry, the energetic photoelectrons of 76 eV will result in secondary electron emission with a yield above unity when they strike the plasma-facing surfaces. Again, this results in frustrated formation of a sheath, until the photoelectrons cool down by collisions to below ~ 30 eV.

As shown in Figure 1, the resulting kinetic ion energy peaks in a confined plasma are limited to < 10 eV, significantly lower than the 76 eV which would have been expected from the photoelectron energy; in between the pulses the majority of ions will have a kinetic energy of ~ 2 eV.

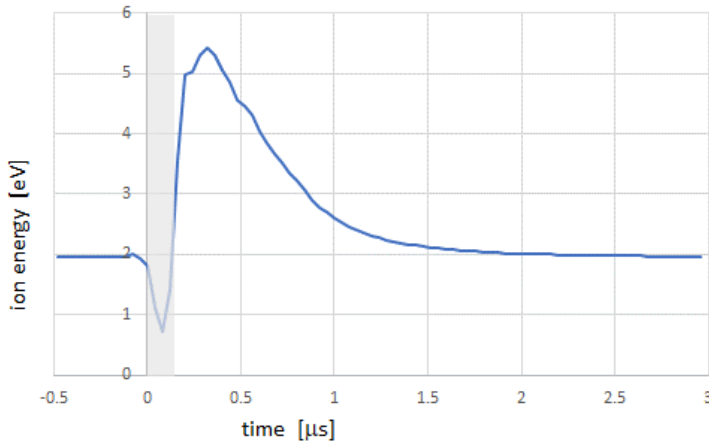


Figure 1: RFEA measurement of ion energy next to the EUV beam at 5 Pa; RFEA blind time of 0.2 μs is marked in gray.

The LPP EUV Source operates at a frequency of 50 kHz, or cycle time of 20 μs, with an EUV pulse length of <100 ns. As the plasma does not extinguish completely within 20 μs, there will be pulse-by-pulse build-up towards a quasi-steady-state plasma, with repeating transient peaks every 20 μs. For a confined plasma diffusion losses to the surface will limit the build-up and the plasma properties will to a large degree be determined by the repeating transient peaks.

Close to the beam, the H-radicals may have a high energy of 1 eV or above from their various production processes, so these may be more reactive than expected from literature values based on colder radical sources. Confinement leads to generation of additional radicals at the walls and an increase of the ratio of radicals to ions, to in order of 50x more radicals (see section 3.3.10).

The plasma parameters as relevant for the confined scanner RME environment are summarized in table 1.

Table 1: Summary of EUV-induced plasma parameters in RME

Parameter	Value
Incident EUV power	50 W

Pulse frequency/interval	50 kHz / 20 μ s
Plasma electron/ion density	$\sim 10^{15} \text{ m}^{-3}$
Ionization degree	$\sim 10^{-4} \%$
Ion flux	$\sim 10^{17} \text{ m}^{-2}\text{s}^{-1}$
Ion energy	$\sim 2\text{-}10 \text{ eV}$
Radical flux	$\sim 10^{19} \text{ m}^{-2}\text{s}^{-1}$

6.3. *Plasma-material interaction and effect on particle adhesion*

6.3.1. Surface erosion and sputtering

Based on the relative impact of ions and radicals, surface erosion by plasma can be broadly differentiated into three classes: plasma-enhanced chemistry, chemical sputtering or reactive ion etching (RIE), and physical sputtering. In plasma-enhanced chemistry the radicals dominate; this process is non-directional, and speed varies according to the activation energy involved and temperature. In chemical sputtering, the ions accelerate the chemical reactions of the radicals; this process is directional and relatively fast. In physical sputtering, energetic ions directly remove target atoms; this process is relatively slow but highly directional (along the electrical field lines near the surface). In addition, hydrogen radicals and ions may promote diffusion, segregation in metals and alloys and agglomeration in thin film coatings.

Light ions like hydrogen are typically not considered a risk for physical sputtering due to their limited energy transfer efficiency γ_E in a head-on collision:

$$\gamma_E = \frac{4 m_2 m_1}{(m_2 + m_1)^2} \quad (6.2)$$

With mass m_1 for the incident ion and mass m_2 for the target atom. Physical sputtering may occur if the ion energy transferred to a surface or target atom exceeds the binding

energy of that atom, in a recoil collision cascade. This gives an energy threshold for physical sputtering, assuming two head-on collisions of the lighter incident ion. The Yamamura sputtering model provides a generic approximation for the threshold energy U_{thr} for light ions incident on heavier target atoms⁷:

$$U_{thr} = \frac{1 + 5.7(m_1/m_2)}{\gamma_E} \cdot U_b \quad (6.3)$$

With U_b the binding energy (in eV) and γ_E the energy transfer efficiency. The binding energy may be taken to be equal to the heat of sublimation and scales with macroscopic properties like melting point⁸.

Besides sputtering with loss of target atoms, a second damage mechanism is displacement of target atoms which may lead to segregation and roughening of the surface layers. The energy required to displace a target atom U_{dis} may be taken to be roughly the same as the sputter threshold energy U_{thr} , but in a hydrogen environment this may be reduced by absorbed interstitial hydrogen. A third damage mechanism is breaking of atomic bonds in the target surface at relatively low incident ion energies of few eV, resulting in promotion of hydride formation in a hydrogen environment⁹.

For molecular ions like H_2 , the kinetic energy is distributed over the constituent atoms. For low energies and sufficiently stiff intramolecular bonds, it was found by Yao that the molecular ion can be treated as an atomic ion with mass equal to the combined mass of the molecule, since the interaction time of the collision is longer than the vibrational period of the molecule (it is assumed that the ion neutralizes before entering the surface)¹⁰. This effect was confirmed by Dobes¹¹ and Phadke¹² for N_2 sputtering of Ru. While Yao investigated N_2 and O_2 , it may be inferred that this also holds for H_2 , since hydrogen has an even higher vibrational frequency¹³. Thus, at low energies molecular H_2^+ ions should behave like deuterium (D^+), which increases the energy transfer efficiency and reduces the sputtering threshold. This was experimentally confirmed by Vergara using deuterium ion beams on carbon¹⁴, as shown in Figure 2.

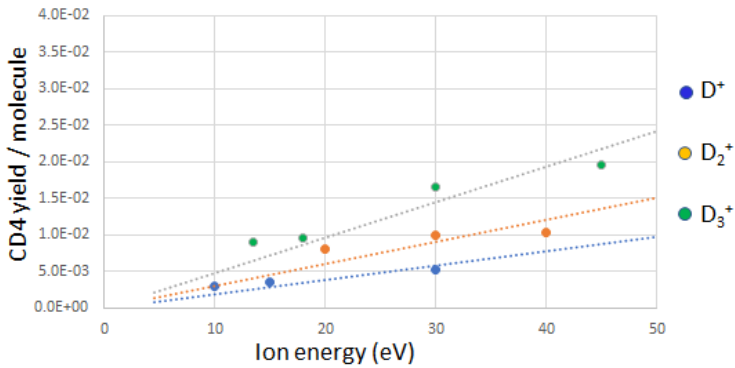


Figure 2: Methane yield per molecular deuterium ion incident on carbon. Based on data from Vergara¹⁴.

This correction may be quite significant, reducing the threshold energy of common construction materials under incident H_3^+ , to e.g. 15 eV for Al and 21 eV for Si (as compared to 30 and 42 eV respectively for H^+). In the scanner plasma, the H_3^+ ions will have a peak energy of <10 eV, which means physical sputtering of even light materials such as Al and Si may be excluded; in practice both materials will also have a protective oxide with a higher binding energy.

6.3.2. Chemical sputtering

At energies well below the physical sputtering energy threshold, chemical sputtering may take place for metals forming volatile hydrides. Taking the latent energy of 2.3 eV of the radical into consideration, hydride formation by radicals is exothermic for all metals, and the energy transferred by the incident ions will create excited states that lower the activation energy barrier; this may increase reaction rates by some orders of magnitude. Aluminum (Al)^{15,16} and silicon (Si)¹⁷ and carbon (C) are the most important examples of this mechanism in hydrogen plasma. It is noteworthy that in the case of tin (Sn), chemical sputtering by hydrogen plasma is actively used to continuously clean Sn debris off the Source collector optics during operation^{18,19}.

Perhaps surprisingly, the activation energy supplied by the hydrogen ions (and/or photons and energetic electrons) may lead to oxidation rather than reduction in

presence of adsorbed H₂O or O₂, in cases where the delta Gibbs energy for oxidation is larger than for hydride formation; this has been observed in base metals such as stainless steel, and in silicon²⁰. Besides thermodynamic considerations, also the reaction kinetics must be considered, and high adsorbate concentration and/or high mobility of the H₂O or O₂ with respect to the hydrogen radical flux may result in net oxidation.

Additional care should be taken for (chemical) sputtering of even trace amounts of heavier ions such as N₂⁺ (28 amu), in combination with hydrogen radicals, in view of their significantly higher mass and correspondingly higher energy transfer efficiency.

6.3.3. Miscellaneous hydrogen-metal interactions

Besides chemical sputtering, the kinetic energy of low-energy ions and hot radicals is sufficient to overcome the surface energy barrier so these ions and radicals will be easily absorbed into the top layers. This may further enhance reaction rates by increased hydrogen density near the surface, and may also lead to supersaturation of hydrogen and blistering for materials like Si²¹ and Sn²². Other damage mechanisms from hydrogen absorption into metals and alloys are loss of ductility (embrittlement)²³ and increased diffusion and segregation²⁴. Interface stresses may be increased by interstitial hydrogen and hydride formation, which may be another mechanism to induce blistering²⁵, and may also result in roughening of the surface at ion energies well below the sputter threshold. In context of particle release, these mechanisms may generate particles and may significantly reduce the adhesion force of existing particles²⁶. For some metals, such as Pb, Sn and Zn, the (ion-assisted) reaction with hydrogen plasma may be a direct source of particles by decomposition of the metal, even in alloyed state. Clearly, these metals should be avoided or carefully shielded in a hydrogen plasma environment.

Figure 3 show a recent example of lead (Pb) particles exposed to an in-house Electron Cyclotron Resonance (ECR) hydrogen plasma source (T_e = 5 eV), showing disintegration and emission of Pb particulates. Besides decomposition of the particle also particle

fragments and particle movement were observed, and some particles were observed to have jumped onto a pristine monitoring surface facing the contaminated surface.

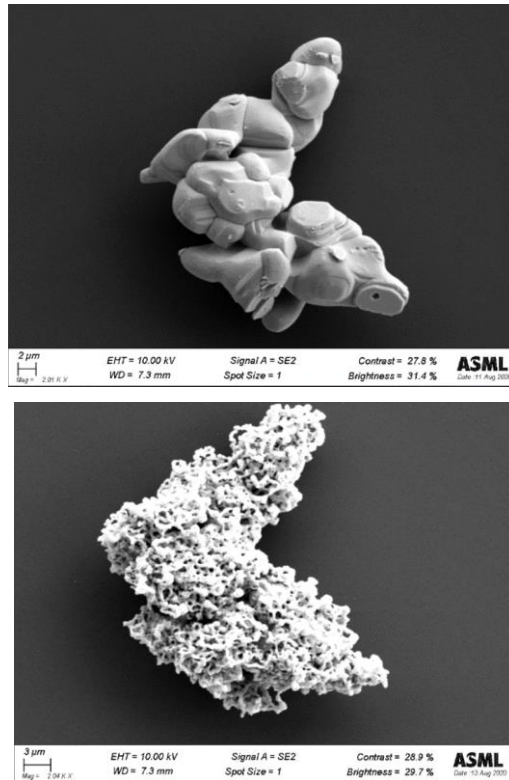


Figure 3: Decomposition of Pb by exposure to hydrogen plasma. Left: Pb particle as deposited. Right: eroded Pb particle after 17 hours of plasma exposure (Sairem Aurawave ECR, $\phi_{i,w}=10^{19} \text{ m}^{-2}\text{s}^{-1}$ and $T_e = 5 \text{ eV}$)²⁷.

Figure 4 shows example of tin (Sn) particles exposed to the same ECR hydrogen plasma source, resulting in roughening and particle release by open blisters and submicron holes, corresponding to expulsion of significant amounts of 100-500 nm particles in a large Sn particle. This blistering process is similar to earlier observation in fusion plasma wall materials²⁸, and is attributed to supersaturation of hydrogen atoms leading to internal stresses exceeding the yield limit along certain crystal planes; the differentiation between grains can be explained by different crystal orientations between the grains²⁹.

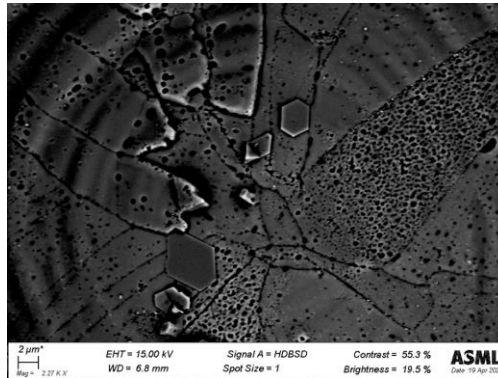


Figure 4: Blistering and pitting of large Sn particle by hydrogen plasma. Sn particle after 60 hours of plasma exposure (Sairem Aurawave ECR, $\phi_{i,w}=10^{19} \text{ m}^{-2}\text{s}^{-1}$, $T_e = 5 \text{ eV}$, sample at 283 K).

For thin metallic coatings, an additional concern is that the ion energies, even when corrected for the limited transfer efficiency of the light H_3^+ ions, are sufficient to induce self-diffusion and agglomeration, which may lead to roughening, de-wetting or delamination of the coating^{30,31}; an example is shown in Figure 5. In practice, this can be mitigated by depositing an amorphous coating, or by tailoring grain size and boundaries by e.g. alloying or doping the metal coating, or by optimizing the underlying interface³².

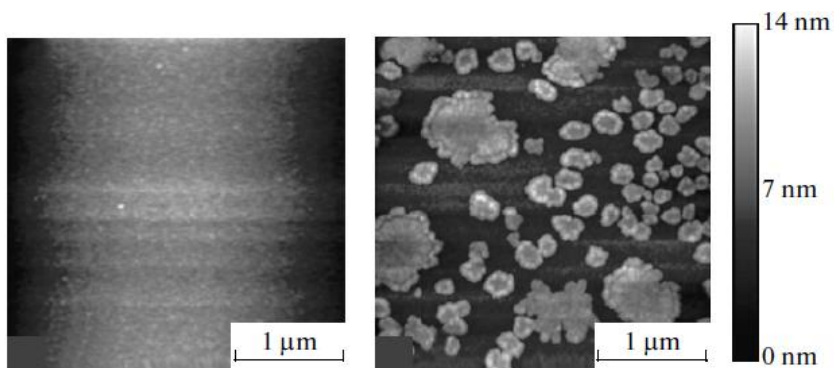


Figure 5: AFM measurements showing agglomeration of a thin (2 nm) molybdenum film on silicon, before (left) and after (right) exposure to $\sim 50\text{--}60 \text{ eV He}^+$ ions. From Malykhin³¹.

6.3.4. Hydrogen-Carbon interactions

Carbon and hydrocarbons are of specific interest because carbon is a ubiquitous contaminant in the scanner, from either adsorbates, fingerprints or residues of machining oils and greases³³. Under influence of EUV-irradiation, adsorbed hydrocarbons will decompose into a carbonaceous layer. The carbonaceous layer will typically be amorphous and hydrogenated (polymeric a-C:H), with a random combination of sp² (graphitic) and sp³ (diamond-like) states. Both states will etch when exposed to hydrogen radicals or a hydrogen plasma under formation of predominantly methyl (CH₃) and methane (CH₄), as described by Küppers^{34,35}.

In general, the carbon etch rate will depend on the carbon allotrope, with one to three orders of magnitude lower etch rates observed for graphitic carbon or polycrystalline diamond than for hydrogenated amorphous carbon³⁶. In an environment of hydrogen radicals, the activation energy for carbon etching has been found to be 0.3-0.4 eV at room temperature (depending on the bonding state of the carbon layer), while also an initial hydrogenation phase was observed with reduced etch rate³⁷.

At room temperature, the reaction rate will be low, especially for graphitic or diamond-like carbon. The reaction rate may be significantly enhanced in a plasma environment containing both hydrogen ions and radicals: the energetic ions create reactive sites by breaking bonds and the hydrogen radicals may react with the dangling bonds before these broken bonds have time to re-form. The etch yield will then be driven by the flux of energetic ions and the available density of hydrogen radicals at the surface. Highest etching rates are achieved for a system with both ions and a surplus of radicals; this condition is reasonably well satisfied in a confined EUV-induced plasma with typical radical-to-ion ratio of ~50, although for this ratio the radical reaction step will be rate-limiting³⁸.

This was first reported by Davis³⁹, showing ions to increase the etching yield of hydrogen atoms by more than an order of magnitude. This was captured in a semi-empirical model by Roth, Garcia and Rosales (RGR model), separating bulk from surface reactions and including the chemical aspect of the hydrogen ions⁴⁰. The radical contribution was emphasized more in by Hopf et al, describing chemical sputtering by

argon ions and hydrogen radicals³⁸; these models were combined and refined by Liu for hydrogen ions and radicals⁴¹. In this model the chemical sputtering yield is proportional both to the yield of bond-breaking by ion impact and to the probability of passivation of these broken bonds by absorbed radicals, scaled with the out-diffusion length of the reaction products. The nominal ion energy to break a C-C bond in the lattice may be taken as the sublimation energy of carbon of 7.4 eV. However, for hydrogenated (amorphous) surface layers the methyl dissociation energy has been found empirically to be lower at 4.5 eV³⁸. This endothermic energy needed may be further reduced by partial recovery of the dissociation energy by C=C double bond formation by the other half of the broken bond (with an energy gain of ~2eV). Thus, even at lower ion energies down to 1-2 eV, excitation of the C-C orbitals by incident ions can lead to reduction of activation energy and enhanced reaction rates with the hydrogen radicals to form C-H bonds⁴².

6.3.4.1. Chemical sputtering of carbon

As shown in Figure 1, the ion energies in the pulsed EUV-induced plasma are below 10 eV. Given the sputtering threshold $E_{thr} = 28$ eV for H_3^+ on carbon, physical sputtering may be ignored. At these low energies the penetration depth of the ions will be in range of ~1-2 nm, which is the relevant range for out-diffusion and etching at room temperature and above⁴¹. Ignoring physical sputtering, the etch rate of a hydrogen plasma ER_{plasma} is a combination of the etch yields by radicals $Y(H)$ and ions $Y(H_n^+, \varepsilon)$ respectively, plus a chemical sputtering term that describes the synergetic excitation by ions and termination by radicals:

$$ER_{plasma} = Y(H) \cdot \varphi_r + \int_0^{\varepsilon_{max}} (Y(H_n^+, \varepsilon) \cdot \varphi_i(\varepsilon) + Y(H_n^+|H, \varepsilon) \cdot \varphi_i(\varepsilon)) d\varepsilon \quad (6.4)$$

With φ_r the incoming radical flux, ε the ion energy and $\varphi_i(\varepsilon)$ the IEDF. Literature values for $Y(H)$ are in order of 10^{-5} #C/H, and in order of 10^{-2} #C/H for $Y(H_n^+)$ ^{36,43}. The

synergetic chemical sputtering yield term $Y(H_n^+|H)$ has been measured to be in a range of 0.1-0.7 #C/H for 10-100 eV ion energies, and may be extrapolated to stay above 10^{-2} #C/H down to at least 4 eV⁴⁴. This has been confirmed by internal measurements using an offline H₂ plasma (Sairem Aurawave ECR; no EUV) with significant sputtering yields over the full measured range down to 4 eV, as shown in Figure 6. For an otherwise similar He plasma this chemical sputtering term was not found, and a clear threshold energy was observed. Both observations are consistent with the mechanisms and simulations described above for ions both breaking bonds and reducing activation energies⁴⁰. The low penetration depth of hydrogen ions into carbon of a few atomic layers further enhances the surface erosion yield of low-energy hydrogen ions.

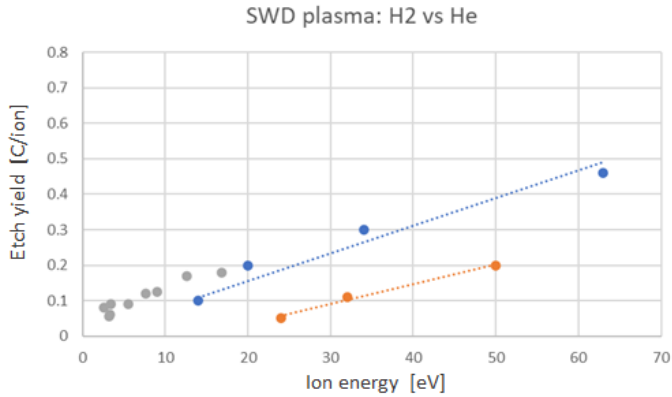


Figure 6: Carbon etch yield as function of average ion energy in off-line plasma (Surface Wave Discharge at 3 Pa – data courtesy of A. Dolgov⁴⁵); blue H₂ and yellow He; dotted lines are guide to the eye. Grey dots are additional data points from internal offline setup (Sairem Aurawave ECR, 20-100W in 5 Pa H₂)⁴⁶.

Equation 6.4 is often approximated by a ‘pure’ sputtering model by modifying $Y(H_n^+, \varepsilon)$ with artificially lowered values for the effective binding energy and threshold energy, but it should be realized that this approximation compromises on the physical meaning of the parameters and will be sensitive to both the radical-to-ion ratio and the ion energy distribution; so it may be significantly different for different plasma setups:

$$ER_{plasma} \cong Y(H) \cdot \varphi_r + \hat{Y}(H_n^+|H) \cdot \varphi_i \quad (6.5)$$

With $\hat{Y}(H_n^+|H)$ the effective chemical sputtering yield per ion for the average ion energy $\langle \varepsilon \rangle$. Following Hopf³⁸, for a sufficiently hydrogenated surface $\hat{Y}(H_n^+|H)$ may be approximated by:

$$\hat{Y}(H_n^+|H) \cong \frac{1}{1 + S \cdot \varphi_i/[H^*]} \cdot \hat{Y}_{max}(H_n^+) \quad (6.6)$$

With S an empirical factor describing the relative likelihood of C-H formation versus re-forming of C-C bonds under the ion load, and \hat{Y}_{max} the yield in case of full hydrogenation, for the average ion energy $\langle \varepsilon \rangle$. As shown in Figure 6, at room temperature, $\hat{Y}_{max}(H_n^+)$ may be approximated as scaling linearly from $\sim 10^{-2}$ at 1 eV ion energy to $\sim 10^{-1}$ at 10 eV ion energy⁴⁴, or $\hat{Y}_{max} \cong 10^{-2} \cdot \langle \varepsilon \rangle$. Chemical sputtering will thus dominate over thermal chemical reactions with $Y(H)$ estimated to be in order of 10^{-5} . At room temperature and for ion energies below 50 eV, the local etch rate may thus be approximated by:

$$ER_{plasma} \cong \frac{10^{-2} \cdot \langle \varepsilon \rangle}{1 + S \cdot \varphi_i/[H^*]} \cdot \varphi_{ion} \quad (6.7)$$

It should be noted that the pre-factor 10^{-2} will increase with substrate temperature, while the empirical constant will depend non-linearly on temperature. Thus, thermal conditioning of the substrate in vacuum thus needs to be considered explicitly in interpreting yields and translating results to other setups and conditions.

In steady state the radical density within the carbon scales linearly with the radical flux, but at the start of the etching process the radical density needs to build up first and the initial chemical sputtering yield in the first minutes will be low. Equation 6.7 shows that for very high ion fluxes (as may occur in fusion plasma conditions), the chemical sputtering rate will drop as the radical density in the top layers will saturate; this has indeed been confirmed by experiments in fusion context for $\varphi_{ion} > 10^{20} \text{ m}^{-2}\text{s}^{-1}$.⁴⁷ For scanner conditions the ion fluxes are some orders of magnitudes lower and the yield will be independent of the ion flux. Still, care should be taken in translating yield results

from accelerated off-line setups to scanner conditions.

6.3.4.2. Chemical sputtering enhancement by EUV

In an EUV-induced plasma, C-C and C=C bonds may also be broken by photons or secondary photoelectrons⁴⁸, besides by ions. The EUV absorption coefficient for carbon is low, so photons penetrate deeply and only ~1% will be absorbed⁴⁹ in the top ~2 nm that is considered relevant for etching at room temperature. The absorbed photons will generate free electrons which in turn will generate several secondary electrons, which may break bonds or provide activation energy for chemical reactions. The blur range of these secondary electrons is ~2 nm which is why the relevant depth is taken to be 2 nm rather than the 1 nm used for ions⁵⁰. The direct photon contribution to C-C bond breaking, with a cross section $\sigma_{hv,c-c} \sim 5 \cdot 10^{-22} \text{ m}^2$ at 13.5 nm wavelength⁵¹, may be neglected relative to the secondary photoelectrons, with a cross section $\sigma_{se,c-c} \sim 10^{-16} \text{ m}^2$ and SEY $\approx 1\%$ for carbon⁵².

It should be noted that the photon cross section increases for longer UV wavelengths⁵¹, so spectral purity and out-of-band light up till ~200 nm needs to be considered when comparing results from different setups.

As for the ions above, hydrogen radicals are required to form C-H bonds before the broken C-C bonds have time to re-form. Also, since the reaction products cannot easily escape from deeper within the material, the reverse reaction of hydrogen abstraction needs to be considered explicitly as well. This will reduce the EUV contribution on the (surface) etching rate and makes it difficult to quantify. Still, it should not be neglected upfront, since the photon flux to irradiated surfaces is several orders higher than the ion flux in 5 Pa H₂ gas. The EUV contribution to the etch rate may be assumed to be linear with the photon flux and may be combined with the ion contribution of Equation 6.7, with different empirical correction constants A_{hv} and A_{ion} :

$$ER_{EUV} \cong \frac{10^{-2} \cdot \langle \epsilon \rangle}{1 + S \cdot \varphi_i / [H^*]} \cdot \varphi_{ion} + \frac{S_{hv,1}}{1 + S_{hv,2} \cdot \varphi_{hv} / [H^*]} \cdot \varphi_{hv} \quad (6.8)$$

Where the empirical constants $S_{hv,1}$ and $S_{hv,2}$ depend on the carbon allotrope (graphitic, diamond-like or amorphous, with amorphous carbon having the lowest etch rate), and on the EUV spectrum. Trace amounts of hydrocarbons that might be present in the background gas supply (e.g. commercial H_2 is often generated from hydrocarbons) or in the EUV setup, will lead to a competing process of decomposition and deposition of carbon and carbonaceous molecules under influence of EUV⁴⁸. This will show up as an apparently lower values of the constant $S_{hv,1}$, which might even become negative; in other words, net carbon growth might be observed in the EUV spot⁵, depending on the cleanliness of the vessel and loadlock. Another concern is that off-line EUV sources are typically operated at higher pressures than the sample chamber and species from the EUV source chamber could enter the sample chamber. If there are no transport obstacles like spectral filters or folding mirrors, these species are likely to affect the sample at roughly the same location as the EUV spot, and the effect of these species might be difficult to differentiate from the EUV photons and ions. Thus, greatest care should be taken in translating empirical fit parameters from one EUV setup to another.

Outside of the irradiated areas, the photon contribution drops to zero, while the diffusing ions may etch for some cm's around the EUV spot. The additional impact of EUV has been measured earlier by Dolgov, and was found to be significant with respect to the ion contribution for H_2 , but not for He, as would indeed be expected in view of the proposed photon-enhanced chemical reactions⁴⁴. The presence of hot radicals in the EUV-plasma, of which some with similar energies to the ions, may also enhance the etch rate.

As outlined above, in steady state the radical density scales linearly with the radical flux, but at the start of the etching process the radical density needs to build up first and the initial etch rate will be low, and the competing mechanism of decomposition and deposition of hydrocarbons, which is instantaneous, may even lead to initial carbon growth. This is relevant both for scanning exposures and for short exposures, where equilibrium might not be reached and the effective etch rate will thus be reduced, or

initial net deposition may even occur. The radical density term is also the reason that the hydrogen plasma etch rate for 2D carbon materials, like graphene or CNT's, is typically significantly lower than for bulk carbon, since graphene/CNT's do not retain hydrogen radicals in the basal plane, and etching occurs primarily at defect sites⁵³; this is a crucial factor in the lifetime of CNT pellicles⁵⁴.

The above etch rate equations were combined with Particle-in-Cell plasma modeling to predict etching under different EUV/ions/radicals loads. The combined model was validated off-line in a low-power EUV-induced plasma, with independently added hydrogen radicals⁵⁵, confirming that besides ions also the highly energetic EUV photons must be included. With this additional EUV term included, a good match between model and measurement was observed, as shown in Figure 7, for varying levels of hydrogen radicals added⁴.

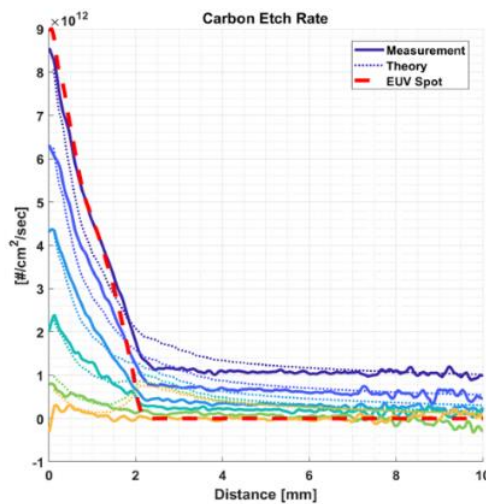


Figure 7: Off-line model validation for EUV-induced hydrogen plasma (EUV spot extends to 2 mm), with different levels of additional hydrogen radicals supplied (as indicated by the different colours).

A second test in a scanner-like LPP Source test set-up, without additional hydrogen radicals, essentially confirmed the model but also showed that the etching rate inside the EUV beam was ~4x lower than predicted, which may be explained by loss of radicals by convection effect of the finite hydrogen gas flow (which was not included in the

model); this is illustrated in Figure 8. An alternative hypothesis could be that there is concurrent decomposition of hydrocarbons and/or redeposition of methane⁵⁶ in the beam center. The second mechanism has been observed in fusion plasma conditions, but is considered unlikely in scanner conditions; this might warrant closer investigation as Source powers continue to increase.

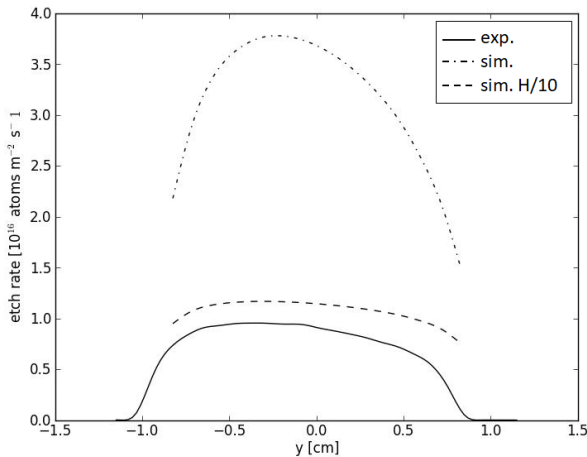


Figure 8: Measured etch rate (solid) vs model (dotted) in LPP Source test set-up, showing order of magnitude match (within factor ~4); also shown is improved match by manually correcting the modeled radical flux for convection (dashed).

In essence, the above shows that for low ion energies between 4 and 20 eV, as to be expected in EUV-induced plasma, the details of the ion energy distribution are relevant but not crucial, and that the radicals play a critical role in the etch rate. This is maybe not too surprising given the significant latent energy in a hydrogen radical of ~4.5 eV, which is of same order of magnitude as the kinetic energy in the molecular ion. While the above carbon etching mechanisms are highly beneficial for the continuous cleaning of carbon deposits on the EUV mirrors, the same mechanism results in loss of adhesion and gradual release over time for particles on top of carbon-containing contaminant layers such as oily residuals or fingerprints as the contaminant layers is eroded by the EUV photons and EUV-induced plasma. This is illustrated in Figure 9; such gradual release is consistent with the findings of Heijmans that particles released during

plasma exposure move according to force of gravity after release, and do not show acceleration into the plasma (as would be the case for electrostatic release)⁵⁷. A practical consequence of this is that surfaces in the scanner in the critical reticle zone must be completely free from human fingerprints and from hydrocarbon residues, since these will show reducing particle adhesion over time in the scanner plasma environment, and subsequent a steady particle release risk over time. Even invisible carbon residues from milling oils and greases may significantly influence measurements of interaction between EUV, plasma and materials⁵.

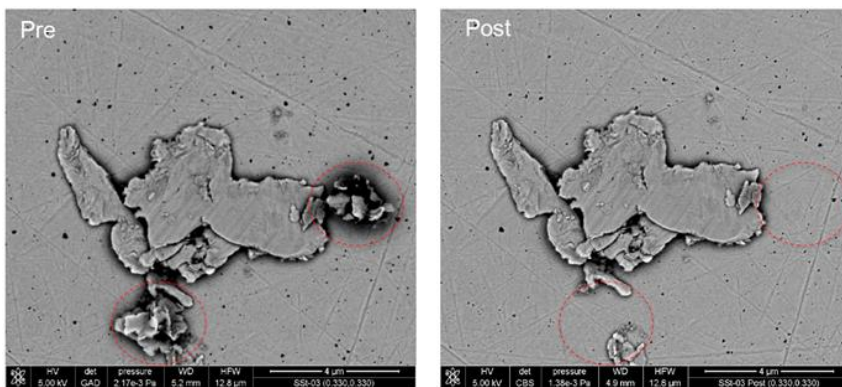


Figure 9: Plasma-cleaning of carbon contamination underneath small particles and resulting release of these particles (left picture prior to off-line hydrogen plasma exposure, and right same area after plasma exposure)⁴.

6.4. Conclusion

Plasma confinement and resulting contributions from secondary electron emission delays the formation of the plasma sheath of the hydrogen plasma generated by EUV. This in turn reduces the peak ion energies and brings the ion energies to below the sputtering threshold for mirrors and construction materials. Still, even for these ion energies, the hydrogen ions and radicals may affect many common construction materials and coatings in several ways, such as roughening, blistering and chemical reactions. This may have consequences for both particle contamination control as well as for molecular contamination control. The thermodynamics of hydrogen radicals and

ions is unfavorable for almost all materials, so whether an interaction becomes problematic relies on the details of the reaction kinetics. This makes it difficult to predict the impact of the scanner hydrogen plasma from other fields of application. In view of this, it is recommended that all construction metals, alloys and coatings should be rigorously evaluated for application in the scanner hydrogen plasma.

The plasma may affect particle adhesion by etching and roughening either the particle or the substrate, by chemical reaction, or by removing possible covalent bonds between particle and surface. Greasy or oily residues were found to be etched away by the hydrogen plasma, which will lead to release over time of particles on poorly cleaned materials. Also, materials that tend to react with hydrogen or form volatile hydrides were found to be liable to generate particles; these materials should be avoided or at least protected by a robust coating.

The confinement geometry and transients of the scanner hydrogen plasma make it difficult to translate findings from off-line laboratory EUV setups to scanner. Lower or higher pulse frequencies, as small focused spots, or different confinement geometries may change the interplay between photons, ions and radicals. Especially the sensitivity of surface chemistry and etching to the local radical flux has been underestimated so far. Better understanding of the scanner plasma will allow better interpretation and translation of findings on off-line setups.

6.5. *References*

¹ J. Israelachvili, “Intermolecular and surface forces”, 3rd edition, Academic Press (2011)

² M. Goetzinger et al, “Particle Adhesion Force Distributions on Rough Surfaces”, Langmuir Vol. 20 (2004)

³ M. van de Kerkhof et al, “Particulate and molecular contamination control in EUV-induced H₂-plasma in EUV lithographic scanner”, Proc. of SPIE Vol. 11489 (2020)

⁴ M. van de Kerkhof et al, “Understanding EUV-induced plasma and application to

-
- particle contamination control in EUV scanners”, Proc. of SPIE Vol. 11323 (2020)
- ⁵ M. van der Velden, “Radiation Generated Plasmas: A Challenge in Modern Lithography” PhD thesis (2008)
- ⁶ M. van der Velden et al, "Kinetic simulation of an extreme ultraviolet radiation driven plasma near a multilayer mirror" J. Appl. Phys. (2006)
- ⁷ Y. Yamamura et al, “Monte Carlo simulation of the thermalization of sputtered atoms and reflected atoms in the magnetron sputtering discharge”, J. Vac. Sci. Technol. A (1995)
- ⁸ M. Turchanin, “Cohesive energy, properties and formation energy of transition metal alloys”, Powder Metallurgy and Metal Ceramics (2008)
- ⁹ G. Lu et al, “Hydrogen embrittlement of aluminum: the crucial role of vacancies”, Physical review letters (2005)
- ¹⁰ Y. Yao, et al, “New molecular collisional interaction effect in low-energy sputtering”, Physical review letters (1998)
- ¹¹ K. Dobes et al, “Sputtering of tungsten by N⁺ and N₂⁺ ions: investigations of molecular effects”, Physica Scripta (2011)
- ¹² P. Phadke et al, “Near-threshold sputter yields of ruthenium under argon and nitrogen ion bombardment”, Nucl. Instrum. Methods Phys. Res., B 458 (2019)
- ¹³ C. Van de Walle, “Energetics and vibrational frequencies of interstitial H₂ molecules in semiconductors”, Physical review letters (1998)
- ¹⁴ L. Vergara et al, “Methane production from ATJ graphite by slow atomic and molecular D ions: evidence for projectile molecule-size-dependent yields at low energies”, J. Nucl. Mater. (2006)
- ¹⁵ C. Budtz-Jørgensen, et al, “Chemical and physical sputtering of aluminium and gold samples using Ar–H₂ DC-glow discharges”, Surface and Coatings Technology (2001)
- ¹⁶ A. Winkler, “Aluminum hydride desorption from hydrogen covered aluminum single crystal surfaces”, J. Chem. Phys. (1991)
- ¹⁷ V. Martirosyan et al, “Modification mechanisms of silicon thin films in low-temperature hydrogen plasmas”, Journal of Physics D: Applied Physics (2018)
- ¹⁸ D. Elg et al, “Removal of tin from extreme ultraviolet collector optics by in-situ hydrogen plasma etching”, Plasma Chemistry and Plasma Processing (2018)
- ¹⁹ M. Ji et al, “Effect of Hydrogen Ion Energy in the Process of Reactive Ion Etching of Sn Thin Films by Hydrogen Plasmas”, Plasma and Fusion Research (2021)

-
- ²⁰ S. Veprek et al, “Role of oxygen impurities in etching of silicon by atomic hydrogen”, *JVST A* (2008)
- ²¹ A. Kuznetsov et al, “Hydrogen-induced blistering of Mo/Si multilayers: uptake and distribution”, *Thin solid films* 545 (2013)
- ²² W. Ou et al, “Deuterium retention in Sn-filled samples exposed to fusion-relevant flux plasmas”, *Nuclear Fusion* (2020)
- ²³ M. Louthan et al, “Hydrogen embrittlement of metals”, *Materials Science and Engineering* (1972)
- ²⁴ K. Alvine et al, “Pb nanowire formation on Al/lead zirconate titanate surfaces in high-pressure hydrogen”, *Journal of Applied Physics* (2012)
- ²⁵ B. Terreault, “Hydrogen blistering of silicon: progress in fundamental understanding”, *Physica Status Solidi* (2007)
- ²⁶ D. Shefer, et al, “Morphology change and release of tin and lead micro-particles from substrates in hydrogen plasma”, *Proc. of SPIE Vol. 11609* (2021)
- ²⁷ O. Oomen, “Hydrogen plasma induced particle release”, M.Sc. thesis, Technical University Eindhoven (2020)
- ²⁸ S. Lindig et al, “Subsurface morphology changes due to deuterium bombardment of tungsten”, *Physica Scripta* (2009)
- ²⁹ W. Shu et al, “Microstructure dependence of deuterium retention and blistering in the near-surface region of tungsten exposed to high flux deuterium plasmas of 38 eV at 315 K”, *Physica Scripta* (2007)
- ³⁰ H. Galinski et al, “Agglomeration of Pt thin films on dielectric substrates”, *Physical Review B* (2010)
- ³¹ E. Malykhin et al, “Plasma cleaning of multilayer mirrors in EUV lithography from amorphous carbon contaminations”, *Moscow University Physics Bulletin* (2011)
- ³² P. Gadkari et al, “Comparison of the agglomeration behavior of thin metallic films on SiO₂”, *JVST A* (2005)
- ³³ H. Perko et al, “Surface Cleanliness Effect on Lunar Soil Shear Strength”, *Journal of Geotechnical and Geoenvironmental Engineering* (2001)
- ³⁴ J. Küppers, “The hydrogen surface chemistry of carbon as a plasma facing material”, *Surf. Sci. Rep.* 22 (1995)
- ³⁵ E. Vietzke et al, “Differences in the CH₃ and CH₄ formation from graphite under bombardment with hydrogen ions and hydrogen atoms/argon ions”, *Journal of Nuclear*

Materials (1984)

³⁶ E. Vietzke et al, “The reaction of atomic hydrogen with a-C:H and diamond films”, Surface & Coatings Technology (1991)

³⁷ J. Chen et al, “In situ ellipsometry study of atomic hydrogen etching of extreme ultraviolet induced carbon layers”, Applied Surface Science (2011)

³⁸ C. Hopf, “Chemical sputtering of hydrocarbon films”, J. Appl. Phys., 94 (2003)

³⁹ J. Davis et al, “Hydrocarbon formation due to combined H⁺ ion and H₀ atom impact on pyrolytic graphite”, Journal of Nuclear Materials (1988)

⁴⁰ J. Roth, “Chemical erosion of carbon based materials in fusion devices”, Journal of Nuclear Materials (1999)

⁴¹ S. Liu et al, “A general model for chemical erosion of carbon materials due to low-energy H⁺ impact”, Journal of Applied Physics (2010)

⁴² E. Salonen et al, “Swift chemical sputtering of amorphous hydrogenated carbon”, Physical Review B (2001)

⁴³ L. Vergara et al, “Methane production from ATJ graphite by slow atomic and molecular D ions: evidence for projectile molecule-size-dependent yields at low energies”, J. Nucl. Mater. (2006)

⁴⁴ A. Dolgov et al, “Comparison of H₂ and He carbon cleaning mechanisms in extreme ultraviolet induced and surface wave discharge plasmas”, Journal of Physics D: Applied Physics (2014)

⁴⁵ A. Dolgov, “Plasma-assisted cleaning of extreme UV optics”, PhD thesis, Twente University (2018)

⁴⁶ A. Dolgov, private communication (2019)

⁴⁷ W. Jacob et al, “Chemical sputtering”, chapter in ‘Sputtering by particle bombardment’, Springer Verlag, Berlin (2007)

⁴⁸ B. Yakshinskiy, “Carbon accumulation and mitigation processes, and secondary electron yields of ruthenium surfaces”, Proc. of SPIE Vol. 6517 (2007)

⁴⁹ Based on www.henke.lbl.gov

⁵⁰ A. Pret et al, “Modeling and simulation of low-energy electron scattering in organic and inorganic EUV photoresists” Proc. of SPIE Vol. 10146 (2017)

⁵¹ Y. Hatano, “Photoabsorption, photoionization, and neutral dissociation cross-sections of hydrocarbon molecules: physicochemical aspects of molecular processes in fusion edge plasmas”, Atomic and Plasma-Material Interaction Data for Fusion 77 (2008)

-
- ⁵² N. Faradzhev et al, “Stability of water monolayers on Ru (0001): Thermal and electronically induced dissociation”, Chem. Phys. Lett. 415 (2005)
- ⁵³ E. Despiau-Pujo, et al, “Hydrogen plasmas processing of graphene surfaces”, Plasma Chemistry and Plasma Processing (2016)
- ⁵⁴ M. Timmermans et al, “Carbon nanotube EUV pellicle tunability and lifetime”, Proc. of SPIE Vol. 11609 (2021)
- ⁵⁵ A. Lassise, ASML internal report (2018)
- ⁵⁶ D. Aussems, “Nanostructured microparticle synthesis by high-flux plasma processing”, PhD thesis, Technical University Eindhoven (2018)
- ⁵⁷ L. Heijmans, “Quantifying Plasma Particle Lofting”, PhD thesis. Technical University Eindhoven (2017)



Conclusions and recommendations

The primary research topics of this thesis are the plasma induced by pulsed EUV radiation in a confined geometry such as the EUV scanner, and the impact of that EUV-induced plasma on materials and contamination. The goal of this thesis was to extend the existing studies which typically focused on single-pulse EUV-induced plasma and/or open vessel geometries towards multi-pulse plasma and confined geometries, and also to bridge the gap between plasma itself and its interaction with the surroundings, both in terms of plasma-material interactions and in terms of the interaction between plasma and electrostatics.

In this chapter, the general conclusions are presented per topic. At the end, a summary of the main conclusions and the outlook will be given.

7.1. *Learnings and recommendations*

The main learnings and recommendations are summarized below:

EUV generation

Laser-produced plasma (LPP) is an efficient source of high-power EUV at 13.5 nm. Besides EUV this also generates VUV and UV spectral components that may impact imaging as well as scanner plasma characteristics. It is shown that VUV is absorbed by the mirrors and the gas in the scanner, and may be neglected at both reticle and wafer level.

UV is not absorbed strongly in scanner and might impact resist imaging at wafer level, though this has been shown to be minor. In terms of plasma especially the UV afterglow, which may last for 0.2-0.3 μs after the EUV pulse, may impact the scanner plasma.

Measured source emission spectra from high power EUV sources were presented, showing that UV/EUV ratio is roughly constant or may even improve for increasing source power. Thus, EUV imaging performance is robust against variations in CE and targeting. In principle, this also opens opportunities to optimize the LPP source independently for both power, imaging and desired plasma characteristics.

EUV-induced plasma

The existing descriptions of single-pulse and more or less open EUV-induced plasma's were extended with a treatment of confinement and multiple pulses.

It was found that confinement, with plasma-facing walls at a distance of order of the mean free path length of the energetic photoelectrons, requires explicit inclusion of secondary electron emission from the walls, which may be induced by photoelectric effect or by secondary electron emission by the energetic photoelectrons.

For a pulsed plasma with a period shorter than the decay time of the plasma, the plasma will consist of a quasi-steady-state cold background plasma, and periodic

transient peaks in ion energy and ion flux. This requires a bi-Maxwellian treatment. In terms of modeling, this means no easy assumptions can be made on the electron distribution functions, and a (Monte-Carlo) Particle-in-Cell (PIC) model is needed. We have presented an extension of the PIC model approach to complex 3D geometries and to multiple pulses, by using a Hybrid PIC-diffusion approach.

It was found that plasma confinement and resulting contributions from secondary electron emission delay the formation of the plasma sheath and thereby reduce the peak ion energies, and resulting ion energies will be ~ 2 eV, with a tail of up to roughly 10 eV. This is significantly lower than found earlier in single-pulse EUV-induced plasmas. These energies are well below the sputtering threshold for mirrors and construction materials. This holds both for close confinement around the beam as well as for close proximity to an EUV-mirror or the reticle. Materials with a high secondary electron emission may be beneficiary in this respect, but care should be taken that all materials must be robust against hydrogen radicals and ion-enhanced chemical reactions with hydrogen.

The UV afterglow of EUV generation will last longer than the EUV pulse itself, and might thereby frustrate sheath formation for some tenths of a microsecond; this also will result in reduced peak ion energies as the energetic electrons will cool down fast in the meantime.

Some discrepancies have been observed between the modeled energies and the measured energies. The overestimation in the model for the peak energies in the transient phase could be attributed to the possibly too conservative model estimates for the UV afterglow and/or to the secondary electron emission details. To clarify this, a time-resolved UV/VUV spectrometer will need to be developed, and accurate secondary electron emission measurements should be done for the relevant materials in the range of 10-100 eV. The underestimation in the model for the mid-term ion energies is attributed to the super-elastic collision effect not being captured sufficiently in the model. There is also some discussion on the absolute value of the RFEA energy measurements, as the RFEA itself is clearly affected by photoelectric effect from the

EUV pulse in the transient phase. Work has started to install an EQP on the LPP Source testrig to verify these aspects of the RFEA.

Looking towards the future, the EUV power will continue to rise to enable throughput improvements in the scanner. The ion flux will scale linearly with increasing EUV pulse energy, while the ion energy is independent of this, as all electron populations scale equally with power. However, in case EUV power should be increased further by increasing the LPP frequency, the ion energy will increase, as in that case the balance between the electron contributions from the gas and from the surface will shift towards the gas.

Discharges and reticle charging

It was found that the conventional wisdom of Paschen does not always hold in low-pressure systems ('left of the Paschen minimum') and certainly not in presence of a source of additional charge carriers. This has been modeled using Particle-in-Cell and validated off-line, and an analytical expression has been derived to guide future designs for higher source powers or different geometries.

The intrinsic negative charging of the floating reticle backside by EUV-induced plasma was studied in detail, and several countermeasures were explored. We developed the use of EUV itself as a conductive medium to de-charge the reticle backside during unload. This removes a risk of discharges to the reticle and greatly reduces electrostatic attraction of particles by the reticle outside of the scanner.

The frontside of the reticle was found to also briefly charge positively during the EUV pulse, by photoelectric electron emission. This positive voltage is quickly neutralized within microseconds by the plasma electrons. Still, the average voltage over the full pulse period is positive at $\sim 1-2$ V, translating to an electric field close to the reticle in order of 0.1-0.2 kV/m.

Charging of free-floating particles and particle transport

Particles within the EUV beam will briefly charge positive due to photoelectric electron emission, and subsequently will charge negatively by the fast plasma electrons. For larger particles above $\sim 1 \mu\text{m}$, after some microseconds electron and ion capture reaches equilibrium and the charge stabilizes at $\sim 1 \text{ e/nm}$, depending on the electron and ion temperatures. For submicron particles this equilibrium might take several pulses to reach.

In the plasma surrounding the EUV beam, even though particles will not experience the transient positive charging, the equilibrium between electron and ion capture will lead to similar charge values.

The negative charging of particles, in combination with the electrical field generated by the average reticle frontside potential, leads to an attractive force on the particle towards the reticle. This understanding allows to design the reticle crossflow such as to ensure the equations of motion for the particles do not result in endpoints on the reticle surface.

Particle charging at walls and release

Charging of particles by ionizing radiation, fast ions and electrons is known from observations from astrophysics and space missions, linking phenomena such as lunar glow and dust accumulation on spacecraft to such charging effects. We have translated these studies to the EUV-induced scanner plasma, and found that particle release by charging is mainly driven by fast electrons and the secondary electron emission these induce.

The transient plasma is an assisting factor in creating an electrical sheath field which may pull negatively charged particles into the plasma, but it was also found that the quasi-steady-state plasma tends to weaken the release force by neutralizing the charge patches which may have formed in the cavity between the particle and the surface. A

high-frequency pulsed plasma will thus result in an enhanced release probability by the repeating transients.

Plasma-material interactions

Plasma confinement and resulting contributions from secondary electron emission delays the formation of the plasma sheath of the hydrogen plasma generated by EUV. This in turn reduces the peak ion energies and brings the ion energies to below the sputtering threshold for mirrors and construction materials. Still, even for these ion energies, the hydrogen ions and radicals may affect many common construction materials and coatings in several ways, such as roughening, blistering and chemical reactions. This may have consequences for both particle contamination control as well as for molecular contamination control. The thermodynamics of hydrogen radicals and ions is unfavorable for almost all materials, so whether an interaction becomes problematic relies on the details of the reaction kinetics. This makes it difficult to predict the impact of the scanner hydrogen plasma from other fields of application. In view of this, it is recommended that all construction metals, alloys and coatings should be rigorously evaluated for application in the scanner hydrogen plasma.

The plasma may affect particle adhesion by etching and roughening either the particle or the substrate, by chemical reaction, or by removing possible covalent bonds between particle and surface. Carbon and carbonaceous layers, such as e.g. greasy or oily residues, were found to be etched away by the hydrogen plasma, which will lead to slow release over time of hydrocarbons and of particles from poorly cleaned materials in a plasma environment. Also, other materials that tend to react with hydrogen or form volatile hydrides were found to be liable to generate or release particles. These materials, such as tin, lead, zinc and silicon, should be avoided or at least protected by a robust coating. Besides this, the photoelectrons and the plasma may release particles by electric forces. Therefore, it is recommended that plasma-facing materials should be conductive to minimize stochastic release force excursions, and should preferably have a low secondary electron yield to prevent cavity charging underneath the particle.

In many descriptions of EUV-induced plasma's, radicals are ignored. However, close to the EUV-beam, radicals may have high kinetic energies of >1 eV and might be in an electronically excited state, both of which may further increase reaction rates and enhance hydrogen absorption into (semi)metals. Besides enhanced chemical reaction rates, the high-energy radical fraction in a confined EUV-induced plasma is also a concern for many metals as these radicals will penetrate beyond the surface barrier and may result in e.g. hydrogen embrittlement or blistering, and in case of coatings in loss of adhesion and delamination.

Off-line setups

The confinement geometry and transients of the scanner hydrogen plasma make it difficult to translate findings from off-line laboratory EUV setups to scanner. Lower or higher pulse frequencies, as small focused spots, or different confinement geometries may change the interplay between photons, ions and radicals. Especially the sensitivity of surface chemistry and etching to the local radical flux has been underestimated so far. Better understanding of the scanner plasma will allow better interpretation and translation of findings on off-line setups. Also, the photon spectrum of laboratory setups will often be significantly different from the scanner. This might originate from differences in the EUV source (e.g. Xe instead of Sn, or DPP instead of LPP), or from different spectral filtering in the ionizing 10-80 nm wavelength range (e.g. by using grazing-incidence mirrors instead of normal-incidence Bragg mirrors). Also, the UV wavelength range up till ~250 nm is relevant in view of the possibility of cold surface electrons being released by photoelectric effect in the afterglow after the EUV pulse. To better emulate the EUV plasma, it is recommended to explore the use of combined setups, e.g. a combination of ICP plasma with fast electrons from an e-beam and a hot-filament radical source.

7.2. *Summary and outlook*

In summary, the EUV-induced scanner plasma is instrumental in maintaining high system transmission by preventing carbon contamination and oxidation of the mirrors in the EUV scanner. Potential side effects however are etching of the surrounding construction materials, particle release, and risk of charging of floating surfaces and discharges. As the EUV is pulsed and thermal equilibrium is not in place for the energetic photoelectrons, a novel hybrid 3D-PIC model has been developed to describe the complex scanner geometry close to the reticle over multiple pulses. The improved understanding of the scanner plasma in the past years has enabled mitigation of these side effects and has helped to ensure that the EUV lithography scanners run reliably in high-volume manufacturing at high Source powers. These models and understanding also enable plasma-aware design guidelines and testing protocols for future EUV systems to be compatible with increasing source powers.

Looking towards the future, the EUV power will continue to rise to enable throughput improvements in the scanner. All things being equal, the ion flux will scale linearly with increasing EUV pulse energy, while the ion energy is independent of this, as all electron populations scale equally with power. However, in case EUV power should be increased further by increasing the LPP frequency, the balance between the electron contributions from the gas and from the surface will shift towards the gas, and as a result the ion energy will increase. To counter this, it is recommended to reduce the hydrogen pressure at higher source frequencies.

As the EUV-induced plasma characteristics and resulting plasma-materials interactions are a key aspect to the scanner performance in terms of imaging and yield, the sometime qualitative descriptions in this thesis should be followed up to create more quantification and more concrete design guidelines for materials and environment. These investigations should address all relevant aspects such as surface particle charging and release by plasma, particle (de)charging in the afterglow phase and attraction by reticle, hydrogen etching, and hydrogen absorption, embrittlement and blistering.

Acknowledgements

Even if I was the one doing the typing, this thesis owes its existence to two other people: Gerrit for planting the idea at a conference party in California and my old boss Vadim for enthusiastically sponsoring it. Also, the depth and range of the discussions with both of you during this journey have been truly awesome. You were always there when I needed you, and you let me find my own way when I didn't. Thank you!

I also want to thank the teams at ASML Research and D&E for all the discussions, and for generating the data that form the foundation of this thesis. You are too many to list without the risk of overlooking someone (so apologies if I missed any of you – let me know and I'll make it up to you with a beer). So, big thanks to Tjarko, Andrei, Andrey, Maarten, Ferdi, Christian, Alex, Michiel, Willem, Jeroen, Selwyn, Vladimir, Luuk, Manis, Jing, Efe, Edgar, Ruud, Ksenia, Ernst, Manish, Ronald, Volker, Daniel, Victor, Ankur, Chip, Tammo, Saeedeh, Evgenia, Gosse, Maria and all the others. And at the university, thanks to Job for always having new insight or angles to explore.

To Martien, Netty, Roy and Karin; thank you for making it so self-evident always that I should be a PhD (at least) – I have to admit I was not always so sure of that myself, and that it sometimes felt like a bit of a burden, but in the end it did provide the bedrock to finish this task. Also thanks to Erik, Rob, Frank, Stephanie, Arjan, Johan, Marcel, Gerrit, Louise, Harald, Marleen, Bas, Laurence, Paulien, Arnold, Inge, and all the other lovely people that managed to put up with me over the years and encouraged me on this road. Like it or not, there is something of all of you in who I am today 😊.

And last but not least, I offer both humblest apologies and deepest thanks to Josephine, Lara and Isabella for all the hours I spent on reading papers, (re)doing calculations and writing thesis chapters. You were absurdly gracious and sweet about it, but I am no fool (at least philologically, 'physics' is quite close to 'psychology'). I'm fully yours now, and I hope to have made you proud. I consider this a joint '*De Beroemde Familie*' production. Ipse dixit.

PS: Josephine, tu es toujours ma jardinière la plus charmante, qui fait fleurir mon âme.

Related publications

Parts of this thesis have been published in several papers and conference contributions, as listed below. Where applicable these are mentioned explicitly in the text or have been referenced:

- M. van de Kerkhof, J. Benschop, V. Banine, “Lithography for now and the future”, *Solid-State Electronics*, 155 (2019)
- M. van de Kerkhof, T. van Empel, M. Lercel, C. Smeets, F. van de Wetering, A. Nikipelov, A. Yakunin, V. Banine, “Advanced particle contamination control in EUV scanners”, *Proc. of SPIE Vol. 10957* (2019)
- M. Lercel, C. Smeets, M. van de Kerkhof, A. Chen, T. van Empel, V. Banine, “EUV reticle defectivity protection options” *Proc. of SPIE Vol. 11148* (2019)
- M. van de Kerkhof, A. Yakunin, V. Kvon, F. van de Wetering, S. Cats, L. Heijmans, A. Nikipelov, A. Lassise, V. Banine, “Understanding EUV-induced plasma and application to particle contamination control in EUV scanners”, *Proc. of SPIE Vol. 11323* (2020)
- M. van de Kerkhof, F. Liu, M. Meeuwissen, X. Zhang, M. Bayraktar, R. de Kruif, N. Davydova, “High-power EUV lithography: spectral purity and imaging performance”, *Journal of Micro/Nanolithography, MEMS, and MOEMS* (2020)
- P. Krainov, V. Ivanov, D. Astakhov, V. Medvedev, V. Kvon, A. Yakunin, M. van de Kerkhof, “Dielectric particle lofting from dielectric substrate exposed to low-energy electron beam”, *Plasma Sources Science and Technology* (2020)
- M. van de Kerkhof, E. Galutschek, A. Yakunin, S. Cats, C. Cloin, “Particulate and molecular contamination control in EUV-induced H₂-plasma in EUV lithographic scanner”, *Proc. of SPIE Vol. 11489* (2020)
- M. van de Kerkhof, A. Yakunin, V. Kvon, S. Cats, L. Heijmans, M. Chaudhuri, D. Astakhov, “Plasma-assisted discharges and charging in EUV-induced plasma”, *Journal of Micro/Nanopatterning, Materials, and Metrology* (2021)

- M. van de Kerkhof, A. Yakunin, D. Astakhov, M. van Kampen, R. van der Horst, V. Banine, “EUV-induced Hydrogen Plasma and Confinement in Scanner”, *Journal of Micro/Nanopatterning, Materials, and Metrology* (2021)

Following related papers are in preparation:

- M. van de Kerkhof, A. Yakunin, V. Kvon, A. Nikipelov, D. Astakhov, P. Krainov, V. Banine, “EUV-induced Hydrogen Plasma and Particle Release”, *Radiation Effects and Defects in Solids* (submitted)
- M. van de Kerkhof, E. Osorio, V. Krivtsun, M. Spiridonov, V. Medvedev, D. Astakhov, “Miniature Plasma Source for In-Situ Scanner Cleaning”, *Plasma Sources Science and Technology* (submitted)
- P. Krainov, V. Ivanov, D. Astakhov, V. Medvedev, V. Kvon, A. Yakunin, M. van de Kerkhof, “Particle lofting from substrate exposed to plasma and electron beam”, *Plasma Sources Science and Technology* (in preparation)

Curriculum Vitae

Marcus Adrianus van de Kerkhof

Feb 5 1968:

Born in Helmond, The Netherlands

1980 - 1986:

Atheneum, Carolus Borromeus College, Helmond (cum laude)

1986 - 1995:

Master of Science in Applied Physics

Eindhoven University of Technology, Eindhoven, Netherlands

Specialization: Fabry-Perot interferometry for in-situ plasma measurements.

1995 - 1999:

ODME, Eindhoven, Netherlands

Lead engineer for hardware and process development for DVD mastering equipment.

1999 - today:

ASML, Veldhoven, Netherlands

Senior systems designer and project manager, working on development of miscellaneous sensors as well as projection optics for both DUV and EUV scanners.

After serving as Product System Engineer for the development and introduction of the NXE:3400B/C EUV scanner, now in charge of EUV projects at ASML Research.

Publications: >40 papers and conference contributions

Patents: >100 US and WO patents

Winner of 'ASML Inventor of the Year' Award 2019